Far-Infrared Studies of High-T_c Superconductors

by

Qian Song

B.Sc. Lanzhou University 1982

M.Sc. Virginia Polytechnic Institute & State University 1987

A THESIS SUBMITTED IN PARTIAL FULFILLMENT
OF THE REQUIREMENTS FOR THE DEGREE OF
DOCTOR OF PHILOSOPHY
in the Department
of
Physics

SIMON FRASER UNIVERSITY
September 1995

APPROVAL

Name: Qian Song

Degree: Doctor of Philosophy

Title of thesis: Far-Infrared Studies of High-T_c Superconductors

Examining Committee: Prof. E. D. Crozier
Chairman

Professor B. P. Clayman, Senior Supervisor

Professor S. Gygax

Professor G. Kirczenow

Professor J. C. Irwin, Internal Examiner

Professor J. E. Eldridge, External Examiner
Department of Physics
University of British Columbia

Date Approved: August 24, 1995

PARTIAL COPYRIGHT LICENSE

I hereby grant to Simon Fraser University the right to lend my thesis, project or extended essay (the title of which is shown below) to users of the Simon Fraser University Library, and to make partial or single copies only for such users or in response to a request from the library of any other university, or other educational institution, on its own behalf or for one of its users. I further agree that permission for multiple copying of this work for scholarly purposes may be granted by me or the Dean of Graduate Studies. It is understood that copying or publication of this work for financial gain shall not be allowed without my written permission.

Title of Thesis/Project/Extended Essay

Far-Infrared Studies on High Tc Superconductors.

Author: _____
(signature)

Qian Song
(name)

29 August 1995
(date)

ABSTRACT

This thesis presents infrared studies on high-T_c superconducting single crystal and polycrystalline systems using a Bruker IFS 113V Fourier Transform Interferometer. For the single crystal system, the ab-plane optical conductivity of twinned single crystals of Ni-doped $YBa_2(Cu_{1-x}Ni_x)_3O_{6.95}$, for x=0, 0.75%, and 1.5%, has been studied using infrared reflectance spectroscopy over a wide frequency range, above and below T_c, The optical properties have been determined by a Kramers-Kronig analysis. In the superconducting state, our study indicates no conventional s-wave superconducting gap shown in the conductivity spectra, instead, it displays a low-frequency residual conductivity which was enhanced with Ni-doping. The dip in the conductivity close to 500 cm^{-1} is also getting weaker with Ni-doping. These results support either an extended s-wave or a d-wave model that has nodes in the gap function. In the normal state, Ni acts as a elastic scatterer, decreasing the (extrapolated) value of σ_{dc} and broadening the Drude-like conductivity. However, at the highest Ni concentration, T_c is still $89K$ and the London penetration depth keeps linear behaviour at low temperatures, indicating that Ni is not a pair-breaking scatterer in this material. By comparing our experimental studies of impurity effects, we find that the d-wave scenario is consistent with our results whereas there is clear qualitative disagreement between experiment and the theory for the s-wave case.

For our polycrystalline samples, we have focused on the lattice vibration and phonon assignment for the normal state properties and the temperature-dependent spectra of excitations for superconducting states. Most of the phonon features appearing in the spectra have been tentatively assigned by comparing the experimental work on similar compounds from other groups. Our results are in reasonable agreement

with theoretical calculations. We have also applied a direct calculation of the wave vector and frequency dependent lattice vibrational tensor of $Bi_2Sr_2CuO_{6+y}$ based on the shell model. We find that not only the mass of ions in a lattice but also its total ionic charge as well as the core-shell spring constant can cause a great deal of varying the phonon frequencies.

By taking the ratio, $R_s(T)/R_n(T)$, of the reflectance in the superconducting state to that in the normal state, we find no obvious evidence showing a superconducting energy gap from our experimental results in the Zn-doped $YBa_2(Cu_{1-x}Zn_x)_3O_{7-\delta}$ system. On the other hand, for both of our Ce-doped and Th-doped $Nd_{1.85}Ce(Th)_{0.15}CuO_{4-y}$ samples, the ratio , $R_s(T)/R_n(T)$, shows a low-frequency enhancement at $\sim 50cm^{-1}$ which is believed as the superconducting energy gap corresponding to $2\Delta_0/k_bT_c$ of 3.1 ± 0.2 (Ce) and 3.9 ± 0.2 (Th) respectively. These values are within the range found for conventional strong coupling superconductors.

ACKNOWLEDGEMENTS

I would like to acknowledge the help and support of my supervisor, Dr. Bruce P. Clayman, for his guidance and encouragement in writing this thesis. I have learnt and benefited a lot by working with him in many aspects.

I am very grateful to Dr. J. C. Irwin for many helpful discussions, advice, and for his willingness to answer my questions; and Dr. E. D. Crozier for the help and encouragement with my thesis.

I appreciate Drs. S. Gygax, J. C. Irwin, and G. Kirzenow for their kindness in correcting the draft version of my thesis; Dr. J. L. Peng at the University Maryland for supplying me with the Nd214 samples, Dr. R. X. Liang at the University of British Columbia for the high quality Ni-doped Y123 single crystal samples.

The last two years of my Ph. D. program was the most difficult time in my life. I feel so grateful to have the encouragement and support from our group members and many faculty members in the department. I owe a special debt to Dr. C. C. Homes for introducing to me the Ni-doped $YBa_2Cu_3O_{6.95}$ single crystal project and many discussions. This work would not been possible without his help and support. Thanks also go to Dr. G. Soerensen, for his friendship and many criticisms and suggestions; Andrew McConnell for his help in the lab; Sheron Beever, Julia MacAdam, Audrey Reid and Shauna Smith Simpson for their friendly help.

Finally, I acknowledge the Natural Sciences and Engineering Research Council of Canada and Simon Fraser University for financial support.

Dedicated to My Parents, Drs. Guizheng Wang, and Yongwu Song, my sisters Xi, Lu, and Tao, for their love and encouragement.

Contents

List of Tables

List of Figures

Chapter 1

Introduction

Ever since the copper oxide superconductors were first discovered in 1986, an enormous amount of work has gone toward investigating the cuprate superconducting materials. Since the crystal structures of these compounds are highly anisotropic, their electronic and superconducting properties may be expected to depend on these anisotropies as well. A number of recent experiments on the high-T_c superconductors give a strong indications that pairings state may not be a conventional s-wave symmetry which perfectly describes the pairing state of low-temperature superconductors. The unique characteristics of these new superconductors have stimulated development of new theories for possible superconducting mechanisms and extraordinary claims for the possibilities of superconductivity at high temperatures.

1.1 General Background on Superconductivity

The phenomenon of superconductivity has been studied since its first discovery by Kamerlingh Onnes [1, 2, 3, 4], in 1911. There are three most striking features of a conventional superconductor: 1) There is an absence of any measurable dc electrical resistivity below a certain temperature. This characteristic temperature is called the

superconducting transition temperature T_c. 2) A superconductor can be a perfect diamagnet provided that the magnetic field is not too strong. A surface electric current, induced by the applied field, can produce a magnetic field exactly canceling the applied field in the interior of the superconductor. This is called the Meissner effect. 3) There is usually an energy gap of width $2\Delta(T)$ centered at the Fermi level. The energy gap varies with temperature. An electron can be moved from the superconducting condensate only if its energy ϵ-ϵ_F exceeds $\Delta(T)$ which reaches its maximum value Δ_0 at T=0 and vanishes at $T = T_c$.

In order to make superconductivity of practical use, materials with high enough transition temperature are desired. Twenty six metallic elements and thousands of alloys and compounds have been found to be superconducting when they are cooled to sufficiently low temperatures [8]. However, in more than seven decades of research, progress in the search for high T_c superconductors has been very slow. The highest T_c ever achieved before 1986 was 23.2K for the alloy Nb_3Ge [8] and this was widely believed to be near the limit in a classical BCS coupling scheme [7].

The first breakthrough came in 1986 when Bednorz and Müller discovered T_c of 30K in the La-Ba-Cu-O system [9]. This result was soon confirmed by many other groups in the world. In the following year or two, many other related superconductors with much higher values of T_c were found. At present, there are four major groups of high T_c superconductors: (1) The original La-Cu-O [10, 11] system with various doping, with T_c in the $30 - 40K$ range; (2) $RBa_2Cu_3O_{7-\delta}$ (123) [12] with $T_c \sim 90\ K$, where R= rare earth elements; (3) the Bi-Sr-Ca-Cu-O [13] and Tl-Sr-Ca-Cu-O [14] systems with T_c up to 125 K; (4) the Nd-Ce-Cu-O system [15], the so-called n-type superconductor with $T_c \sim 20 - 30K$.

These various high T_c superconductors have many properties in common. Firstly, they all have a perovskite-like crystal structure, which consists of Cu-O sheets separated by more or less ionic layers. Secondly, all these compounds have copper and oxygen as common constituents. It is widely believed that the superconducting charge carriers are in the Cu-O sheets. Thirdly, all these compounds are quasi two-dimensional, in other words, the interplane coupling is very small. As a result, there is strong anisotropy in many of their properties. For example, resistivity measurements [16] show metallic behavior along the a- and b-axes, and insulating behavior along the c-axis. Infrared and tunneling measurements also show evidence of high conductivity in the plane and low along c-axis [17]. It is very likely that the two-dimensionality is a key factor in understanding many of the behaviors in these materials [17]

1.2 Theories of Superconductivity

There have been numerous theoretical efforts aimed at the explanation of superconductivity. In 1935, the London brothers [5, 6] proposed two equations which describe the perfect conductivity and the Meissner effect. In 1957, Bardeen, Cooper and Schrieffer [7] established the most important and successful theory of superconductivity, so-called BCS theory. The basic ingredients of this theory can be summarized as follows: (1) there is a net attractive interaction between electrons in the neighborhood of the Fermi surface, via an exchange of virtual phonons; (2) in the presence of such a net attractive interaction, two electrons at the Fermi surface (while the other N-2 electrons fill the Fermi sea) form a bound pair, called Cooper pair; (3) the normal metallic state is unstable with respect to the formation of a macroscopic condensed

state of all pairs with opposite spin and momentum (**k**, **-k**). An energy gap exists to separate the state with paired and unpaired electrons at the Fermi surface.

The BCS theory has several main quantitative predictions on superconductivity. In the weak coupling limit ($\rho V \ll 1$), the zero-temperature energy gap is given by

$$\Delta_0 = 2h\omega_D \cdot exp(-1/\rho V), \tag{1.1}$$

where ω_D is the Debye frequency, ρ is the density of states at the Fermi level and V is the phonon mediated electron-electron coupling constant which measures the strength of the electron-phonon interaction giving rise to the superconductivity.

The BCS superconducting transition temperature T_c has the form

$$T_c = 1.14\Theta_D \cdot exp(-1/\rho V). \tag{1.2}$$

Because of the presence of the exponential factor in Eq. 1.2, the critical temperature T_c is much smaller than the Debye temperature Θ_D. In fact, for $\rho V \ll 1$, T_c up to $25K$ should be very exceptional. This led many people to believe that $T_c = 23k$ in Nb_3Ge is the maximum one according to the weak-coupling BCS theory.

The ratio of Eqs. 1.1 and 1.2 yields a fundamental formula:

$$2\Delta_0/k_BT_c \ = \ 3.53\,, \tag{1.3}$$

which is independent of phenomenological parameters. This result holds for a large number of conventional superconductors to within about ten percent. Since, in the BCS theory, the interaction between electrons and phonons is assumed to be small compared to the maximum phonon energy, and the interactions between quasiparticles are neglected, the theory is also called the "weak coupling" theory of superconductivity. Deviations from this theory can usually be explained by strong-coupling effects [21], which allow arbitrary electron-phonon coupling strengths.

This simplest BCS model predicts a rise to 100% reflectance and zero absorptance at T=0 for photons below the energy $2\Delta_0$. In the superconducting state, electrons respond in a unique way to optical radiation that they can move through the solid with absolutely no scattering. Unless a photon has enough energy, $\hbar\omega \geq 2\Delta(T)$, to break apart a pair of electrons, absorption does not occur. Above the superconducting gap, $2\Delta_0 = 3.5k_BT_c$, absorption should start and reflectance should decrease. Thus, for such low energy excitation, the superconducting energy gap $2\Delta(T)$ should be measurable by standard infrared techniques.

There are several cases in which the gap might be hard to detect experimentally or might occur at an energy other than that predicted by $2\Delta_0 = 3.5k_BT_c$. One case where a superconducting transition would be hard to detect optically is that the superconductor might be in the clean-limit which is defined as $\Gamma \ll 2\Delta_0$, where Γ is the scattering rate represented in cm^{-1}. The clean-limit is characterized by a low scattering rate Γ for the conduction electrons, making the normal state conductivity peak much narrower than the superconducting gap $2\Delta_0$. Therefore, the normal state electrons absorb a negligible amount at the energy $2\Delta_0$ and the drop to identically zero absorptance has very little impact on the optical properties. $\sigma_1(\omega)$ exhibits such a small change at $2\Delta_0$ that is completely overwhelmed by other absorption processes such as phonons and charge transfer bands [59] [90]. It is also possible that the gap function has node lines at the Fermi surface, so that the energy gap varies size along different directions in reciprocal space. The lack of a unique gap energy makes soectroscopic observation impossible.

Although the BCS theory has been found to be in good agreement with many experimental results for conventional superconductors, it met several apparent difficulties in the new high-T_c superconductors. First of all, the high value of T_c cannot

be explained by Eq. 1.2. Secondly, many experiments show direct symmetry-based evidence of strong pairing anisotropy in the cuprates. For instance, a photoemission spectroscopic result indicates a significant gap anisotropy with the gap vanishing to within resolution at several points on the Fermi surface [112]. The conventional s-wave BCS theory can not explain the unusual behavior of the anisotropic pairing state.

These results have encouraged many researchers to look for other mechanisms of superconductivity. Instead of the conventional BCS electron-phonon theory, many new and modified microscopic models have been proposed. For example, the RVB (Resonance-Valence-Bond) model, the theory proposed for the high temperature superconductivity first by Anderson [22], 1987; and a recent one, the interlayer tunneling mechanism, by Anderson and Chakravarty et al. [23], 1993; magnetic disturbances model, which is different from Anderson's interlayer tunneling mechanism, by R. Dynes et al. [24]; and a rapidly growing body of theoretical and experimental work, the spin-fluctuation mechanism with its predicted $d_{x^2-y^2}$ pairing state by a number of groups [52]; and many more, e.g., Schrieffer et al [27]., 1988; Varma et al. [26], 1990, W. M. Que and G. Kirczenow [28]. But there still is no consensus regarding the microscopic mechanism for the high T_c superconductivity.

On the other hand, some experimental results [10, 11] have shown that the elementary current-carrying excitation in the superconducting state has the charge 2e, which suggests that Cooper pair-like bound states are formed, just as in the conventional superconductors. Recent precise penetration depth measurements by Bonn *et al.* [100] provide evidence that shows a linear behavior of penetration depth $\Delta\lambda(T) = \lambda(T) - \lambda(1.3T)$ at low temperature in the $YBa_2Cu_3O_{6.95}$ system. This linear behavior is quite unlike the exponentially activated behavior caused by the

nodeless energy gap of a conventional s-wave BCS superconductor. This result is consistent with an anisotropic energy gap that has nodes at the Fermi surface, as discussed by Hirshfeld and Annett *et al.* [110] [111]. Now the question is whether electron-phonon interactions provide the binding mechanism as with the conventional superconductors or the spin-fluctuation mechanism is the basis of the high-T_c superconductivity. Is BCS theory highly relevant to the mechanism of the high temperature superconducting materials or not?

In order to answer this question, more experimental data on the optical properties and electronic band structure of these materials are needed. Among the many experimental techniques that can be used to probe electronic structures, infrared spectroscopy, which had been used successfully with the classic superconductors, plays an important role in investigating the energy gap and any spectral feature responsible for the superconducting pairing and in determining the electronic and vibrational properties of these high-T_c superconductors.

1.3 Outline of This Thesis

The purpose of this study is to use infrared spectroscopy techniques to examine the optical properties of both normal and superconducting states in high T_c superconductors. Both single crystal and polycrystalline materials are studied. For our Ni-doped single crystals $YBa_2Cu_3O_{6.95}$, the difficulties in observing features associated with a gap in clean-limit systems motivate us to study the effect of impurities on the optical conductivity. Additionally, impurity doping in in the CuO_2 planes of hole-doped cuprate superconductors may also allow a distinction between unconventional (extended s-wave or d-wave) and anisotropic conventional (s-wave) models. For the

superconducting polycrystalline samples, we examine the effects of impurities on the low frequency optical response. We also attempt to find any superconducting absorption by taking the ratio of the reflectance in the superconducting and normal states of the polycrystalline samples. For the normal state, we try to address electronic and vibrational properties of high temperature materials. Such information, which could provide fundamental knowledge about the nature of a substance, would be very helpful for understanding the mechanism of the high-T_c superconducting oxides.

The thesis is organized as following: Chapter 2 will give a brief review of the optical properties of metals and superconductors as well as the background of infrared spectroscopy. The phenomena relevant to our experiments will be discussed in more detail. The experimental far-infrared spectroscopy apparatus and arrangement will also be illustrated in this chapter. Then the experimental work is divided into two parts, one contains Chapter 3, 4, and 5 which represent the studies on three high-T_c superconducting polycrystalline systems of Zn-doped $YBa_2Cu_{3(1-x)}Zn_{3x}O_{7-\delta}$, Pb-doped $Bi_{2.125-x}Pb_xSr_{1.875}CuO_{4-\delta}$, and $Nd_{1.85}M_{0.15}CuO_{4-\delta}$ (M=Ce, Th); Chapter 6 is about the infrared study on Ni-doped single crystals $YBa_2Cu_{3(1-x)}Ni_{3x}O_{6.95}$ with x=0, 0.75% and 1.5%, respectively. Finally, Chapter 7 summarizes the overall thesis and some possible future directions.

Chapter 2

Optical Spectroscopy: Theory and Experimental Methods

2.1 Optical Properties of Superconductors

2.1.1 Dielectric Response Function

In this section, we summarize some important relations for the optical constants of a medium subjected to an electromagnetic field of frequency ω. For an optically isotropic material, i.e. uncharged, homogeneous, linear, and local in its response, the microscopic optical properties may be characterized quite generally by a frequency-dependent complex dielectric function $\tilde{\epsilon}(\omega)$ defined as

$$\tilde{\epsilon}(\omega) = \epsilon_1(\omega) + i\epsilon_2(\omega)\,, \tag{2.1}$$

where $\epsilon_1(\omega)$ is called the real dielectric function and $\epsilon_2(\omega)$ the imaginary. In addition to $\epsilon_1(\omega)$ and $\epsilon_2(\omega)$, other quantities are often used to describe the optical properties of a material. These include the complex conductivity, $\sigma(\omega) = \sigma_1(\omega) + i\sigma_2(\omega)$, the complex refractive index, $N(\omega) = n_1(\omega) + in_2(\omega)$, and the skin depth, δ *et al.*. These

quantities are not independent. They are interrelated by

$$\epsilon_1(\omega) = n_1(\omega)^2 - n_2(\omega)^2\,, \tag{2.2}$$

and

$$\epsilon_2(\omega) = 2n_1(\omega)n_2(\omega)\,. \tag{2.3}$$

$$\tilde{\sigma(\omega)} = i\omega\epsilon_0(1 - \tilde{\epsilon}(\omega))\,, \tag{2.4}$$

where $\epsilon_0 = 8.854 \times 10^{-12} C^2/Nm^2$ is the permittivity of free space. The real part of the optical conductivity is one of the most commonly used optical properties because at the low frequency it can be compared to results of dc resistance measurements. Inserting the numerical value for ϵ_0 and converting the frequency to wavenumbers from Eq. 2.2, we can write the real and imaginary parts of the frequency dependent conductivity as

$$\sigma_1(\omega) = \frac{n(\omega)k(\omega)\omega}{30} = \frac{\omega\epsilon_2(\omega)}{60}\,. \tag{2.5}$$

and

$$\sigma_2(\omega) = \frac{\omega(1 - \epsilon_1(\omega))}{60}\,. \tag{2.6}$$

respectively, where a value of ω measured in cm^{-1} gives the conductivity in units of $(\Omega cm)^{-1}$. At zero frequency $\epsilon_1(0)$ becomes the static dielectric constant and $\sigma_1(0)$ is the ordinary dc electrical conductivity, σ_0.

The simplest model for the dielectric function of a metal is the free electron theory, Drude model [29]. The basic assumption in this theory is that within the metal the valence electrons of the atoms are free and these electrons can be treated by the kinetic

theory of gas. When the electrons in the metal are subjected to an external electric field, the behavior of the electrons is determined by a balance between two forces: (1) the -eE force exerted by the electric field and (2) the relaxation of electrons towards equilibrium by elastic scattering processes, treated as a damping force $m\Gamma\frac{d\vec{r}}{dt}$. Here Γ is the relaxation rate, $\Gamma = V_F/l$ with V_F as the Fermi velocity and l the electron mean free path. The Drude complex dielectric function $\tilde{\epsilon}(\omega)$ can be written as:

$$\tilde{\epsilon}(\omega) = \epsilon_\infty - \frac{\omega_p^2}{\omega^2 + i\omega\Gamma}, \tag{2.7}$$

where ω_p is the plasma frequency, defined as

$$\omega_p{}^2 = \frac{4\pi n e^2}{m}. \tag{2.8}$$

and n, e and m being the number of the electrons per unit volume, the charge and mass of the electron, respectively.

The Drude frequency-dependent conductivity $\sigma(\omega)$ [30] is then obtained by:

$$\sigma(\omega) = \frac{\sigma_0}{1 - i\omega/\Gamma} \tag{2.9}$$

where σ_0 is the dc conductivity defined by

$$\sigma_0 = \frac{ne^2}{\Gamma m} \tag{2.10}$$

The frequency-dependent conductivity $\sigma(\omega)$ falls steadily from this value with a characteristic width of Γ, a frequency usually in the microwave or far infrared region of the spectrum. Most metals have relaxation times in the 10^{-14} sec range. This corresponds to a conductivity of $\sigma_0 \sim 2 \times 10^5 \Omega^{-1} cm^{-1}$ or a resistivity of $5\mu\Omega - cm$.

Then the reflectance of a infinitely thick medium, $R = I_R/I_0$, has the form

$$R = \frac{(1 - n_1)^2 + {n_2}^2}{(1 + n_1)^2 + {n_2}^2} \tag{2.11}$$

at normal incidence. At low frequencies, $\omega \ll \Gamma$, metals have $n_2 \approx n_1 \gg 1$, and a Hagen-Rubens reflectance [31] holds:

$$R \approx 1 - \sqrt{\frac{8\omega}{\omega_p{}^2/\Gamma}}. \tag{2.12}$$

2.1.2 Kramers-Kronig Relations

The Kramers-Kronig dispersion relations enable us to find the real part of the response of a linear passive system if we know the imaginary part of the response at all frequencies, and vice versa. For the real and imaginary parts of the complex dielectric function, the Kramers-Kronig relations (known as KK relations) are

$$\epsilon_1(\omega) = 1 + \frac{2}{\pi} P \int_0^\infty \frac{\omega' \epsilon_2(\omega')}{\omega'^2 - \omega^2} d\omega' , \tag{2.13}$$

$$\epsilon_2(\omega) = -\frac{2\omega}{\pi} P \int_0^\infty \frac{\epsilon_1(\omega')}{\omega'^2 - \omega^2} d\omega' \tag{2.14}$$

where P stands for the Cauchy principal value of the integral where the singularity in the integral at $\omega = \omega'$ is omitted from the integration:

$$P \int_0^\infty \equiv \lim_{a \to 0} \left[\int_0^{\omega - a} + \int_{\omega - a}^\infty \right] . \tag{2.15}$$

There are several similar KK relations between $\sigma_1(\omega)$, $n_1(\omega)$ and $n_2(\omega)$. For the experimental determination of optical properties, the most important feature of the KK relations is the one which relates the phase shift upon reflection (θ) to the reflectance (R). In terms of the amplitude reflection coefficient r, the reflectance of a thick sample at normal incident is given by

$$R = r r^*, \tag{2.16}$$

where

$$\tilde{r} = |\tilde{r}|\, e^{i\theta} = \frac{n_1 - 1 + in_2}{n_1 + 1 + in_2}\,. \tag{2.17}$$

Here $|\ \tilde{r}\ | = R^{1/2}$ is the amplitude of $\tilde{r}$ and θ is the phase shift of the light wave caused by the reflection. According to the KK relations regarding R and θ, we have

$$\theta(\omega) = \frac{\omega}{\pi} \int_0^\infty \frac{\ln R(\omega') - \ln R(\omega)}{\omega^2 - \omega'^2} d\omega'\,. \tag{2.18}$$

The reflectance $R(\omega')$ is determined directly from experimental measurements but the phase angle of Eq. 2.17 has to be found by numerical integration. If $R(\omega')$ is measured, $\theta(\omega)$ can be evaluated from this relation, resulting in equations for the two quantities n_1 and n_2, from which any of the other constants may be calculated.

Whenever $R(\omega')$ is independent of ω', there is no contribution to the integral. Similarly, when $\omega' \gg \omega$ or $\omega' \ll \omega$, the contribution is very small. The range of the Kramers-Kronig integral extends over all frequencies, requiring extrapolations beyond the measured frequency interval. Typically, power laws are used at high frequency, $R \sim \omega^{-\alpha}$ with $0 \leq \alpha \leq 4$. At low frequencies the reflectance will be assumed to follow the Hagen-Rubens relation, $R = 1 - A\sqrt{\omega}$, if the sample is a metal.

A fundamentally important sum rule is the oscillator-strength sum rule which relates the rate of energy absorption by transverse electromagnetic field:

$$\begin{aligned} \int_0^\infty \sigma_1(\omega') d\omega' &= \frac{1}{2}\frac{\pi n e^2}{m} \\ &= \frac{1}{2}\epsilon_0 \pi {\omega_p}^2\,. \end{aligned} \tag{2.19}$$

In terms of ω and ϵ_2, the sum rule can be given as

$$\int_0^\infty \omega \epsilon_2(\omega') d\omega' = \frac{1}{2}\pi {\omega_p}^2. \tag{2.20}$$

The sum rule provides an important consequence that the area under the curve of $\sigma_1(\omega)$ vs ω is a constant, independent of factors such as temperature, phase transition, etc.

2.1.3 Optical Response of Superconductors

One of the most important features of the conventional superconducting state is that electrons can move through the solid with absolutely no scattering at T=0 K. These electrons respond in a unique way to optical radiation. While the normal electrons can absorb light and transfer the energy to the lattice through collisions, the superconducting electrons have no mechanism through which to absorb energy. Thus unless a photon has enough energy to break apart a pair of electrons, absorption does not occur. Therefore, condensation of the electrons into the superconducting state leads to a perfect reflectance in the energy range below the electron binding energy, $2\Delta = 3.5k_BT_c$.

Within the BCS theory, Mattis and Bardeen (MB) have calculated the real and imaginary parts of the frequency-dependent conductivity, σ_{1s} and σ_{2s}, respectively, [32] for superconducting materials. At all non zero frequencies below the superconducting gap the real part of the conductivity is zero at zero temperature and exponentially activated at finite temperature, according to the BCS theory. Fig. 2.1 illustrates the MB theory for ratio of the conductivity in superconducting state to the normal state value, $\sigma_{1s}(\omega)/\sigma_n$ and $\sigma_{2s}(\omega)/\sigma_n$, as a function of frequency $\omega/2\Delta_0$. It is clear that the superconducting gap $2\Delta_0$ corresponds to the point above which the $\sigma_{1s}(\omega)$ starts to rise to join the normal state conductivity $\sigma_n(\omega)$ at a substantially higher frequency. The infinite dc conductivity is represented in the frequency-dependent conductivity of a superconductor by a delta function at zero frequency.

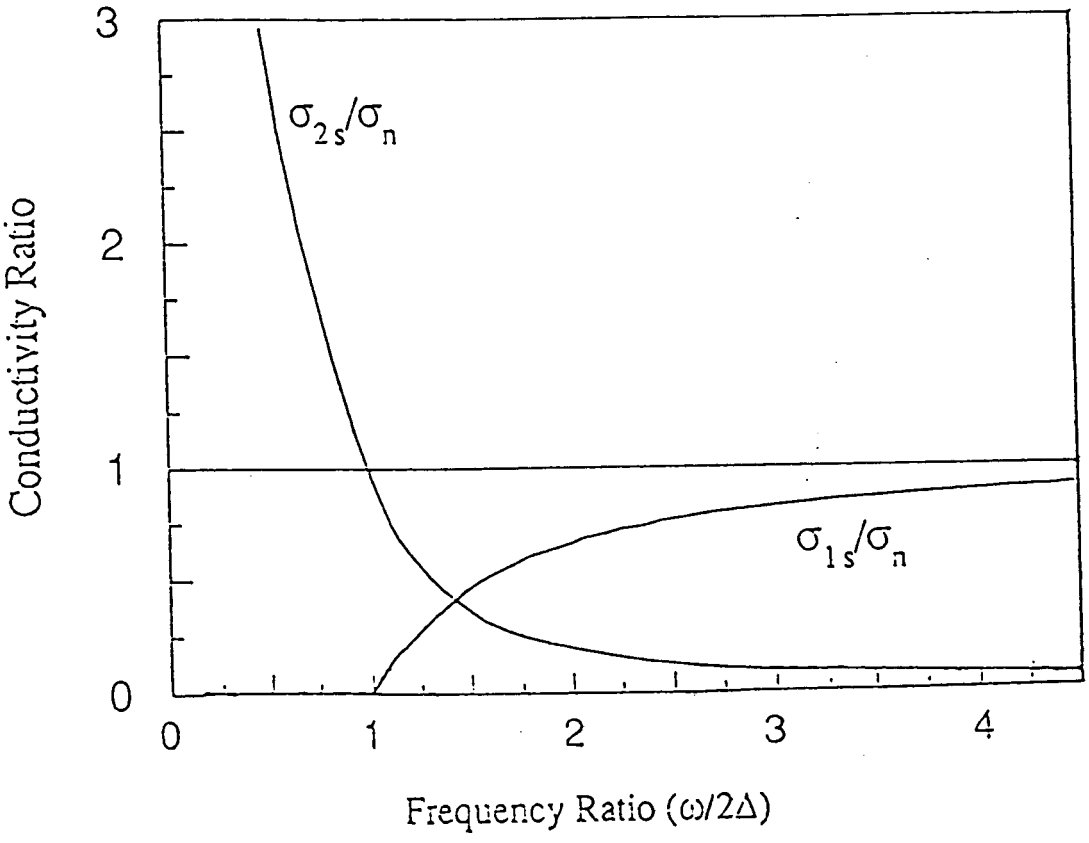

Figure 2.1: The calculated real and imaginary parts of the frequency-dependent conductivity of a BCS-type superconductor.

The simplest BCS model predicts a rise to 100% reflectance and zero absorptance at T=0 for photons below the energy $2\Delta_0$. There are several cases where this change might be hard to detect experimentally or might occur at an energy other than that predicted by $2\Delta_0 = 3.5k_BT_c$. One case where the effects of a superconducting transition would be hard to detect optically is that in which the superconductor is in the clean limit. A straightforward BCS model can be used to predict the optical properties of superconductors in either a clean or dirty-limit, which is defined as

$$\text{Clean limit} \; : \quad \Gamma \ll 2\Delta_0 \, ; \tag{2.21}$$

$$\text{Dirty limit} \; : \quad \Gamma \gg 2\Delta_0. \tag{2.22}$$

where the scattering rate Γ is represented in cm^{-1}. In terms of the electronic mean free path l, and the Pippard coherence length $\xi_0 = v_F/\pi\Delta_0$, the above definitions correspond to $l \gg \xi_0$ for the clean-limit and $l \ll \xi_0$ for the dirty-limit.

The dirty-limit is characterized by a high scattering rate Γ for the conduction electrons, making the normal state Drude conductivity peak wider than the superconducting gap $2\Delta_0$. In the clean-limit, the scattering rate is low and the Drude conductivity peak is much narrower than $2\Delta_0$. In both cases, the basic BCS prediction of perfect reflectance and zero absorption at T=0 remains unchanged. For a clean-limit superconductor however, normal state electrons absorb a negligible amount at the energy $2\Delta_0$ and the drop to identically zero absorptance has very little impact on the optical properties. Many of the low-T_c superconductors are believed to be in this limit, exhibiting such a small change in $\sigma_1(\omega)$ at $2\Delta_0$ that is completely overwhelmed by other absorption processes such as phonons and charge transfer bands [59] [90].

There are several circumstances in which the size of the gap could become zero while the sample retains superconducting characteristics. For temperature close to

but below T_c, materials in which there are magnetic impurities can simultaneously display superconducting characteristics and show no gap at the Fermi surface [97]. It is also possible to have superconductors in which the size of the energy gap is anisotropic along different directions in reciprocal space. In this case, it is possible to have nodes at which the gap function is zero at some points on the Fermi surface. We will discuss such cases more detail in Chapter 6.

2.2 Spectroscopic Techniques

In optical experiments one generally measures the intensities of the incident (I_0), reflected (I_R) or transmitted (I_T) beams. From conservation of energy it follows

$$I_0 = I_R + I_T + I_A, \tag{2.23}$$

where I_A is the intensity absorbed by the sample. Dividing by I_0 in Eq. 3.1, we obtain the familiar relation

$$\tilde{R} + \tilde{T} + \tilde{A} = 1, \tag{2.24}$$

where $\tilde{R} = I_R/I_0$, and $\tilde{T} = I_T/I_0$ and $\tilde{A} = I_A/I_0$ are the "apparent" reflectance, transmission and absorption, respectively. From measurements of $\tilde{R}$ it is possible to determine directly the optical constants.

This study focussed on measurements of far infrared reflectance of high temperature superconductors.

2.2.1 Spectroscopic Apparatus

The most popular technique used in the study of the infrared properties of the high T_c superconductors is the measurement of specular reflectance over a wide range

of frequencies followed by the Kramers-Kronig analysis that yields the phase and hence the optical constants. For the present work, a Fourier-transform spectroscopy photometer, the IFS 113V Bruker was used. The IFS 113V Bruker covers the whole infrared region with a high pressure mercury lamp as source for the far-infrared range, a globar for the mid-infrared, and a tungsten-halogen lamp the near-infrared. Fig. 2.2 shows the optical layout of the IFS 113V Bruker.

The principal interferometer used in spectroscopy owes the theory of operation to the basic Michelson interferometer. As shown in Fig. 2.2, the basic component, which works as an interferometer in the IFS 113V Bruker, consists of a beamsplitter and three mirrors. The two mirrors, $m3$ and $m4$, are fixed; and the other, the scanning mirror, is able to be moved at a constant velocity. The radiation, which is initially assumed to be monochromatic, of the source (1) or (2) is reflected by fixed parabolic mirrors $m1$ and $m2$, as shown in Fig. 2.2. The incident beam of radiation then strikes the beamsplitter(BMS) and is divided into reflected and transmitted components. These continue to their respective mirrors where they are reflected back to the beamsplitter. The two waves finally moving towards the detector have travelled different paths and hence interfere optically with each other. From interference theory, we know that the components are transmitted preferentially on to the detector only if their path difference is $0, 1, 2, 3$, *etc.*, whole wavelengths, i.e., constructive interference occures. When the position of the moving mirror is such that the path difference is half a wavelength then the components are completely out of phase and destructive interference occurs, the radiation being reflected back to the source. Scanning the moving mirror at a constant velocity causes the beam to go in and out of phase; the modulated frequency of the resulting sinusodal wave is then directly propotional to the velocity of the moving mirror.

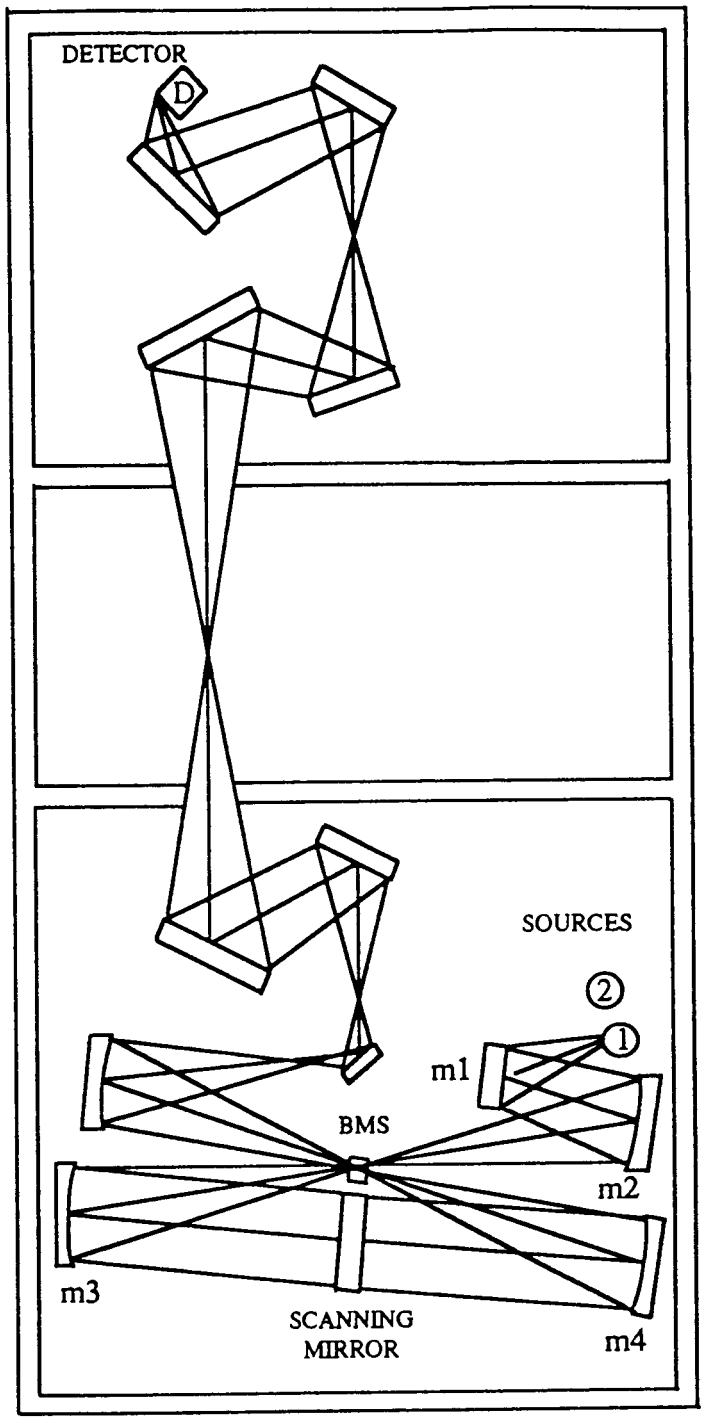

Figure 2.2: The top view of the optical layout of IFS 113V Bruker

The modulated signal received at the detector is known as the interferogram. It can be shown that the interferogram is the cosine Fourier transform of the intensity of the source at a particular frequency (see Section 2.2.2 for reference), as modified by the characteristics of the instrument.

Turning to the case of a broadband source, i.e., one emitting more than one frequency, the interferogram obtained here is the resultant of the interferograms for each frequency in the source. As the moving mirror scans, the detector sees the intensity variations of all the frequencies simultaneously. All the spectral information is recorded in a multiplexed form at the detector during each scan of the moving mirror. The spectrum is obtained, therefore, by taking the Fourier transform of the interferogram. It is necessary to measure two interferograms, one for the sample and one for the background, in order to obtain the reflectance spectrum of the sample from the ratio of the two.

2.2.2 The Principle of Fourier Interferometers

Referring to Fig. 2.2 we denote $l - x/2$ as the optical path between the source (1) and the detector (D) of the beam which is reflected at the scanning mirror toward the fixed mirror $m3$, and E_1 the electric field of this beam at P, where x is defined as the optical path difference . Similarly, $l + x/2$ and E_2 are the optical path and the electric field of the beam reflected at the scanning mirror which is moving away from mirror $m4$. For a monochromatic source of frequency $\omega = 2\pi c\tilde{\nu}$ we have

$$E_1(\tilde{\nu}) = A_1(\tilde{\nu})A_S(\tilde{\nu})e^{2\pi i c\tilde{\nu}t}e^{ik(l-x/2)}, \tag{2.25}$$

$$E_2(\tilde{\nu}) = A_1(\tilde{\nu})A_S(\tilde{\nu})e^{2\pi i c\tilde{\nu}t}e^{ik(l+x/2)}. \tag{2.26}$$

$A_1(\tilde{\nu})$ depends on instrumental conditions of the interferometer (source efficiency, losses by transmission of beam splitter, lenses, filters, windows and by reflection at mirrors, etc.), and $A_S(\tilde{\nu})$ depends on the optical properties of the sample. For a reflectance experiment $A_S(\tilde{\nu}) = \tilde{r}_s(\tilde{\nu})$ is the complex amplitude of the beam reflected at the sample, and for transmission experiment $A_S(\tilde{\nu}) = \tilde{t}_s(\tilde{\nu})$ the complex amplitude of the beam transmitted by the sample. Using $k = 2\pi/\lambda = 2\pi\tilde{\nu}$ and the expressions (eqs. 2.25, 2.26) the intensity at the point P is

$$I(x,\tilde{\nu}) = \frac{1}{2}|E_1 + E_2|^2 = S(\tilde{\nu})(1 + \cos 2\pi\tilde{\nu}x), \tag{2.27}$$

where $S(\tilde{\nu}) = |A_1(\tilde{\nu})|^2|A_S(\tilde{\nu})|^2$ is the spectral intensity at wavenumber $\tilde{\nu}$. For a polychromatic source emitting light between $\tilde{\nu} = 0$ and $\tilde{\nu} = \infty$ we obtain the interferogram

$$\begin{aligned} I(x) &= \int_0^\infty S(\tilde{\nu})(1 + \cos 2\pi\tilde{\nu}x)d\tilde{\nu} \\ &= \frac{1}{2}I(0) + \int_0^\infty S(\tilde{\nu})\cos 2\pi\tilde{\nu}x)d\tilde{\nu}, \end{aligned} \tag{2.28}$$

where $I(0)$ is the intensity at zero path difference. Applying the classical form of Fourier's integral, we obtain the desired spectrum

$$S(\tilde{\nu}) = 4\int_0^\infty [I(x) - \frac{1}{2}I(0)]\cos 2\pi\tilde{\nu}x)dx\,. \tag{2.29}$$

In practice, $S(\tilde{\nu})$ is approximately given by the sum:

$$S(\tilde{\nu}) \simeq 4\sum_{x=0}^{D}[I(x) - \frac{1}{2}I(0)]\cos 2\pi\tilde{\nu}x)\Delta x\,, \tag{2.30}$$

where D is the maximum optical path difference and $x = h\Delta x$ with h =0, 1, 2, ... $D/\Delta x$. Let G and $D(\tilde{\nu})$ be the gain of the amplifier and the detector sensitivity. Then the actual computed reflectance transmission spectrum of the sample is

$$P_S(\tilde{\nu}) = G_S D(\tilde{\nu})|A_I(\tilde{\nu})|^2 R_S(\tilde{\nu})\,, \tag{2.31}$$

where $R_S(\tilde{\nu}) = |A_I(\tilde{\nu})|^2 = |\tilde{r}_s(\tilde{\nu})|^2$ is the reflectance of the sample and $|A_B(\tilde{\nu})|^2 = R_B(\tilde{\nu}) = 1$ for in ideal mirror at the place of the sample, and we obtain

$$R_S(\tilde{\nu}) = G_B P_S(\tilde{\nu})/G_S P_B(\tilde{\nu}). \tag{2.32}$$

2.2.3 Cryogenic Arrangement

The polycrystalline samples were mounted on a cold finger in a continuous-flow cryostat, as shown in Fig. 2.3, allowing the reflectance to be measured between 7 and 300 K. The cold finger, which was built by Dr. J. M. Wrobel, is composed of a heating coil, a copper bar, a temperature sensor, and a U-shaped stainless steel tube which is attached to the back of the copper bar for cooling the whole cold finger. A copper shield with a slot of 1.3 cm wide is used to cover the cold finger and screen the background radiation from outside. The cryostat is pumped to a good vacuum $\sim 10^{-6}$ mbar at room temperature before transferring liquid N_2 or liquid H_2 and then kept that vacuum in order to avoid contamination of the spectra by water vapor. The dewar is isolated from the interferometer vacuum by a window of either mylar or polypropylene film, which is transparent in the frequency range of our interest. Once the cryogenic system is under the thermal quasi-stable condition at low temperature with continuous-flowing LHe, the temperature of samples can be controlled within 0.2 K by carefully adjusting the Helium return valve. With the tail of the cryostat inside the Bruker's sample chamber, the system sits on the top of the Bruker. Changing the height of the benches, as many as five samples can be measured by moving their position vertically to the focus of the beam in sample chamber. Since the beam must pass through an optical window to reach the sample, the window is angled to reflect light away from the mirror in order to avoid window reflections. Another sample set up with a R. G. Hansen High-Tran continuous-flow cryostat was employed for the

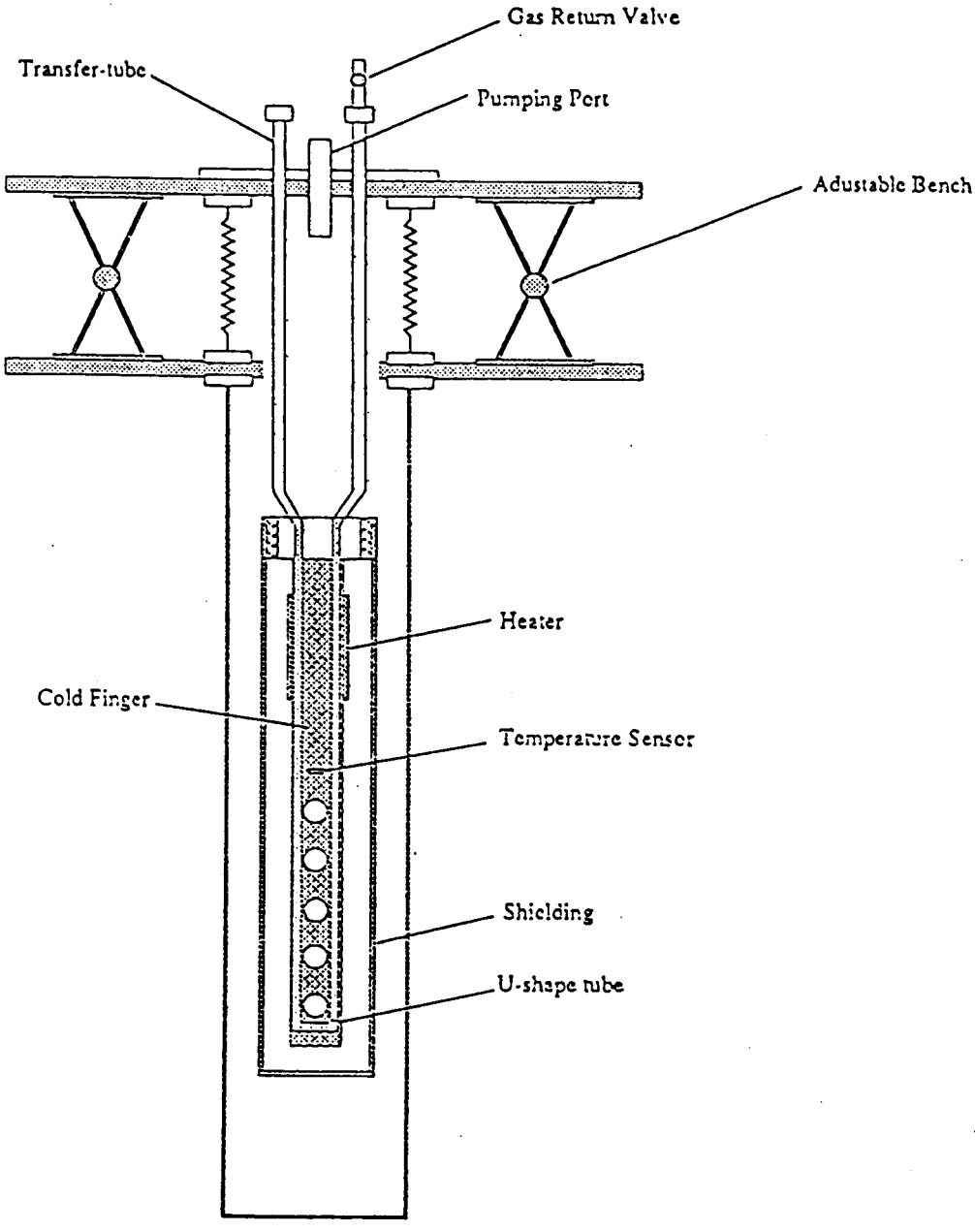

Figure 2.3: Cross section view of the cryostat with cold finger

reflectance measurement on Ni-doped single crystals $YBa_2Cu_3O_{7-\delta}$. Chapter 6 gives the detail.

In far infrared measurements, either a room temperature detector or a germanium bolometer is used. The reflectance measurement becomes particularly difficult in the far infrared due to the weakness of Hg-arc lamps and lack of photoconductive detector. To compensate for the problems, a He-cooled germanium bolometer is employed as a detector for low frequency and weak signal measurements. The germanium bolometer is cooled down to its working temperature of 2.5 K - 4.5 K by a commercial bolometer cryostat (model HD-3; Infrared Laboratories). A cooled-preamplifier, which is a low-noise voltage amplifier, is employed for the first-stage electronics; the electric signal is in turn transferred to the data input of Bruker. Helium consumption for twelve hours of measurement is about 4 liters.

Chapter 3

Far-Infrared Properties of the Superconducting Alloys $YBa_2(Cu_{1-x}Zn_x)_3O_{7-\delta}$

3.1 Introduction

Since the discovery of high-T_c superconductors, a tremendous efforts have been devoted to exploring the infrared properties of $YBa_2Cu_3O_{7-\delta}$, and other oxide superconductors, as reviewed extensively in Refs [17] [46]. The optical properties, and their dependence on the composition, structure, temperature, etc. of this oxide are important for understanding the nature of superconductivity. In particular, partial substitutions of transition metals from iron to Zn have received great attention in attempting to understand the origin of superconductivity. In this chapter we study far-infrared reflectance on ceramic $YBa_2(Cu_{1-x}Zn_x)_3O_{7-\delta}$, where $x = 0\%$, 3% and 4%, in both the normal and superconducting states. Among all $3d$ substitutions in $YBa_2Cu_3O_{7-\delta}$, Zn has an unique role for probing the $3d$ holes of Cu on superconducting properties, because Zn has a fixed valence state of 2^+ and preferentially occupies $Cu(2)$ sites in the CuO_2 planes which have the uppermost significance in the

high-T_c superconductors [33] [54]. However, there is still some disagreement on the substitutional site of Zn. Despite many studies indicate that Zn substitutes on the Cu(2) site, some work favors Cu(1) as the site of Zn substitution [56]. This could be due to the presence of other phases in the samples. For conventional superconductors, the presence of magnetic impurities, which act as pair breakers in BCS theory, can destroy the superconductivity. The most surprising result from the substitutions for copper in $YBa_2Cu_3O_{7-\delta}$ by transition and non-transition elements [33], however, is that the non-magnetic ion Zn^{+2}, with a closed-shell ($3d^{10}$), has a strong deleterious effect on T_c. This reinforces the conclusion that the material has anomalous behavior, different from that of conventional superconductors.

Our purpose in this work is to investigate the optical properties and the role of local structure by analyzing the changes in the far-infrared spectrum of Zn-doped Y-Ba-Cu-O. We shall also examine the vibrational structures and their assignments to eigenvectors of the primitive cell of $YBa_2Cu_3O_{7-\delta}$. Because the far-infrared radiation penetrates on the order of 1 μm below the sample surface, the results are not very sensitive to the oxygen depletion which is known to occur at the surface and the results are thus representative of the bulk material.

The anisotropy of the high-T_c materials makes optical measurements on polycrystalline samples less useful in the search for a superconducting energy gap, since it is very hard to control the orientation of the crystal grains on the surface of the sample, and therefore the measured reflectance is the average from the three directions along a, b, and c-axis. At the time when we started the measurements on the Zn-doped $YBa_2Cu_3O_{7-\delta}$, ceramic materials were the only samples available to us. Since the positions of the vibrational modes wouldn't be affected by the absolute reflectance, we will concentrate our study on the phonon assignment and some of the normal

state properties in this chapter and discuss the detail of the optical properties and superconducting gap problem of $YBa_2Cu_3O_{6.95}$ in Chapter 6.

3.2 Preparation and Characterization of Zn-doped $YBa_2(Cu_{1-x}Zn_x)_3O_{7-\delta}$

Samples were synthesized in appropriate atomic ratios of $Y : Ba : Cu_{1-x}Zn_x = 1 : 2 : 3$ with $x = 0\%$, 3% and 4% from the powders of pure (99.99%) Y_2O_3, BaO, CuO and ZnO. To improve the homogeneity, the well- mixed powders were held at 920°C for 10 hours. The reaction products were ground and die-pressed into pellets of $1.5\,mm \times 12\,mm$ diameter. Pellets were then sintered at 930°C for 20 hours, cooled to 700°C, kept at that temperature about 5 hours then cooled to room temperature under ambient condition; cooling required about 10 hours. All the heating processes were in a pure oxygen atmosphere. For every different Zn concentration x, more than four samples were prepared for optical infrared and DC resistivity measurements. The experiments were repeated on the samples and results were reproducible.

X-ray diffraction patterns Fig. 3.1 show that all three samples have orthorhombic structures, predominately single phase; the content of impurity phases was small for the three samples. Peaks due to impurities are marked with asteriks. By comparing the x-ray data of $BaCuO_2$, which is one of the three common impurities found in the $YBa_2Cu_3O_{7-\delta}$ X-ray spectra, we can assign the impurity peaks in Fig. 3.1 are from the $BaCuO_2$ phase material [43].

DC resistivity measurements, under Dr. Gygax's supervision in his laboratory, were performed by using a standard four-probe method from room temperature to liquid helium with a current of 10 mA; no dependence of the measured resistivity

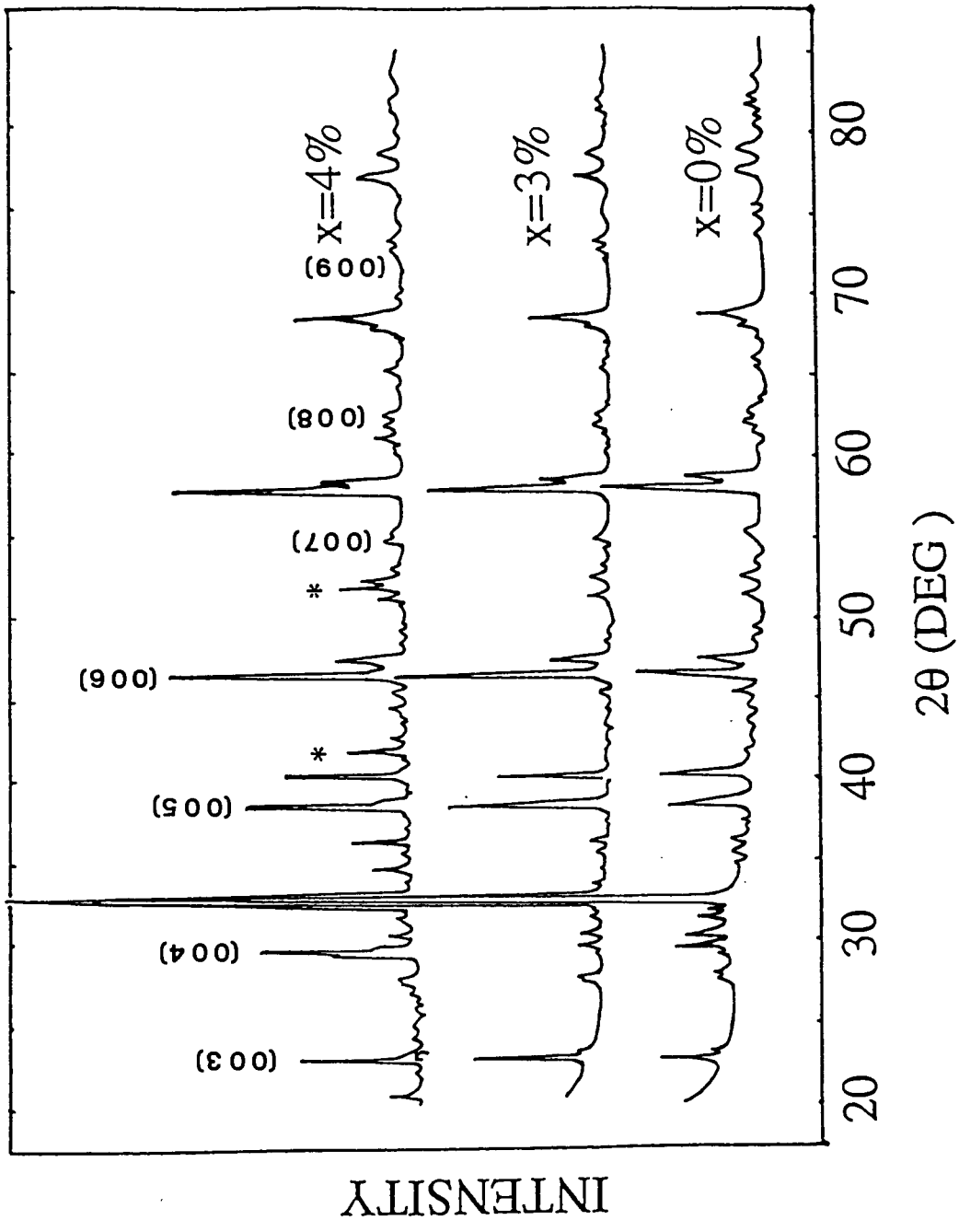

Figure 3.1: X-ray diffraction of $YBa_2(Cu_{1-x}Zn_x)_3O_{7-\delta}$, peaks due to impurities are marked with asteriks(ref. [45]).

on measuring current was noted up to 50 mA. Samples were cut and shaped as rectangular bars ($4mm \times 1mm \times 1mm$) for resistivity measurements. Fig. 3.2 shows the temperature dependence of resistivity for the three $YBa_2(Cu_{1-x}Zn_x)_3O_{7-\delta}$ with $T_C = 89K$, 61 K, and 49 K for $x = 0\%$, 3% and 4%, respectively [45]. The values T_c were obtained at the onset of zero resistivity from the transition curve in Fig. 3.2. The width of transitions ($\Delta T \leq 6K$) indicates that the samples are highly homogeneous. The critical temperatures of our samples fall within the range reported in [33]. It is interesting to note that, in Fig. 3.2, the normal state resistivity just above the superconducting transition decreases with increased x. However, some other groups [33] and [44] show that resistivity increases with increased x. Sample preparation techniques clearly affect the normal state resistivity. Affronte et al. [36] attribute this sensitivity to a two-band situation with a delicate competition between holes and electrons.

3.3 $YBa_2Cu_3O_7$ Crystal Structure and Symmetry

Fig. 3.3 shows the unit cell of $YBa_2Cu_3O_7$. The unit cell has $N = 13$ atoms. The corresponding crystal structure, with the a and b axes differing by less than 2% generally and c axis paralleling to the long cell dimension and, is identified as an orthorhombic unit cell. The size of the unit cell is given by the lattice constants [47] which, for this structure, are $a = 3.822$ Å, $b = 3.891$ Å and $c = 11.677$ Å, respectively.

The nearly ideal $1 \times 1 \times 3$ dimensions ($3.8 \times 3.9 \times 11.7$), coupled with the "1-2-3" cation stoichiometry, are composed of a stack of three perovskite-like cubes ABO_3. This stack contains an ordered metal arrangement with copper filling all the octahedral "B" cube corner sites, and a regular sequence $...Ba-Y-Ba/Ba-Y-Ba...$

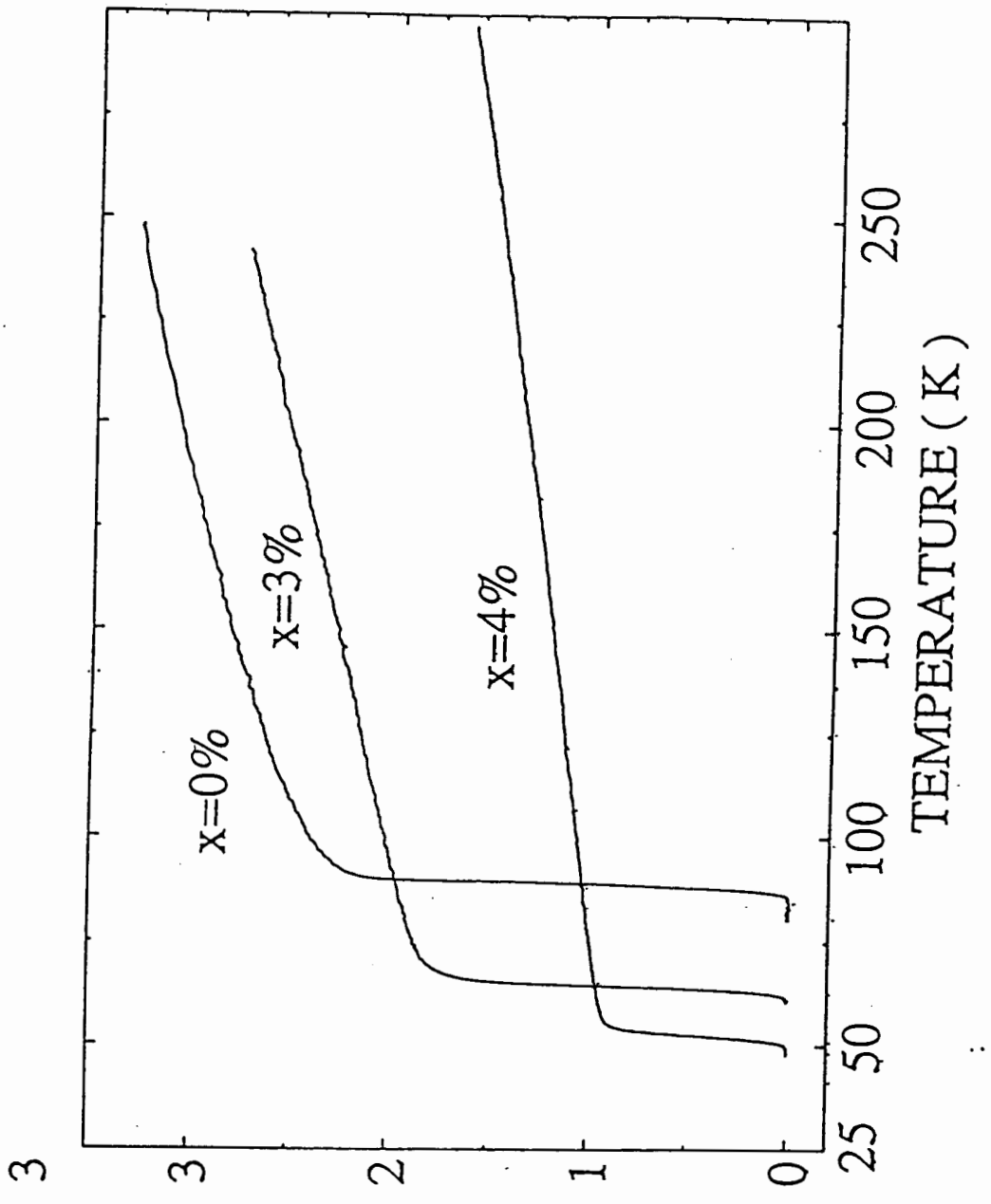

Figure 3.2: Resistivity vs temperature of $YBa_2(Cu_{1-x}Zn_x)_3O_{7-\delta}$ (ref. [45]).

in the large "A" sites. All oxygen atoms are assumed at the perovskite-like anion positions, half way between copper atoms along cube edges. $O(1)$ oxygens are at the level of $Cu(1)$ halfway along the b-axis, so b is slightly longer that a. In ideal $YBa_2Cu_3O_7$ materials, $O(1)$ sites are fully occupied. The $Cu(1)$ and $O(1)$ atoms form the CuO chains which are believed to act as charge reservoirs [50]. The $Cu(2)$, $O(2)$, and $O(3)$ atoms make up the superconducting CuO_2 planes, which are important features of Y123 compounds. Between the CuO chains and CuO_2 planes are the $O(4)$ atoms commonly referred to as apical or bridging oxygen atoms.

For the oxygen deficient system $YBa_2Cu_3O_{7-\delta}$, structures remain orthorhombic for $0 < \delta < 0.5$. The $O(1)$ content in orthorhombic $Y123$ varies significantly depending on conditions of synthesis. Under high oxygen pressure the structure may actually accommodate more than seven oxygens. Changing $O(1)$ occupancy has a relatively minor effect on structural parameters. Substitutions of Zn do not affect the orthorhombic distortion of $Y123$ [53].

The space group for stoichiometric $YBa_2Cu_3O_7$ is P_{mmm} (D_{2h}) using standard short and Schoenflies notation [47]. The $\vec{k} \approx \vec{0}$ long wavelength vibrational modes of the $YBa_2Cu_3O_7$ crystal are given by the $3N = 39$ normal modes of the unit cell. Classification of these normal modes in terms of symmetry can be achieved by determining the number of modes that transform as each irreducible representation of the D_{2h} point group of the unit cell. In Mulliken or chemical notation, the resulting classification can be written as [47]:

$$\Gamma_{vib} = 5A_g + 5B_{2g} + 5B_{3g} + 8B_{1u} + 8B_{2u} + 8B_{3u}. \tag{3.1}$$

where the 15 modes denoted with the subscript g (gerade) are even while the 24 remaining u (ungerade) modes are odd with respect to inversion symmetry. The unit

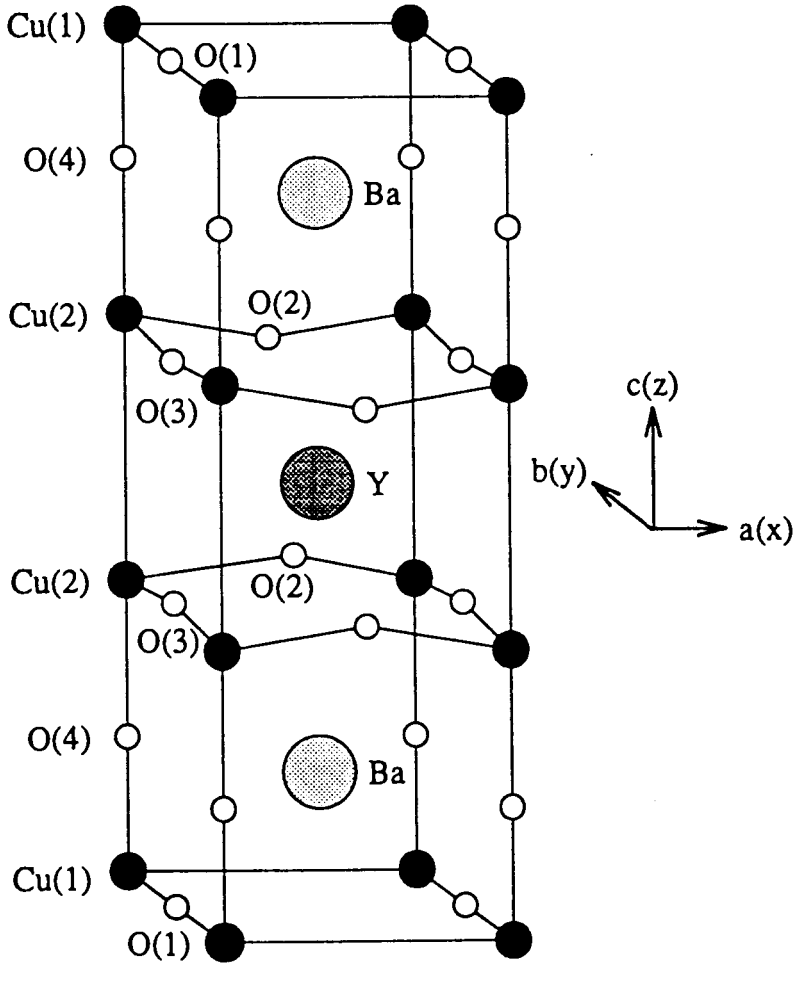

Figure 3.3: $YBa_2Cu_3O_7$ unit cell

cell has a center of inversion, 21 of 24 odd u modes are infrared active, the other three u modes acoustic (B_{1u}, B_{2u}, B_{3u}) and the 15 even (g) modes Raman active.

3.4 Infrared reflectance of $YBa_2(Cu_{1-x}Zn_x)_3O_{7-\delta}$

Far-infrared reflectance measurements were performed with a Bruker 113V Fourier spectrophotometer in the range from 100 cm^{-1} to 700 cm^{-1}, as a function of temperature over the full range of 10K to room temperature. Samples were mounted in a circulating helium cold finger cryostat whose temperature could be varied from 10K to 300K, as detailed in Chapter 2. The infrared radiation was incident on the sample at approximately normal incidence and was nominally unpolarized. Absolute reflectivities were obtained by using a stainless steel mirror as reference. The relative precision of the reflectance was estimated to be at least 0.1% for all temperatures; because of the possibility of systematic errors due to several effects related to the sample geometry, the relative accuracy of the measurements is no better than 1%. The spectra presented here were taken on several samples and were found to be unchanged in a number of remeasurements taken over a two month period.

To avoid contamination, infrared measurements on the samples were carried out without any surface preparation.

Fig. 3.4.a gives the far-infrared reflectance spectra in superconducting states for the three $YBa_2(Cu_{1-x}Zn_x)_3O_{7-\delta}$ samples, where x = 0% 3% and 4%. Fig. 3.4.b shows the spectra for the same samples in normal states. In normal state, the reflectance of the undoped samples decreases gradually from $\sim$ 0.8 at 50 cm^{-1} to 0.3 at 700 cm^{-1}. At the lower temperatures, i.e., in the superconducting states, the general shapes of the spectra remain the same but the reflectance is slightly enhanced at

low frequency range 50 to 200 cm^{-1}. Above about 200 cm^{-1}, the reflectivities of the Zn-doped samples become slightly lower than those in normal states. This behavior indicates that the superconductivity influences the dynamic conductivity. The spectra of the $x = 3\%$ and $x = 4\%$ samples also indicate that the reflectance decreases as the Zn content increases.

Fig. 3.5 presents the ratio of reflectance of the three samples in the superconducting states to those in the normal states (R_s/R_n). It shows a systematic decrease as the Zn concentration increases. The ratios also give a remarkably rich spectra with feature lines at 155, 190, 270, 310, and 560 cm^{-1}.

The infrared reflectance spectrum of the pure $Y123$ compound is in good agreement with the results reported by other groups on polycrystalline samples, e.g., [58]; and its main phonon peaks are in similar locations and their relative strengths are similar to those of single crystal samples [59] [64] [63] and thin films [71]. However, it should be noted that the intensity of the reflectance from polycrystalline ceramics, including the results reported here, is usually lower than those from single crystals and highly orientated films. This difference is mainly due to the roughness of our samples' surface, and the random orientation of anisotropic crystal grains in the ceramic samples.

We shall consider the three excitations principally responsible for the observed optical activity: lattice vibrations, superconducting excitations and free carrier effects.

3.5 Phonon Assignments

Lattice vibrations in high-T_c cuprates have been the subject of numerous studies. Besides obtaining the phonon parameters (frequencies, linewidths, spectral strengths)

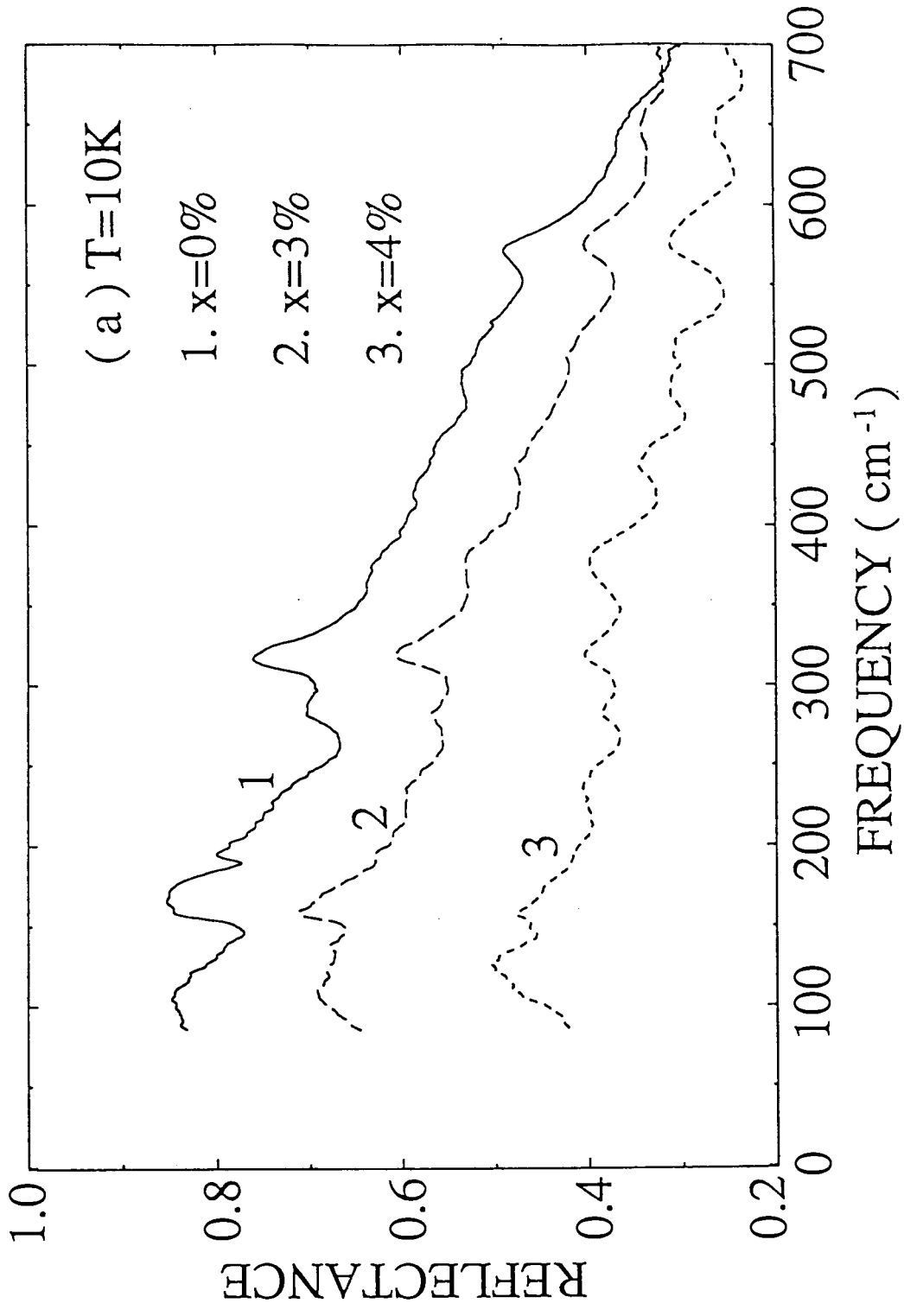

Figure 3.4.a: The far-infrared reflectance spectra in superconducting state for the three $YBa_2(Cu_{1-x}Zn_x)_3O_{7-\delta}$ samples.

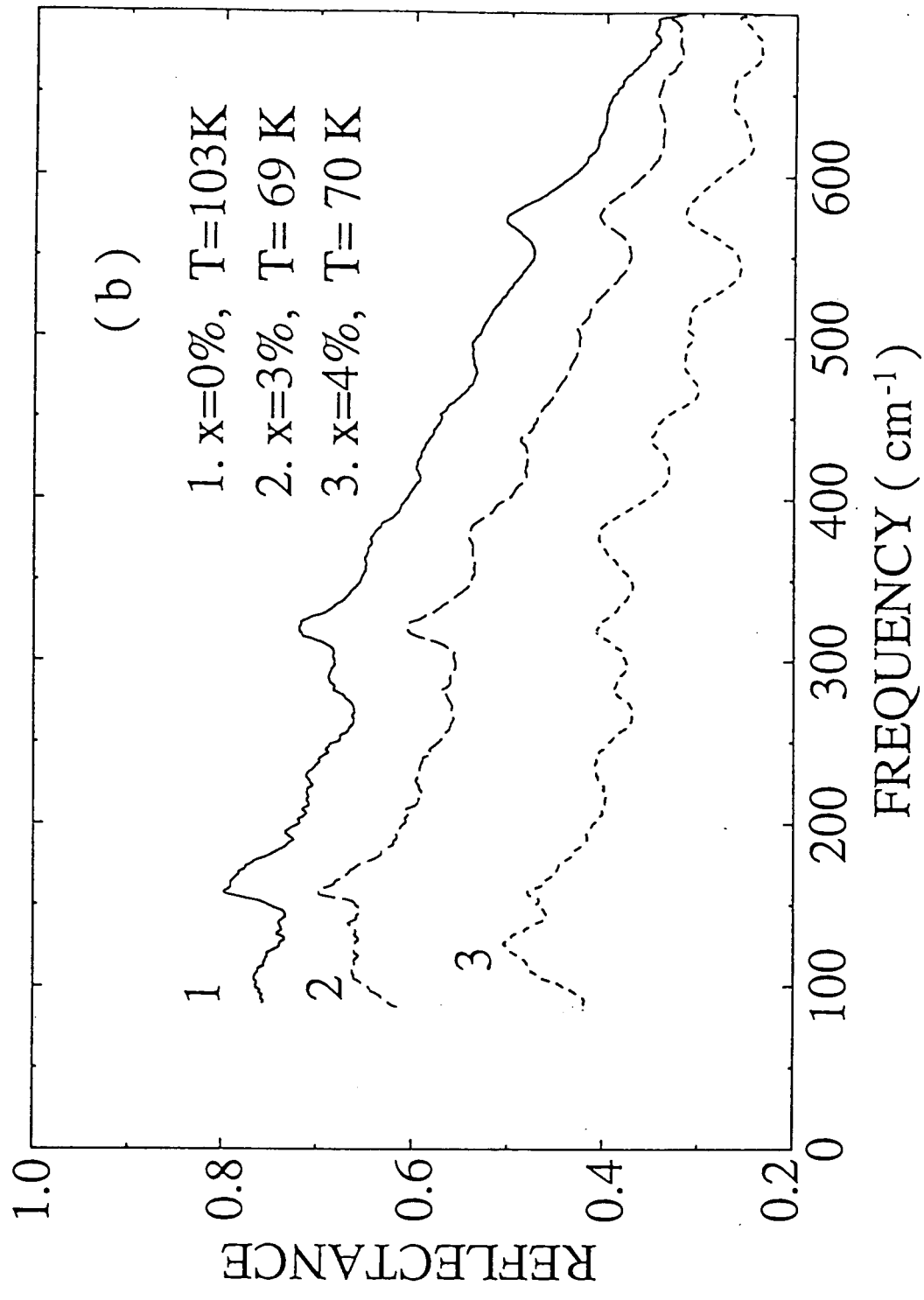

Figure 3.4.b: The far-infrared reflectance spectra in normal state for the three $YBa_2(Cu_{1-x}Zn_x)_3O_{7-\delta}$ samples.

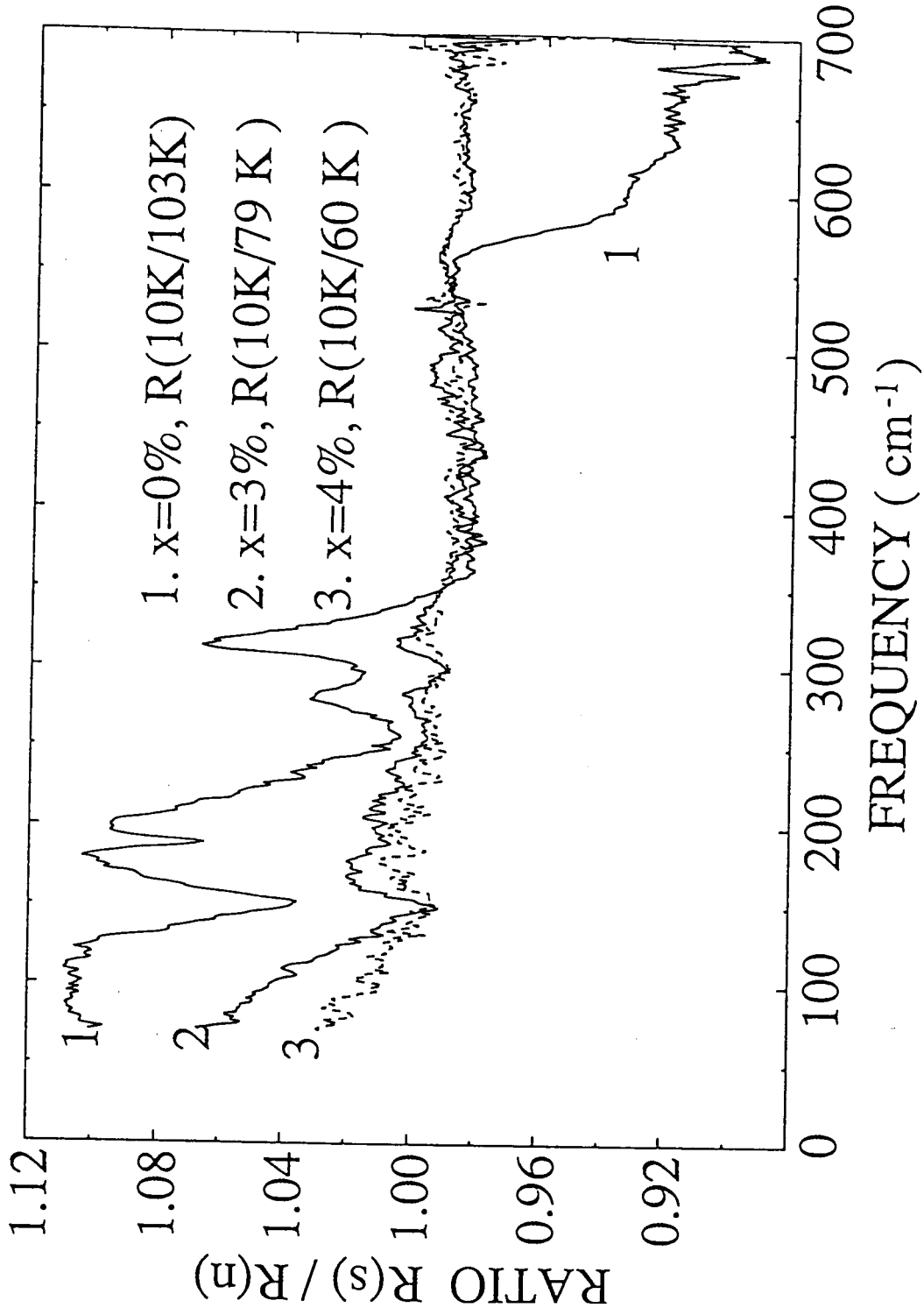

Figure 3.5: R_s/R_n, ratio of the superconducting to normal reflectivities (1) $R(103K)/R(70K)$ for pure sample, (2) $R(80K)/R(54K)$ for the 3% Zn-doped sample , and (3) $R(70K)/R(40K)$ for the 4% Zn-doped sample.The far-infrared reflectance spectra in normal state for the three $YBa_2(Cu_{1-x}Zn_x)_3O_{7-\delta}$ samples.

these studies aim at the investigation of electron-phonon coupling when moving in temperature across the superconducting transition. We should recall here that optical techniques (e.g., Raman and ir spectroscopy) only reveal phonons near the center of the Brillouin zone. A more complete picture can be obtained, in principle, with inelastic neutron scattering [52]. Existing neutron data, however, do not have the accuracy of optical data as far as phonon frequencies are concerned. We assign the features in our measured spectra by comparing them with theoretical lattice dynamic calculations and experimental results, including results from infrared and inelastic neutron scattering, by other groups [51] [52].

As discussed in Chapter 2, one of the most common methods for obtaining the frequency-dependent dielectric function and other fundamental optical properties is to calculate them from a measured reflectance $R(\omega)$, and its phase $\theta(\omega)$ by using a Kramers-Kronig transformation . Since the Kramers-Kronig integral requires knowledge of the reflectance at all frequencies, $R(\omega)$ must be extrapolated beyond the measured frequency range. The uncertainties in these extrapolations can result in large errors in $\theta(\omega)$ which are subsequently involved in the calculation of the dielectric response. In our case, reflectance were extrapolated for the frequency ranges below 100 cm^{-1} and above 700 cm^{-1}. Several other factors such as the uncertainty of the absolute values of reflectivities, the strong anisotropy of layered $Cu-O$ superconducting materials, and random orientation of crystal granules, make the Kramers-Kronig results less useful for polycrystalline samples. But we can still use the Kramers-Kronig analysis to extract some phonon information since the locations and relative strengths of the features are not dependent on the nature of the extrapolation. Fig. 3.6 presents the real part of frequency-dependent conductivity calculated by a Kramers-Kronig transformation of the data in Fig. 3.4.a. Fig. 3.6 also shows that

the calculated conductivity decreases sharply with increasing Zn content, as expected from the decreases in reflectance.

It has been concluded in [33] that the substitution of divalent Zn does not affect the concentration of oxygen and that Zn merely replaces the Cu(2) within the CuO_2 plane based on neutron diffraction results. However, it was reported that Zn impurities were also found at Cu(1) sites [56]. Thus in our analysis of the vibrational modes, we will consider the effects of the Zn substitution for both Cu(1) and Cu(2) cases.

The presence of free carriers increases the overall background reflectance and can "screen" the features in the spectrum which stem from the vibrational modes, reducing the apparent strength of those features. In our discussion of the effects of Zn impurities on the optical spectra, we must take into account three different effects: 1) Zn substitution decreases the infrared conductivity and it can reduce screening and enhance the apparent strength of optical features; 2) Zn substitution for Cu(2) will decrease the strength of those phonons whose eigenvectors have significant motion at Cu(2) sites; impurity modes of Zn at those sites will have energies different from the original phonons; 3) Zn substitution (at any site) will further reduce the degree of translational symmetry in the lattice; these defect structure crystals already deviate significantly from perfect symmetry. A result of this further reduction in symmetry can be increased optical activity by modes (e.g. Raman-active modes) that are symmetry-forbidden in the perfect crystal. We shall see that, in most cases, the observed results can be explained in terms of these three effects.

Of the 21 infrared-active phonons in $YBa_2Cu_3O_{7-\delta}$ according to group theory, six (154 cm^{-1}, 191 cm^{-1}, 283 cm^{-1}, 315 cm^{-1}, 566 cm^{-1} and 637 cm^{-1}) are clearly visible in both our far-infrared reflectance and the conductivity spectra of $x = 0\%$

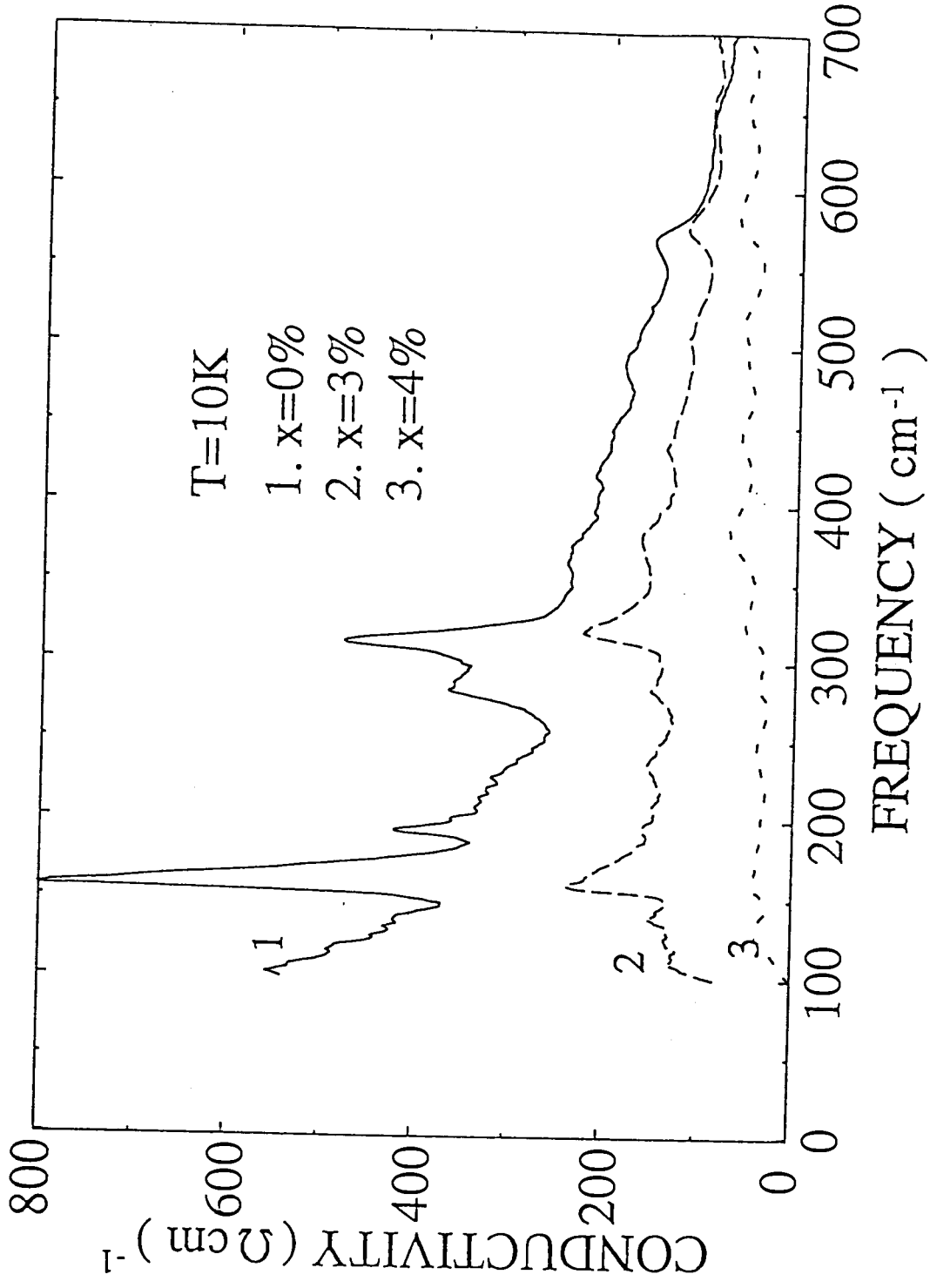

Figure 3.6: Conductivity of $YBa_2(Cu_{1-x}Zn_x)_3O_{7-\delta}$ from 100 to 700 cm^{-1} at 10 K.

sample, as summarized in Table 3.1. The positions of phonons are determined from the peaks in both reflectance and conductivity spectra of the undoped $YBa_2Cu_3O_{7-\delta}$ sample. Strength is measured with respect to the background reflectance attributed to free carrier effects. The frequencies are in reasonable agreement with recent reports of far-infrared reflectance measurements on thin films of $Y(Pr)Ba_2Cu_3O_{7-\delta}$ [71] and on single crystal $GdBa_2Cu_3O_{7-\delta}$ [63] as given in Table 3.1. Also shown in Table 3.1 are the symmetries and ions that participate most strongly in the modes. These were inferred from the corresponding modes in the single crystal studies. Our assignments of phonon features agree with the results from inelastic neutron scattering experiments [46]

As shown in Fig. 3.6, the strengths of the phonons at 154 cm^{-1}, 191 cm^{-1} and 315 cm^{-1} become weaker with increasing x, whereas the lines at 367 cm^{-1}, 566 cm^{-1} and 637 cm^{-1} become stronger. In addition, new broad features appear at 225 cm^{-1}, 440 cm^{-1} and 492 cm^{-1}, as Zn impurities are added.

It has been concluded [68], [71] that the 154 cm^{-1} line, which has the largest oscillator strength in the far-infrared spectra, arises from a symmetric Cu(1)-O(1) chain vibration . It is clear from Fig. 3.4.a and Fig. 3.6 that the width of the 154 cm^{-1} mode of the $x = 3\%$ sample is approximately the same as in the pure sample but the strength decreases very sharply as x increases. This strong effect of Zn would contradict the assignment [68] mentioned above if Zn occupies only Cu(2) sites. It seems evident that the Zn impurities replace both Cu sites [71].

The phonon feature at 191 cm^{-1} observed in the pure 1-2-3 sample almost disappears in the Zn-doped samples. This provides an useful information in the assignment of this mode. Previous researchers [68]-[73] have assigned the line at 191 cm^{-1} to a

Table 3.1: Phonon Assignment

Symmetry	Vibration	This work $x = 0$ Frequency	Homes *et al.* [64][a] (cm^{-1})	Železny *et al.* [63][b]
B_{1u}	$Cu(1)$, $O(1)'$	154	153	148
B_{1u} or B_{2u}	Cu, Y, O	191	195	176
B_{1u}	$Cu(1)$, $O(1)$	283	287	288
B_{1u}	$Cu(2)$, $O(2)$	315	314	320
B_{1u}	$O(1)$, $O(4)'$	566	557	560
?	?	637	630	620
B_{2u} or B_{3u}	?	225	-	227
A_g or B_{2u}	$Cu(2)$, $O(2)$, or $O(4)$	440	-	420
B_{2u} or B_{3u}	$O(4)$, or $Cu(2)$, $O(2)$	492	-	493

The prime denotes a 180^0-out-of-phase-vibration. E.g., $O(1)$, $O(4)'$ indicates that $O(1)$ vibrates in-phase and $O(4)$ vibrates out-of-phase with them.

[a] $YBa_2Cu_3O_{7-\delta}$ single crystal.
[b] $GdBa_2Cu_3O_{7-\delta}$ single crystal.

B_{1u} vibration involving Y and O, based primarily on frequency shifts which is caused by substitutions of Y by a rare earth. From our data, we conclude that this mode must also involve the Cu(1) or Cu(2) sites, because Zn substitution, on those sites, dramatically changes this mode. This conclusion is reinforced by a recent published results on lattice vibrations of Y(Pr)-123 by J. Humlicek et al. [71]. A number of factors could cause the decrease of the 191 cm^{-1} mode as Zn is added in the $Y123$ system. For example, with reference to the calculated eigenvectors, the 191 cm^{-1} line could be a B_{2u} symmetry mode, like the mode calculated [71] to lie at 201 cm^{-1} which involves Cu(2) or at 187 cm^{-1} by Bates [75] which involves Cu(1) or Cu(2).

The mode at about 283 cm^{-1} in $YBa_2Cu_3O_7$ was originally assigned to a plane-oxygen mode which is silent in $YBa_2Cu_3O_6$. It is recently reassigned as a mode of chain-oxygen vibrations based on the experiment for site -selective oxygen-substitution of O^{18} for O^{16} by Ye and McCall et al [76] and results from neutron scattering experiments by N. Pyka et al [70]. Our results do not contradict this assignment, since our spectra do not show an apparent change in the phonon strength which corresponds to a change in the microscopic oscillator strength as Zn concentration x increases, i.e., the mode does not involve in the vibration of copper in the plane.

The sharp decrease in strength of the strong mode at 315 cm^{-1}, as x increases, is a clear indication that both Cu(2) and Cu(1) sites are involved in this mode. This does not support the earlier assignment as either a B_{3u} vibration [73], [74] involving only O(4) and O(1) or as a B_{1u} vibration [75] of Y-O and Ba-O. Instead, we find this line belongs to the doublets of 283 cm^{-1} and 315 cm^{-1}, and is associated with $Cu-O$ plane bending modes. The results reported by Crawford et al., based on their infrared measurements on isotropically substituted samples [68], show no contradiction with

our assignment on this line.

The mode at 566 cm^{-1} becomes somewhat stronger as x increases. This is consistent with the conjecture [73], [74] that its optical activity is defect-induced, stemming mainly from out-of-phase motion of the apical O(4) and the chain O(1) oxygens. Other researchers [59], [68] have suggested that this mode corresponds to Cu-O stretching vibrations between the Cu-O chains and the Cu-O planes.

A number of other features appear in the reflectance spectrum as x increases; bands are centered at 225 cm^{-1}, 440 cm^{-1} and 492 cm^{-1}. In all cases the modes are very weak or non-existent in the pure 1-2-3 compound. As we discussed earlier, the high T_c copper oxide materials are highly anisotropic. In low frequency range, optical measurements on theses materials show metallic reflectance if the surface of the sample is dominated by $a-b$ plane and insulating low reflectance in the c direction. Usually phonon bands from $a-b$ planes are invisible because the high conductivity background screening effects on the phonons. In our case, the low frequency reflectance is sharply reduced with Zn-doping. Therefore, the screening by charge carries in $a-b$ planes should be also decreased. The phonon bands from $a-b$ planes then should be seen superimposed on the electronic background. The extra lines observed from the $Zn-doped$ spectra could be then assigned as the phonons arising from $a-b$ planes. Comparing the recent measurements on $a-b$ plane single crystal $GdBa_2Cu_3O_{7-\delta}$ by V. Železny et al. [63], we find these lines are nearly in the same positions of the phonon bands occurred in their spectra on $a-b$ plane measurements.

Symmetry breaking induced by Zn defects could be another reason for causing the extra lines. The lines at 440 cm^{-1} and 492 cm^{-1} in the reflectance spectra of our Zn-doped samples could be the same lines as seen at about 440 cm^{-1} and 502 cm^{-1}

in Raman spectrum [77], [71].

3.6 Search for the Superconducting Gap and doping effects

The existence of a superconducting energy gap in the high-T_c superconductors has been hotly debated. As discussed in Chapter 1, a simple s-wave BCS model has a complete gap of width $2\Delta_0$ around the Fermi energy with $2\Delta_0/k_BT_c \cong 3.5$ for weak coupling or higher for stronger coupling. This energy gap is evident in the far-infrared-microwave range for low-T_c superconductors. Beginning with the pioneering work of Glover and Tinkham [82], infrared spectroscopy [83], [84], [85], [86] has provided the most fundamental and versatile probe of the superconducting energy gap.

Infrared studies [90, 89, 87, 91, 92, 93] on high-T_c materials reveal a feature at $\sim (8-12)k_BT_c$, originally thought to be the gap. However, there is increasing evidence showing the contrary of the interpretation [93]. In high-T_c superconductors the gap might not show up in the infrared spectrum for several reasons. First, the scattering rate of the charge carriers may be low relative to the superconducting energy gap ($\Gamma \ll 2\Delta_0$), making hard to detect a superconducting gap by infrared spectroscopy [90]. Second, there seems to be a temperature independent contribution to the oscillator strength in this frequency range, overlapping and possibly masking a weak gap feature. It is also possible that the description of the superconducting state cannot be put in a BCS framework.

We can experimentally test the first possibility by adding Zn to the system which could enhance the impurity scattering rate to produce better circumstances for the observation of the spectroscopic gap. To examine the change in reflectance

at the normal-to-superconducting transition, it might be useful to form the ratio, $R_s(T)/R_n(T)$, of the reflectance in the superconducting state to that in the normal state. Fig. 3.5 shows the ratios of the three samples. It is clear that major increases in the strengths of the phonon features present for $x = 0\%$ occur below the transition temperature, as noted previously by Collins et al.[60]. For $x > 0\%$, there are smaller changes in strengths of the phonon features. The a-b plane related features at 225 cm^{-1}, 440 cm^{-1} and 492 cm^{-1} are unaffected by the superconducting transition. The regions of enhanced reflectance, below about 220 cm^{-1} are present in all three samples, albeit with decreased enhancement for $x > 0\%$.

We note that there is no sizable shift of any feature in the reflectance (c.f. Fig. 3.4.a and Fig. 3.4.b) or the reflectance ratio (c.f.Fig. 3.5) as x is increased. This is the case despite the fact that T_c drops from 90K for $x = 0$ to 49K for $x = 4\%$. Many previous studies have related [60], [78]-[80] the enhanced reflectance below 200 cm^{-1} to an energy gap at that energy. Our results, which show that the enhanced reflectance persists, despite the large decrease in T_c, suggest either that there is no detectable gap at this energy or that the gap does not depend on the transition temperature, as required if BCS theory describes the superconductivity. Further discussion of the superconducting gap will be presented in Chapter 6 of infrared study on Ni-doped high quality single crystal $YBa_2Cu_3O_{6.95}$.

Another well known feature, which is related to the superconducting gap interpretation, is a prominent non-Drude notch-like absorption feature occurring in the $a-b$ plane reflectance of $YBa_2Cu_3O_{7-\delta}$ near $400cm^{-1}$ [126] [87]. This structure has been the focus of much discussion. It has been variously attributed to the superconducting energy gap and to phonons. Z. Schlesinger et al. [87] interpreted it as belonging to a superconducting gap according to their experimental results on single crystals.

Recently M. Reedyk et al. claimed that the strong absorption structure is correlated with $c-axis$ longitudinal optical (LO_c) phonons [88]. However, this characteristic notch in the reflectance is very difficult to see in our spectra both in superconducting and normal states, shown in Fig. 3.4.a and Fig. 3.4.b. The random orientation of ceramic samples could be the cause of the absence of the $a-b$ plane notch, according the effect discovered by Reedyk et al.. Another reason for the notch feature not showing up could be due to the presence of phonon structure in this spectral region.

One other result that should be mentioned is that the overall far infrared reflectance decreases as x increases. This implies a decrease in conductivity, confirmed by Kramers-Kronig analyses of our data in Fig. 3.6. The absolute magnitude of the calculated conductivity is about an order of magnitude lower than those from single crystal samples, e.g. Ref. [63]. This is directly related to the lower reflectance which is, in turn, believed due to incomplete orientation of the textured surface of the sample. The addition of Zn causes further reduction in the absolute magnitude of the reflectance and in the calculated conductivity. For $x = 3\%$, and especially $x = 4\%$, the low frequency conductivity is less than in the undoped sample and the low frequency conductivity loses its strong, metal-like frequency dependence. The phonon peaks, however, maintain their identities and their strengths have a variety of different dependencies on Zn concentration, as noted above. This suggests either that a free carrier model is totally inappropriate to describe these materials or that very strongly frequency-dependent damping processes are present. Further study is clearly needed.

The reason that the intensity of each phonon feature in the spectra is so sensitive to, and systematically changes with, small amounts of Zn impurity is not clear. It has been proposed that a high oscillator strength can be attributed to strong electron

vibrational coupling. Here we speculate that Zn with one more electron replacing at Cu(2) sites changes the local electronic density and induces a random potential which may affect the symmetric vibrational modes of the Cu-O system. This effect could make the infrared-inactive phonons become active in pure $YBa_2Cu_3O_{7-\delta}$ change their intensities, or create new features (225, 367, 440 and 492 cm^{-1} in Fig. 3.6). It is interesting to note that such a small content of Zn impurities has a major effect on the overall reflectance and on T_c. This provides a further confirmation that the superconductivity in this material is very sensitive to local disorder caused by substitution at the Cu sites, on which the Zn ion is situated.

3.7 Conclusions

In conclusion, the far-infrared spectra of $YBa_2(Cu_{1-x}Zn_x)_3O_{7-\delta}$ ceramic samples have been presented and discussed in the normal and superconducting state for Zn concentrations up to $x = 4\%$.

In the normal state, the infrared-active modes in the spectra have been studied and assigned. The changes of intensities of the phonons are found to be related to the Zn doping concentration. In the superconducting state, there is no clear evidence of a superconducting energy gap from our experimental results in the $YBa_2(Cu_{1-x}Zn_x)_3O_{7-\delta}$ system. The effects of inserting Zn^{2+} ions in the $YBa_2Cu_3O_{7-\delta}$ lattice lead to a strong depression of reflectance in low frequency range. This suggests either that a free carrier model is totally inappropriate to describe these materials or that very strongly frequency-dependent damping processes are present. The relationship between the superconducting transition and FIR properties of the Zn-doped compounds reported here is of importance and worth further investigations,

e.g., polarized optical measurements on high quality single crystal samples could provide more precise information about the strong anisotropy and doping properties of the materials.

Chapter 4

Superconducting $Bi_{2.125-x}Pb_xSr_{1.875}CuO_{6+y}$

4.1 Introduction

$Bi_2Sr_2CuO_{6+y}$ ($Bi-2201$) is a member of the Bi-based cuprate superconductor family with a T_c of approximately $10K$. It shares structural elements with $La_{2-x}Sr_xCuO_{4+\delta}$, $YBa_2Cu_3O_{7-\delta}$, and $Bi_2Sr_2CaCuO_{6+y}$ in that the crystal structure is body-centered tetragonal unit cell. On the other hand, unlike $YBa_2Cu_3O_{7-\delta}$ and $Bi_2Sr_2CaCuO_{6+y}$, in which double CuO_2 plane layers are the common structure, $Bi_2Sr_2CuO_{6+y}$ has only one CuO_2 plane layer with a BiO-SrO-CuO-SrO-BiO sequence. Initial studies [121] indicate that the transition temperature T_c of superconducting parent compound $Bi_2Sr_2CaCuO_{6+y}$ decreases by doping lead into bismuth sites. It has also been found that various defects including vacancies, substitutions, and atomic displacements exist in the interlayer structure [118] in the Bi-systems. Although such progress has been seen in the fundamental study of the bismuth compounds, some of their properties, e.g., the normal-state excitation spectrum, and the manner in which the spectra develop from the insulating phase as a function of doping [17],

are still not fully understood. To address these questions, here we report a progression of the behavior, from metallic and superconducting to insulating, in the Ca-free $Bi_{2.125-x}Pb_xSr_{1.875}CuO_{6+y}$ series with increasing the concentration of doping lead, which we have investigated optically using polycrystalline samples.

In this chapter, we present the results of infrared reflectance measurements from 50 to 10,000 cm^{-1} on the single Cu-O layer system $Bi_2Sr_2CuO_{6+y}$ and its lead-doped counterparts and their phonon spectra determined from the real part of the conductivities, obtained by Kramers-Kronig analysis. This is an interesting domain because for the pure $Bi_2Sr_2CuO_{6+y}$ compound has a pseudo-tetragonal structure with an incommensurate structural modulation [123], while adding low concentrations of lead in place of bismuth decreases the modulation. At higher lead concentrations, there is a transformation to an orthorhombic structure and no evidence of structural modulation. Throughout these structural changes, up to $x \sim 0.2$, the superconducting transition temperatures remain low, on the order of 10K; above this concentration, the samples are insulators. On the basis of our experimental data and the results of group theoretical analysis and model calculations, we discuss the features observed in the reflectivity spectra in the phonon excitation region. We should point out here that at the time we started the project of experiments on $Bi_{2.125-x}Pb_xSr_{1.875}CuO_{6+y}$, ceramics were the only samples available to us. In the last section of the chapter, we discuss very recent infrared studies on single crystals of the Bi-based materials and update our understanding of these materials.

4.2 Preparation and Characterization of $Bi_{2.125-x}Pb_xSr_{1.875}CuO_{6+y}$

The samples were prepared using the rapid solidification technique [37]. They were prepared and characterized by Dr. J. Akujieze et al. at Illinois Institute of Technology. Starting materials were first weighed in the proper ratios and then were melted in an alumina crucible at 940 ^oC for 40 minutes in an electric furnace. The subsequent melt was quickly poured onto a copper plate, which was preheated to a temperature above room temperature (200 ^oC), and splat quenched between the copper plate and a copper hammer. The average thickness of the resulting samples was of the order of 2 mm. The splat quenched samples (glassy precursors) were then annealed at 840 ^oC in air and furnace cooled.

Phase identification was carried out using an automated General Electric XRD diffractometer and $Cu\ K\alpha$ radiation. Diffraction patterns were acquired over the $3^o < 2q < 70^o$ range in steps of 0.05^o for counting times of 10 s per step. Impurity phases in the samples were deduced from the diffraction spectra by comparison to individual X-ray patterns of standards and phases reported in the literature. Lattice parameters were obtained by Rietveld refinement of the diffraction spectra [38].

The X-ray diffraction patterns shown in Fig. 4.1 indicate that all of the samples are essentially single phase with the compositions of the undoped sample and the sample with Pb-doping $x = 0.05$ in the pseudotetragonal phase with intense modulation peaks [39]. The lead content of 0.1 appears to be a critical composition after which there is a structural transition from the pseudotetragonal to a more definite orthorhombic phase which shows no modulation [40]. Hence both compositions 0.1 and 0.15 which showed a sharp decrease of the modulation lines were refined assuming an orthorhombic unit

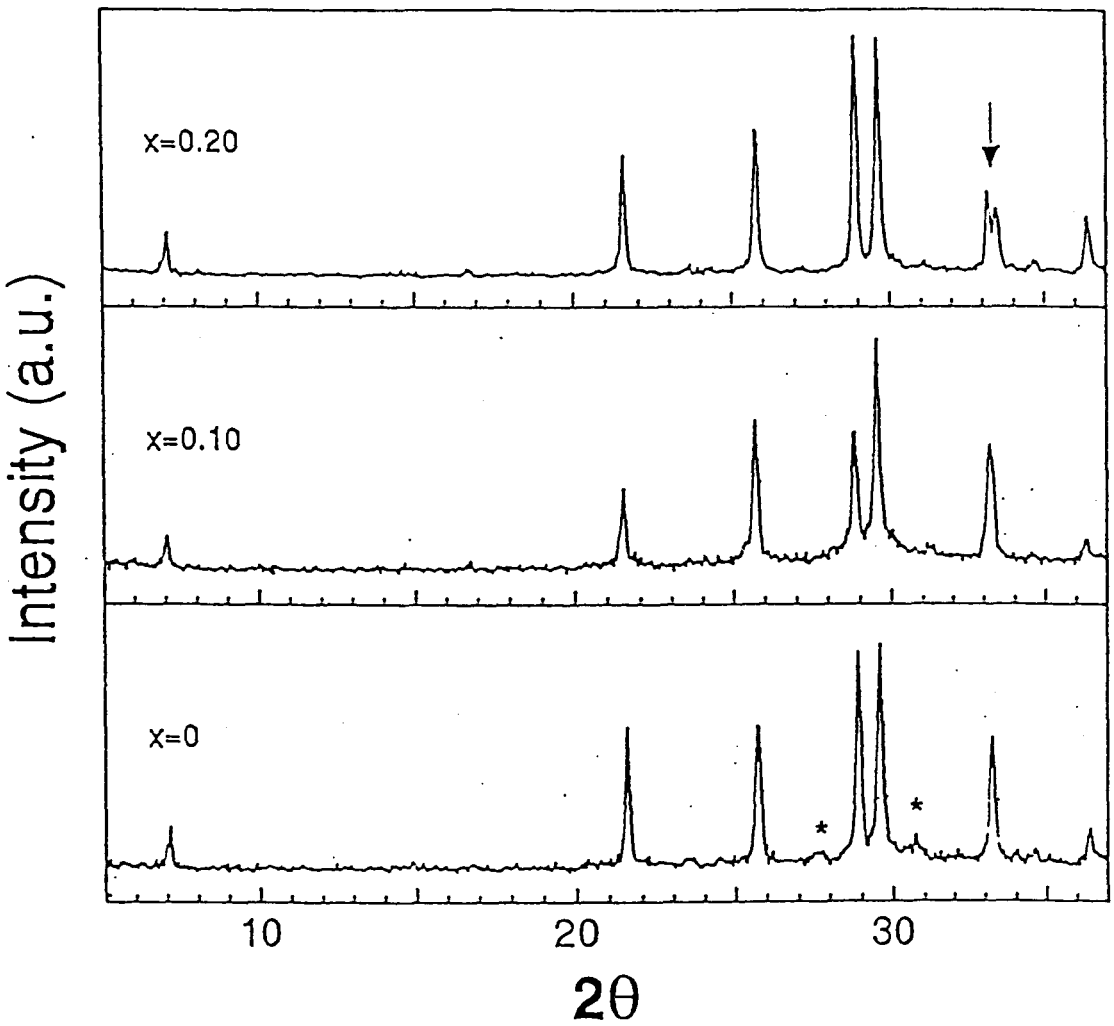

Figure 4.1: X-ray diffraction of $Bi_{2.125-x}Pb_xSr_{1.875}CuO_{6+y}$. * indicates the modulation peaks in the pseudotetragonal phase when $x = 0$, $\downarrow$ indicates the impurity peak by lead substitution (ref. [41]).

cell. It is commonly agreed that Pb impurities substitute Bi in Bi-2201 structure [41]. The superconducting $T_c's$ for these samples decrease with lead content, in agreement with other reports in the literature. [40]. The Pb-doped samples with $x = 0$, 0.05 and 0.10 lead content exhibited superconducting transitions of $7.6K$, $7.35K$ and $6.8K$ respectively, whereas a sample of $x = 0.2$ is an insulator.

4.3 $Bi_2Sr_2CuO_6$ Crystal Structure and Symmetry

The ideal $Bi_2Sr_2CuO_6$ $(Bi-2201)$ structure [124] has a body-centered tetragonal unit cell which contains a single $Cu-O(2)$ plane, perpendicular to the c-axis of the structure, surrounded on each side by a $Sr-O(1)$ layer and then a $Bi-O(3)$ layer, as illustrated in Fig. 4.2. The long and weak $Bi-O(3)$ bond parallel to the c-axis results in very weak interlayer bonding and mica-like mechanical behavior in all the Bi superconductors.

The structure of $Bi_2Sr_2CuO_{6+y}$ has been described as "pseudo-tetragonal" – it is orthorhombic but with only very slight deviations from tetragonal structure, as shown in Fig. 4.2. Its dimention is approximately $3.9 \times 3.9 \times 24.4$ Å. The single Cu-O plane and the octahedral coordination of the Cu make this $Bi_2Sr_2CuO_6$ structure very similar to the $(La_{2-x}Sr_x)CuO_4$ and $TlBa_2CuO_6$ (Tl-2201) superconductors.

From group theory and previous work by Burns et al. [125], the vibrational normal modes of tetragonal $Bi_2Sr_2CuO_6$ can be classified as $A_{2u} + E_u$ (Acoustic), B_{2u} (Silent), $4A_{1g} + 4E_g$ (Raman-active), and $5A_{2u} + 6E_u$ (IR - active), where A/B and E modes correspond to an atomic motion perpendicular and parallel to the CuO_2 plane, respectively. The $5A_{2u} + 6E_u$ ir-active modes involve mainly the motion of Sr, Bi, $O(1)$, $O(2)$, and $O(3)$ atoms.

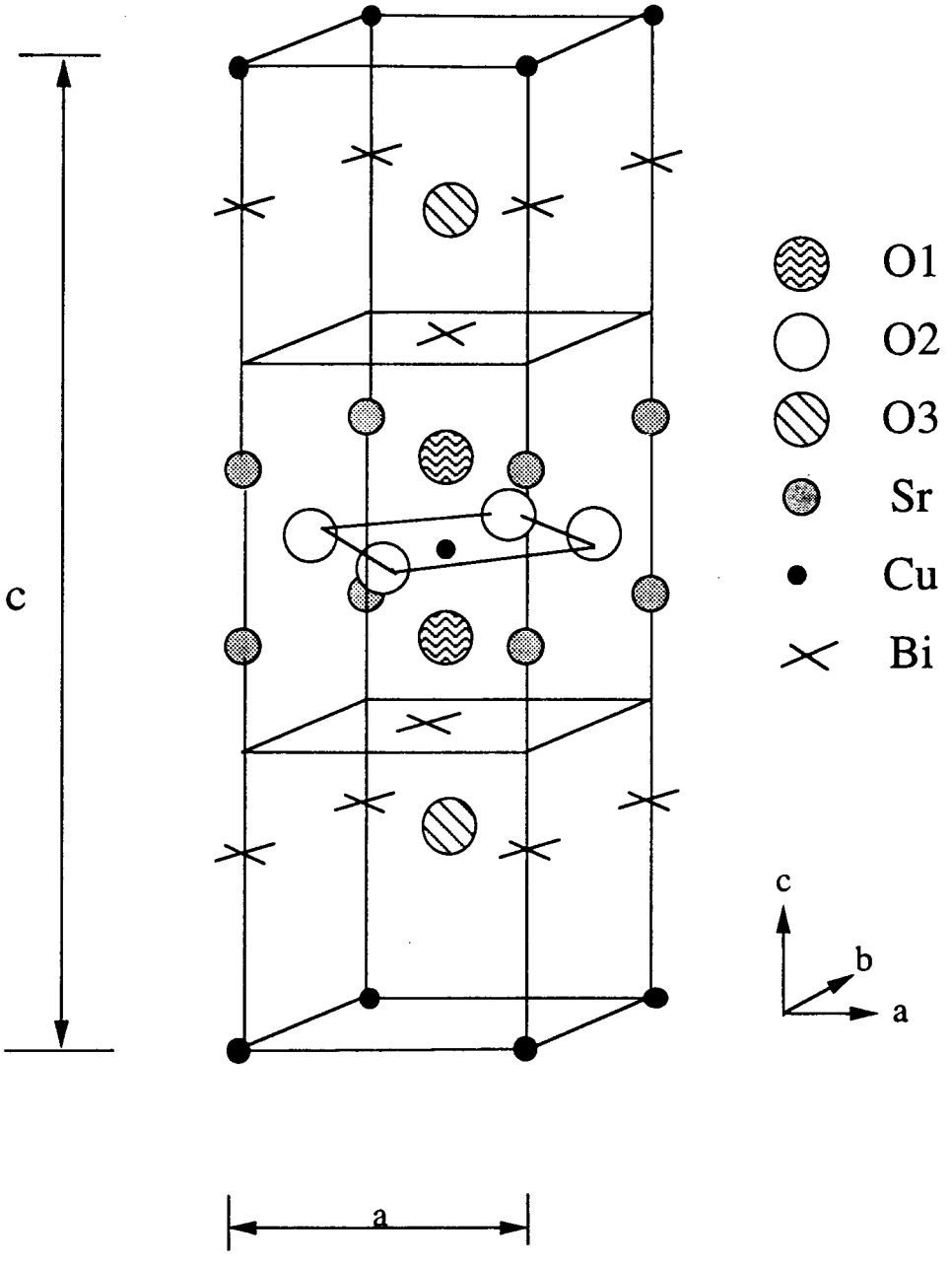

Figure 4.2: $Bi_2Sr_2CuO_6$ unit cell

Incommensurate modulation is observed along the a-b plane of the structure of $Bi_2Sr_2CuO_{6+y}$. The implications of this on the interpretation of our spectra are profound. We should observe more than the expected number of ir-active modes for two reasons: a) the degeneracy of the E modes in the a-b plane will be lifted, and b) the selection rules that prevent the observation in the infrared of Raman-active modes will be weakened. Pb-doping and changes in oxygen stoichiometry increase the disorder and thus further increase the tendency for optically inactive modes to become active. An alternate explanation of the observed "excess" of modes is the presence of other phases and/or other compounds in our samples. This was ruled out by examination of the x-ray spectra and observation that all the modes occur, with systematically varying strengths, in all our sample spectra.

4.4 Results and Discussions

Far-infrared reflectance measurements were performed using a modified Bruker $IFS-113\ V$ Fourier transform spectrophotometer in the range 50 - 10,000 cm^{-1}. The infrared radiation was incident on the sample at approximately normal incidence. For details, see Chapter 2. The absolute reflectivity was obtained using a stainless steel mirror as reference. To avoid contamination, our measurements were carried out without any surface treatment on the samples. All measurements were performed at room temperature.

In Fig. 4.3 we show the far-infrared reflectance spectrum of $Bi_2Sr_2CuO_{6+y}$ together with the spectra of its lead-doped counterparts, $Bi_{2.125-x}Pb_xSr_{1.875}CuO_{6+y}$ with x = 0.05, 0.10, and 0.15, in the frequency range of 50 to 700 cm^{-1}, at 300 K. Fig. 4.4 shows the real part of the conductivity of the four samples obtained by

Kramers-Kronig analysis of the reflectance data of Fig. 4.3, with extrapolations to higher and lower frequencies; results in the region of interest were virtually independent of the precise nature of the extrapolations. Phonon frequencies reported in this thesis correspond to maxima in the conductivity spectra.

The spectra shown in Fig. 4.4 show nine lines, including two very weak lines at 120 and 210 cm^{-1}. All nine are listed in Table 4.1 along with proposed assignments. Mode assignments were based on comparisons with calculated and experimentally observed spectra of structurally similar high-T_c materials and according to group theoretical considerations, as described below. We concentrate mainly on the $x = 0$ results and use the effects of Pb doping to help refine our arguments.

The most useful theoretical work for assigning the modes is a lattice- dynamical calculation of the normal modes on $Tl_2Ba_2CuO_6$, $Tl_2Ba_2CaCu_2O_6$ and related compounds by A. D. Kulkarni et al [126]. $Bi_2Sr_2CuO_6$ ($Bi-2201$) and $Tl_2Ba_2CuO_6$ (Tl-2201) have very similar crystal structures. The introduction of Ca in $Tl_2Ba_2CaCu_2O_6$ (Tl- 2212) results in the addition of a second Cu-O plane and a structure similar to that of $YBa_2Cu_3O_7$. Another useful work, by the same group [127], calculates the modes of $Bi_2Sr_2CaCu_2O_6$ ($Bi-2212$) whose structure is the same as that of $Tl-2212$. Unless otherwise noted, all references to calculated modes are from these two works. We shall first discuss the modes which can be assigned by a straight-forward comparison with these works, and then address the other modes we observe.

We first note that the energy of a mode tends to decrease when the effective mass of the atoms involved in the mode increases, assuming that the force constants remain approximately the same; the size of the decrease depends on the effective mass of the atoms involved in the mode. The mass of Bi (209 amu) is close to those of

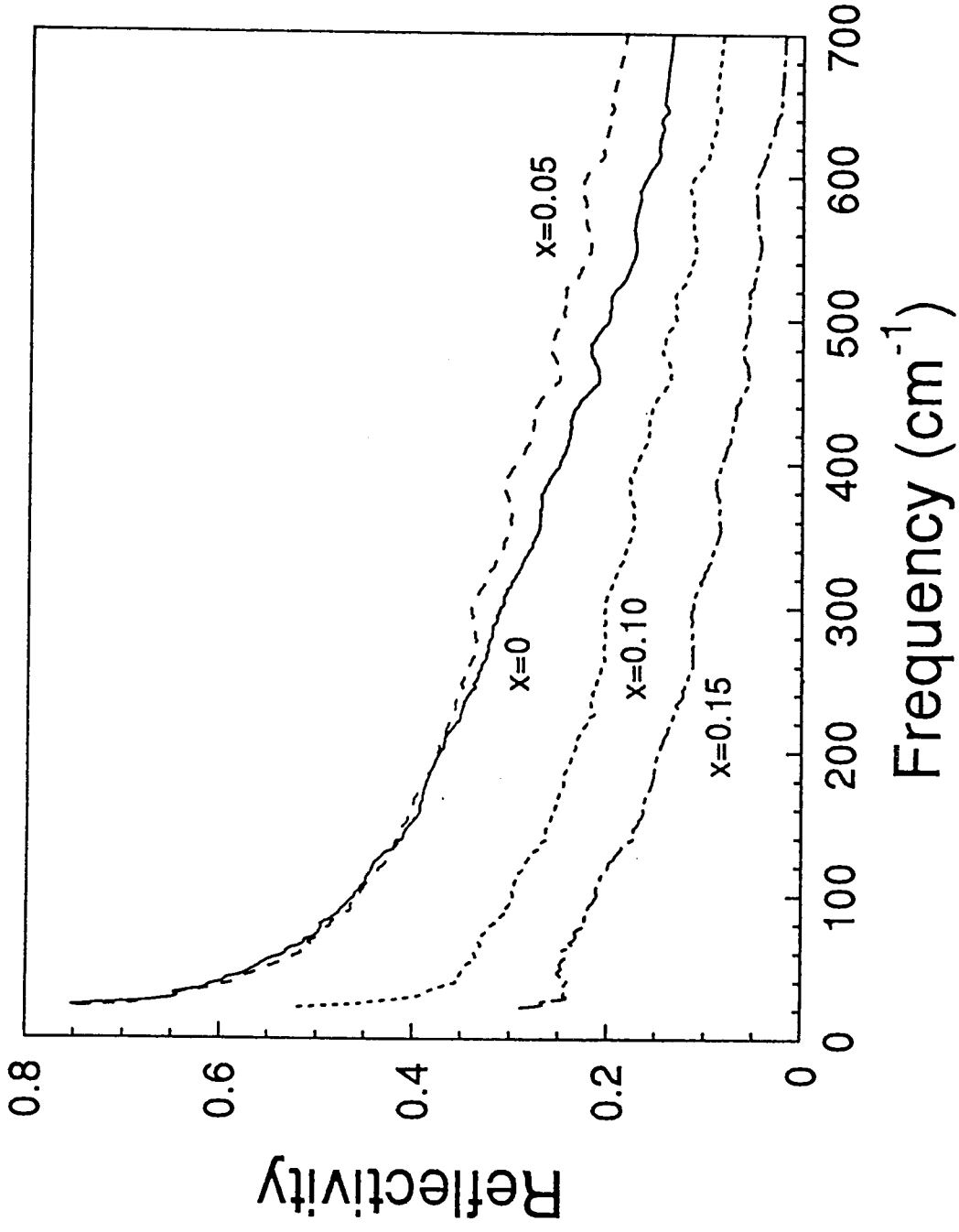

Figure 4.3: Reflectivity spectra of $Bi_{2.125-x}Pb_xSr_{1.875}CuO_{6+y}$, where x = 0, 0.05, 0.10, and 0.15, at 300 K

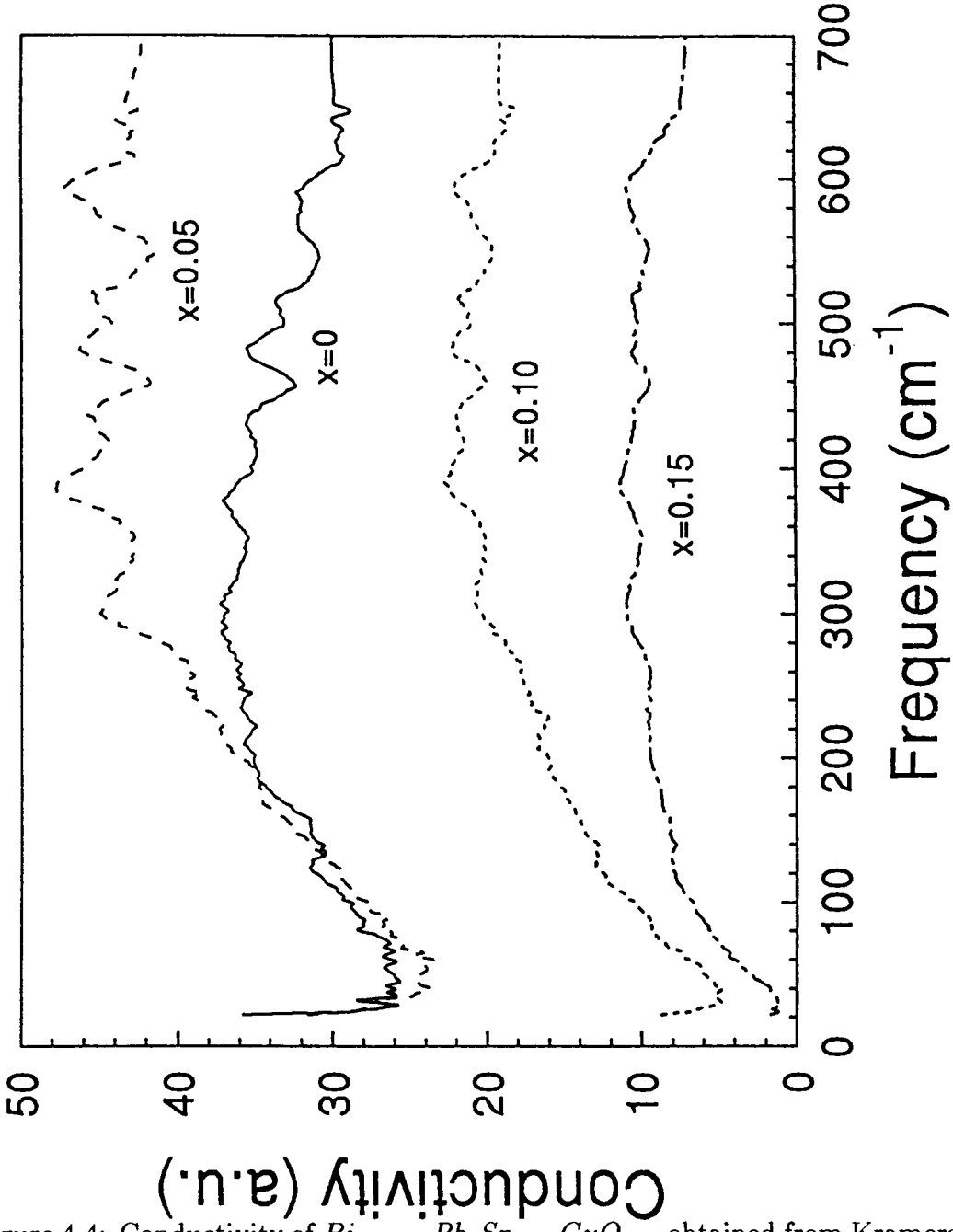

Figure 4.4: Conductivity of $Bi_{2.125-x}Pb_xSr_{1.875}CuO_{6+y}$ obtained from Kramers- Kronig analysis, at 300 K.

Table 4.1: Phonon Frequencies (cm^{-1}) Assignment $Bi_2Sr_2CuO_6 + y$

		This work	Kulkarni *et al.* [126]	Prade *et al.* [127]
		Measured	Calculated	Calculated
Symmetry	Vibration	$Bi-2201$	$Tl-2201$	$Bi-2212$
A_{2u}	Cu, Sr, Bi'	120	108	139
A_{2u}	Cu, Sr'	210	129	169
A_{2u}	$O(2)$	300	294	277
A_{2u}	$O(1)$, $O(2)'$	480	413	487
A_{2u}	$O(3)$	570	602	-
E_u	$O(1)$, $O(3)$	380	381	-
A_{1g}	$O(1)$	440	445	400
E_g	$O(3)$	515	491	493
A_{1g}	$O(3)$	600	640	517

The prime denotes a 180^0-out-of-phase-vibration. E.g., Cu, Sr, Bi' indicates that Cu and Sr vibrate in-phase and Bi vibrates out-of-phase with them.

Tl (204 amu) and Pb (207 amu). Ba (137.3 amu) is much heavier than Sr (87.6 amu). Therefore, for example, we expect that the modes involving the Sr atoms in $Bi_2Sr_2CuO_6$ will have higher frequencies than the corresponding modes in the $Tl_2Ba_2CuO_6$ system, where Ba is involved in the corresponding modes.

Because Bi is the heaviest atom in this structure, vibrations involving it are expected to have the lowest frequencies. We note however that, without knowing the exact form of the normal vibrations for each mode, one cannot predict the precise dependence on the mass of atoms involved in the vibration. However, the calculations show that only the lowest frequency mode contains the Bi atom and this mode is well separated from the others. We assign the weak mode at 120 cm^{-1} as an A_{2u} mode of Cu and Sr vibrating in-phase and Bi vibrating 180° out-of-phase with them, as in the similar modes calculated at 108 cm^{-1} in both $Tl-2201$ and $Tl-2212$ and at 139 cm^{-1} in $Bi-2212$. Note the substantial increase in the calculated frequencies with the replacement of Ba in $Tl-2212$ by the lighter Sr in $Bi-2212$, recalling again the very similar masses of Bi and Tl.

Another low frequency A_{2u} mode in $Tl-2201$ is calculated to occur at 129 cm^{-1}. The corresponding mode is at 113 cm^{-1} in $Tl-2212$ and at 169 cm^{-1} in $Bi-2212$. This mode in $Tl-2212$ is due to the out-of-phase vibrations of Cu and Ba, so we expect (in $Bi-2212$) a large increase in frequency as observed when the much lighter Sr replaces Ba. Thus our line at 210 cm^{-1} can be assigned as an A2u mode of the Cu and Sr out-of-phase vibration. Since the intensities of both of our low-frequency modes are weak and the reflectivity is high in this frequency range, these assignments must be tentative. However, it is difficult to tell if there are small frequency shifts upon the replacement of some Bi by Pb, as would be expected.

An A_{2u} mode is predicted at 294 cm^{-1} in $Tl-2201$; the corresponding mode is predicted to occur at 210 cm^{-1} in $Tl-2212$ and at 277 cm^{-1} in $Bi-2212$. Since this mode is primarily due to the vibrations of $O(2)$ atoms in the Cu-O plane, a mode at virtually the same frequency should be observed in $Bi-2201$. Therefore our 300 cm^{-1} mode can be assigned as the experimental counterpart of the 294 cm^{-1} mode in $Tl-2201$, i.e., the A_{2u} mode of $O(2)$. Similar modes are observed in all cuprate high-T_c materials.

Our mode at 480 cm^{-1} may be assigned by comparing with the A_{2u} mode calculated at 413, 487, and 457 cm^{-1} in $Tl-2201$, $Bi-2212$, and $Tl-2212$, respectively. It is due to the vibration of the $O(1)$ oxygens in $(Ba,Sr)-O$ plane and the $O(2)$ oxygens in Cu-O plane; again we observe the shift to higher frequency as Sr replaces Ba. In this mode, the $O(1)$ atoms themselves vibrate in-phase and out-of-phase with the $O(2)$ atoms. We find that the mode in the spectra is nearly unaffected by the substitution of Pb for Bi. This helps confirm that Bi is at most only weakly involved in this mode.

The broad feature centered at about 585 cm^{-1} for $x=0$ becomes clearly resolved as two modes (at 570 cm^{-1} and 600 cm^{-1}) when Pb content is increased. The higher frequency component increases in strength much more than the lower frequency component, suggesting that its optical activity is induced by breakdown of the selection rules; as noted above this may be due to deviations from tetragonal structure and/or from the introduction of impurities. We note that the highest frequency infrared- and Raman-active modes calculated for $Tl-2201$ involve primarily $O(3)$ atoms (and to a lesser degree $O(1)$ atoms) and thus should not be influenced by the replacement of Ba by Sr, but will be influenced by replacement of Tl by Bi. Comparing the highest frequency A_{2u} mode in $Tl-2212$ (at 591 cm^{-1}) with the corresponding mode

in $Bi-2212$ (at 513 cm^{-1}), we see a significant reduction in frequency. We conclude from this and similar comparisons of the Raman-active modes, that our mode at 570 cm^{-1} is most likely the counterpart of the A_{2u} mode calculated for $Tl-2201$ at 602 cm^{-1} and that at 600 cm^{-1} the A_{1g} (Raman-active) mode calculated to lie at 640 cm^{-1} in $Tl-2201$. The corresponding A_{1g} mode is calculated to occur at 517 cm^{-1} in $Bi-2212$ and at 623 cm^{-1} in $Tl-2212$.

Thus far we have assigned five of the nine observed modes to A_{2u} vibrations and one to an A_{1g} vibration. The remaining three modes may be assigned with reference to other calculated modes that would not be optically active in the ideal crystal (A_{1g} and E_g modes) or optically active modes that might be expected to be screened by the charge carriers in the a-b plane (E_u modes).

The band at 380 cm^{-1} exhibits a large increase in strength and a significant frequency increase (about 10 cm^{-1}) when Pb atoms substitute on Bi sites. The substitution-induced shift implies the involvement of Bi in the 380 cm^{-1} mode and/or sensitivity to increased orthorhombicity and disorder. Since only the lowest frequency calculated modes involve the Bi site, we conclude that it is the latter effects that are important here. An E_u mode and an E_g mode are calculated to occur in $Tl-2201$ at 380 cm^{-1} and 388 cm^{-1} respectively. The E_u mode involves motion of both the $O(1)$ and $O(3)$ oxygens and the E_g mode that of the $O(3)$ oxygen. These modes are virtually insensitive to the substitution of Ba for Sr, as evidenced by the existence of their counterparts in the 2212 compounds at very similar frequencies. We conclude that the mode at 380 cm^{-1} is likely the counterpart in $Bi-2201$ of the E_u mode at 381 cm^{-1} in $Tl-2201$.

Our mode at 440 cm^{-1} increases in strength upon Pb substitution. Again, we

consider the main effect of substitution to be increased disorder which activates modes that are not optically active in the ideal crystal. We assign this mode to the A_{1g} mode calculated to occur at 445 cm^{-1} in $Tl-2201$. It is due to motion of the $O(1)$ oxygens and has counterparts at 439 cm^{-1} in $Tl-2212$ and at 400 cm^{-1} in $Bi-2212$.

Finally, we consider our mode at 515 cm^{-1}. It is likely the counterpart of the E_g mode calculated to occur at 491 cm^{-1} in $Tl-2201$ and at 493 cm^{-1} in both $Bi-2212$ and $Tl-2212$. This mode involves motion of the $O(3)$ oxygens. Comparing the behavior of the two lines at 480 cm^{-1} and 515 cm^{-1}, one finds that the strength of the line at 515 cm^{-1} increases more rapidly with Pb substitution. This supports the assignment of the 480 cm^{-1} mode as an (allowed) A_{2u} mode and the 515 cm^{-1} mode as a (forbidden) E_g mode.

4.5 Application of Shell Model

The above discussion is based on the analogy with previous shell-model calculations on $Tl-2201$ and $Bi-2212$ [126] [127]. It is desirable to make a more direct comparison with calculated phonon modes of $Bi_2Sr_2CuO_6$. However, at present, shell model parameters for this crystal are not available. A preliminary shell-model calculation is carried out here based on a reasonable estimate of shell-model parameters for other high T_c compounds. (More detailed description of the shell-model equations can be found in Appendix and Ref. [157].) The parameters used here listed in Table 4.2, provided by Dr. de Wette [128]. Our calculated results are only semi-quantitative since it is well known that shell-model parameters are not completely transferable. Nevertheless, it is useful to study the trend of the changes of vibrational frequencies by modifying the shell-model parameters mimicking the change of chemical environment

due to, for example, lead doping. However, it is not possible to simulate uniquely the changes caused by the induced crystal structural change upon doping.

In a simple shell model which takes into account the electronic polarizability in the dipole approximation, each ion is represented as a core of charge X surrounded by a rigid spherical shell of charge Z_{sh}; the ionic charge is $Z_{ion} = X + Z_{sh}$, and the core and shell are connected by a spring k expressed in units $e^2/\mathring{A}^3$. The interaction potential in this model is divided into two basic parts: a long-range Coulumb part (including the dipole interactions) for which the potential is exactly known and short-range overlap parts which, for closed-shell ions, can be rather well described by Born-Mayer potentials

$$V_{ij}^{ss} = a_{ij} exp(-b_{ij}). \tag{4.1}$$

We take into account shell-shell short-range forces between Bi(Pb) and O, Sr and O, Cu and O, and between neighboring oxygen ions in the $Bi_2Sr_2CuO_6$ system with the body-centered pseudo-tetragonal unit cell.

Table 4.3 lists calculated phonon frequencies of $Bi_2Sr_2CuO_6$ at several variation of the shell-model parameters provided by Dr. de Wette [128]. Since the masses of Bi (209 amu) and Pb (207 amu) are close to each other, simply changing the mass of Bi into that of Pb does not lead to any changes greater than 1 cm^{-1} in the vibrational frequencies. On the other hand, there are noticeable changes caused by the change of either the total ionic charge of Bi or the core-shell spring constant. The change of the ionic charge corresponds to the change of valence. And the change of spring constant corresponds to the change of atomic polarizability, because the numbers of their valence electrons are different. Substitution of Bi by Pb , should correspond to decreases of both the atomic valence and the polarizability. As shown in Table

Table 4.2: Shell Model Parameters [128] of $Bi_2Sr_2CuO_6 + y$. Z_{ion} is the ionic charge; Z_{sh} is the shell charge, k is the core-shell spring constant; a_{ij} and b_{ij} are the Born-Mayer constants.

Ion	Z_{ion} (e)	Z_{sh} (e)	k $(e^2/\mathring{A}^3)$	
Bi	2.5	2.42	5.04862	
Sr	2.35	2.32	0.95433	
Cu	2.00	3.22	5.76022	
O_1	-1.98333	-2.70	9.59211	(in plane)
			1.45509	($\perp$)
O_2	-1.98333	-2.70	1.45509	
O_3	-1.98333	-2.70	9.59211	

	a_{ij} (eV)	b_{ij} $(\mathring{A}^{-1})$
$Bi-O$	3015	3.0
$Sr-O$	3010	2.9
$Cu-O$	1259	3.5
$O-O$	1000	3.0

4.3, both of these decreases lead to the overall decrease of phonon frequencies. This may at first sight appear to contradict to our experimental observation, in which we have noticed an significant increase of the E_u mode at 380 cm^{-1}. However, it is pointed out earlier that the increase of this E_u mode is most likely due to the crystal structural changes caused by the lead doping. Further refined shell-model parameters are greatly desired for the $Bi_2Sr_2CuO_6$ crystal. Our experimental data can provide valuable checks for these refinements.

In addition, there may exist a variety of complications in the ionic interactions in high T_c superconducting compounds including the $Bi_2Sr_2CuO_6$ system, such as non-central contributions (many-body forces), hybridization of electronic states (charge transfer), anharmonicities, etc., which are not contained in our calculation. The effects of such interations might possibly be exhibited by inelastic neutron scattering measurements of the phonon dispersion curves over the entire Brillouin zone. Such additional information will probably call for further adjustments in the short-range potential parameters. Therefore, in the absence of more complete information, it is not useful to attempt to match the available experimental results too closely. For a tentative comparison to the calculated results, we show the experimental modes from our spectra in Table 4.3.

4.6 Doping effects on overall spectra

Generally, the intensity of the background reflectivity is determined both by the number of the impurity ions and their locations in lattice, which in turn influence the scattering rate, and by the concentration of charge carriers. The presence of carriers increases the overall background reflectivity and that of impurities decreases it. The

Table 4.3: Calculated phonon frequencies (cm^{-1}) based on the shell-model parameters of Table 5.2 (first column). The second to the fifth columns are the results with different Z_{ion} and k of the Bi ions.

Exp. data[a)]	$Z_{ion}(Bi) = 2.6$	$Z_{ion}(Bi) = 2.5$	$Z_{ion}(Bi) = 2.7$	$k(Bi) = 0.8k_0^{b)}$	$k(Bi) = 1.2k_0^{b)}$	Symm.	Mode
120	145	147	139	142	145	A_{2u}	Bi, Sr, $O(2)$
-	281	270	264	272	274	E_u	Cu, $O(1)$, $O(3)$
300	295	292	287	287	292	A_{2u}	(Bi, Sr) Cu, $O(2)$, $O(3)$
-	333	322	332	329	331	E_u	Sr, Cu, $O(1)$
-	380	378	383	380	381	E_u	$O(1)$, $O(2)$
380	382	381	385	382	383	E_u	$O(1)$, $O(3)$
480	392	392	400	397	400	A_{2u}	$O(2)$, $O(3)$
570	497	499	500	498	501	A_{2u}	$O(1)$, $O(3)$
-	523	499	520	518	518	E_u	Cu, $O(2)$
-	525	528	524	535	531	E_u	Cu, $O(2)$

[a)] Modes from our experimental data.

[b)] $k_0(Bi) = 5.04862$, the core-shell spring constant of Bi when $Z_{ion}(Bi) = 2.6$, see Table 4.2.

substitution of Pb for Bi will increase the concentration of the free carriers in this system, but it will also increase the scattering rate.

The overall level of our reflectivity changes dramatically and in an unusual fashion as x increases. As shown in Fig. 4.3, as lead is doped in with $x = 0.05$, the reflectivity dramatically increases over that of non-doped sample. For higher values of x, the reflectivity decreases and the sample appears more insulating. The change in conductivity of these compounds with variation in lead content is consistent with the reflectivity shown in Fig. 4.4. The observed change could be due to subtle changes in the structural modulations of the pseudo-tetragonal phase as Pb is added followed by a metal-insulator transition when the structure becomes orthorhombic. The anomalous behavior of the $x = 0.05$ sample indicates a critical Pb-doping concentration near the change of the structure from pseudo-tetragonal to orthorhombic. According to Tarascon et al [123], the structural modulation is due to the insertion of extra oxygen in the Bi-O layer, and replacing a Bi by a Pb in the 2201 Bi-layered compound affects the modulation through the removal of oxygen to compensate for the charge imbalance created by the substitution.

A recent report of far infrared transmission measurements on single crystal samples of $Bi_2Sr_2CaCuO_8$ shows a strong evidence that the superconductivity in $Bi_2Sr_2CaCuO_8$ is gapless [117]. This result also rules out "clean limit" explanations for the absence of the spectroscopic gap in the material by comparing the results of the infrared measurements on "pure" samples and with those on "dirty" samples produced by electron-beam irradiation. This result is consistent with a recent reflectivity study on Ni-doped $YBa_2Cu_3O_{7-\delta}$ films [94]. Since $Bi_2Sr_2CuO_{6+y}$ shares similar structural elements with $YBa_2Cu_3O_{7-\delta}$, and $Bi_2Sr_2CaCuO_{6+y}$ in that the crystal structure is body-centered tetragonal unit cell, one may speculate that super-

conducting spectroscopic gaplessness could be a common property in the $Bi-2201$ as well. It would be interesting to see the result from infrared measurement on single crystals of $Bi_2Sr_2CuO_{6+y}$.

4.7 Conclusions

We have studied the far-infrared reflectivity spectra and conductivities, obtained from Kramers-Kronig analysis, of $Bi_{2.125-x}Pb_xSr_{1.875}CuO_{6+y}$ system. Phonon modes have been tentatively assigned by comparing with theoretical work on similar compounds. The phonon at 380 cm^{-1} is observed to shift to higher frequency upon the partial substitution of Bi by Pb. Our results are in reasonable agreement with theoretical calculations. However, definitive analyses await theoretical calculations for this compound as cautioned by the authors in Ref. [12] that the mode frequencies are very sensitive to the particular parameters of each system. We have also applied a direct calculation of the wave vector and frequency dependent lattice vibrational tensor of $Bi_2Sr_2CuO_{6+y}$ based on the shell model. We have performed the fitting process on the shell model parameters in order to investigate the doping effects on phonon frequencies and lattice vibration. We find that not only the mass of ions in a lattice but also its total ionic charge as well as the core-shell spring constant can cause a great deal of variation in the phonon frequencies. Further refined shell-model parameters are greatly desired for the $Bi_2Sr_2CuO_6$ crystal. Our experimental data can provide valuable checks for these refinements.

Chapter 5

Far-Infrared Response of Superconductors $(Nd_{1-x}M_x)_2CuO_{4+\delta}$

5.1 Introduction

The discovery of the new copper oxide superconductor of composition $M_{2-x}R_xCuO_{4-y}$ (M=Pr, Nd, and Sm; R=Ce and Th), by Tokura et al. [15] [134] [135] has attracted great attention since transport measurements indicate that the charge carriers in these materials are likely dominated by electrons rather than holes, as found in all previously discovered high temperature superconductors.

For all Ce (Th) concentrations possible ($0 \leq x \leq 0.2$), substituting the trivalent lanthanide in the insulator Ln_2CuO_4 with a tetravalent lanthanide makes the system become a superconductor. Increasing x in $M_{2-x}R_xCuO_{4-y}$ ($M = Ce$ or Th), apparently introduces more electrons into CuO_2 planes, producing a continuous insulator-metal transition and yielding superconductivity with a maximum $T_c = 25K$ and maximum flux expulsion at $x = 0.15$ and $y = 0.02$ [137].

This so-called n-type superconductor is the only member of the high T_c copper

oxides found so far with electron type conduction. The physical properties [130] of the material are significantly different from those hole-type systems. For instance, its dc resistivity exhibits a T^2-like temperature dependence rather than the more common linear behavior; secondly, both a negative and positive Hall coefficient R_H have been reported [131] [132] in this electron doped superconductor and R_H decreases in magnitude with increasing Ce (Th) content x. In contrast, the Hall coefficients for other cuprate superconductors are all positive; finally, the superconducting coherence lengths, from the measurements of the upper field H_{c2} as a function of temperature, are about 70 Å within CuO_2 planes and 3.4 Å along the c axis. For hole type superconductors, for example the YBCO compound, these lengths are around 12-16 Å in CuO_2 planes and 2-3 Å along the c axis [47].

It is not clear whether the interaction leading to superconductivity is the same as in the n-type material in other cuprate systems such as $YBa_2Cu_3O_7$. We note that $T_c = 24K$ is certainly within reach of the prediction by the conventional strong-coupling theory; thin films of Nb_3Ge have a transition temperature at $23K$. The n-type material provides an opportunity to assess the effects of the nature of the charge carrier on the mechanism of superconductivity. Recently this system has attracted much more interest because of its possible simple BCS s-wave pairing in the superconducting state [131], which is in contrast to d-wave behavior proposed for hole doped high-T_c cuprates [133].

Far-infrared spectroscopy can be a powerful tool in the study of the properties of superconductors [32]. In this chapter, we study the superconducting $Nd_{2-x}Ce(Th)_xCuO_{4-y}$ system for x around 0.15 with electrons as charge carriers. Its parent compound, $Nd_2Ce_2CuO_4$ is an insulator with ionic properties. Since the free-carrier density created by Ce or Th doping is low and the screening of

internal electric fields is weak, it is expected that ionic characteristics associated with $Nd_2Ce_2CuO_4$ will be preserved in $Nd_{1.85}Ce(Th)_{0.15}CuO_{4-y}$. This partially screened ionic nature plays an important role in the electron-phonon interaction inside $Nd_{1.85}Ce(Th)_{0.15}CuO_{4-y}$.

The interpretation of optical properties of hole-type copper oxide superconductors is still unclear due to both the complicated structure of these materials and the lack of a definitive theory [129] [18]. The study based on the n-type superconductor will certainly enrich our knowledge of the high T_c copper oxide materials.

We will present far-infrared spectra of $Nd_{1.85}R_{0.15}CuO_{4-y}$ (R=Ce and Th) measured in the superconducting and normal states over the frequency range $20 - 10000\ cm^{-1}$ and interpret the results in terms of lattice vibrations, free-carrier effects, and possibility of a superconducting energy gap in the range predicted by BCS theory.

5.2 Preparation and Characterization of $Nd_{1.85}R_{0.15}CuO_{4-y}$

All of the electron-doped $Nd-214$ superconductors with the oxygen deficiency were achieved by annealing in reduced atmosphere. The preparation of single phase materials for these compounds is very delicate as compared with hole-doped high-T_c copper oxides. The n-type samples which were measured in our experiments were prepared and characterized by Dr. Peng in University of California at Davis, where results cited below were published in Ref. [42].

Samples were prepared by solid-state reaction from high-purity (99.99%) Nd_2O_3, CeO_2 or ThO_2, and CuO by the method described in detail previously [42]. Resultant

powders were pressed into pellets which were then annealed and cooled to room temperature. Sample surfaces were mechanically polished to a mirrorlike finish.

X-ray diffraction measurements on $Nd_{1.85}R_{0.15}CuO_{4-y}$ ($R = Ce$ and Th) indicated that all samples were composed of single-phase, tetragonal material with lattice constant of $a = 0.3959 \pm 0.0004\ nm$ and $c = 1.211 \pm 0.002\ nm$ for the Ce compound and $a = 0.3955 \pm 0.0004\ nm$ and $c = 1.2116 \pm 0.0006\ nm$ for the Th compound.

The dc magnetic susceptibility measurements, which were made in a variety of magnetic fields using a Quantum Design SQUID magnetometer, are displayed in Fig. 5.1.a and Fig. 5.1.b. The magnetic field used in the field-cooled magnetization (Meissner effect) versus temperature for the $Nd_{1.85}Ce_{0.15}CuO_{4-y}$ is 5 Oe, for the $Nd_{1.85}Th_{0.15}CuO_{4-y}$ is 10 Oe. Measurements of the dc magnetic susceptibility showed that the Meissner effect below 20 K is approximately 20% that expected for full diamagnetism, indicating that superconductivity is a bulk property of the sample. Onset of the magnetic transition is at 26 K in the Ce sample and at 22 K in the Th sample; the $10\% - 90\%$ width is about 4 K (Ce) and 5 K (Th).

The dc electric resistivity $\rho(T)$ measurements [42] were performed on rectangular specimens cut from sintered pellets employing the standard dc four-probe technique. To ensure good contacts between the electrical leads and the samples, four silver contacts were evaporated on the sample surface, followed by annealing at 400 $^{\circ}C$ in a N_2 atmosphere for two hours to help the silver diffuse easily around the contacts on the sample surface. This process reduces the contact resistance dramatically. After this process, platinum wires were attached to the silver contacts using silver paint. In a zero magnetic field the midpoint of the resistive transition is at 23 ± 1 K (Ce) and the $10\% - 90\%$ width is about 5 K; for the Th sample, the corresponding values are

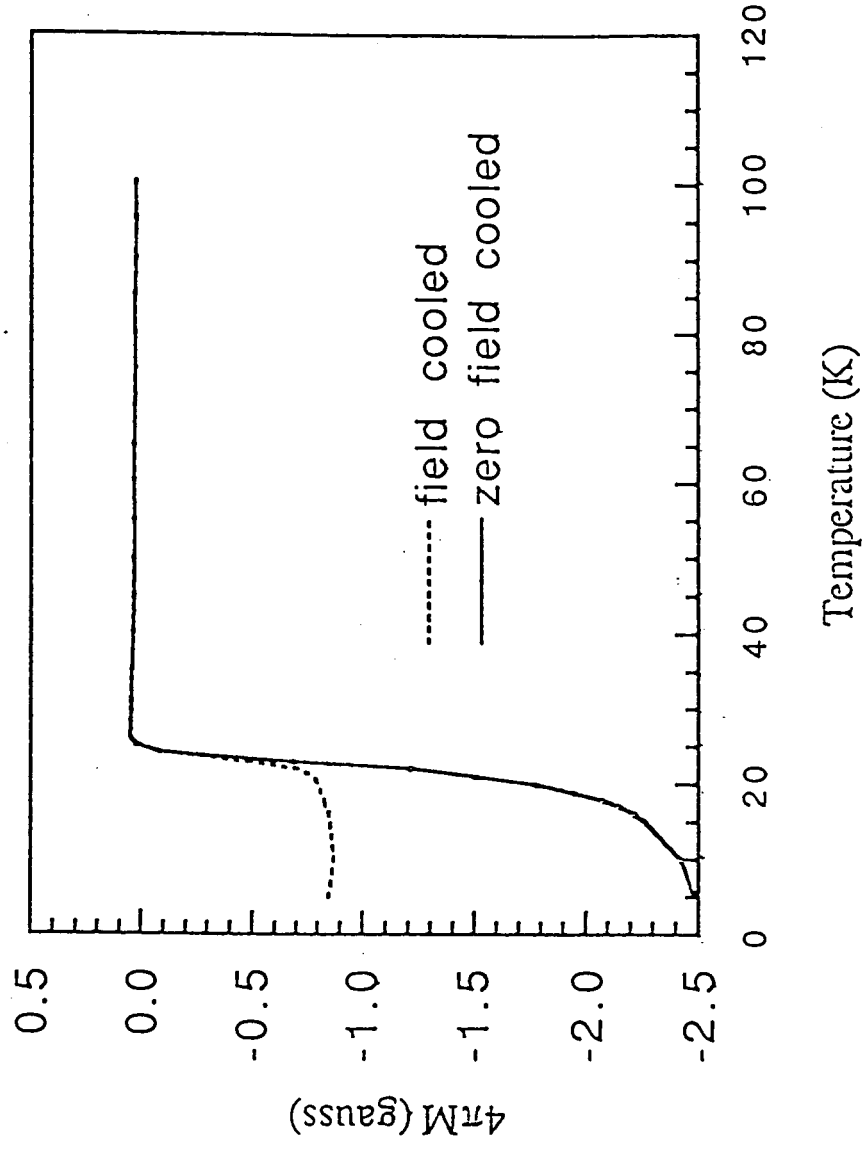

Figure 5.1.a: The dc magnetic susceptibility of $Nd_{1.85}Ce_{0.15}CuO_{4-y}$ (Ref. [42]).

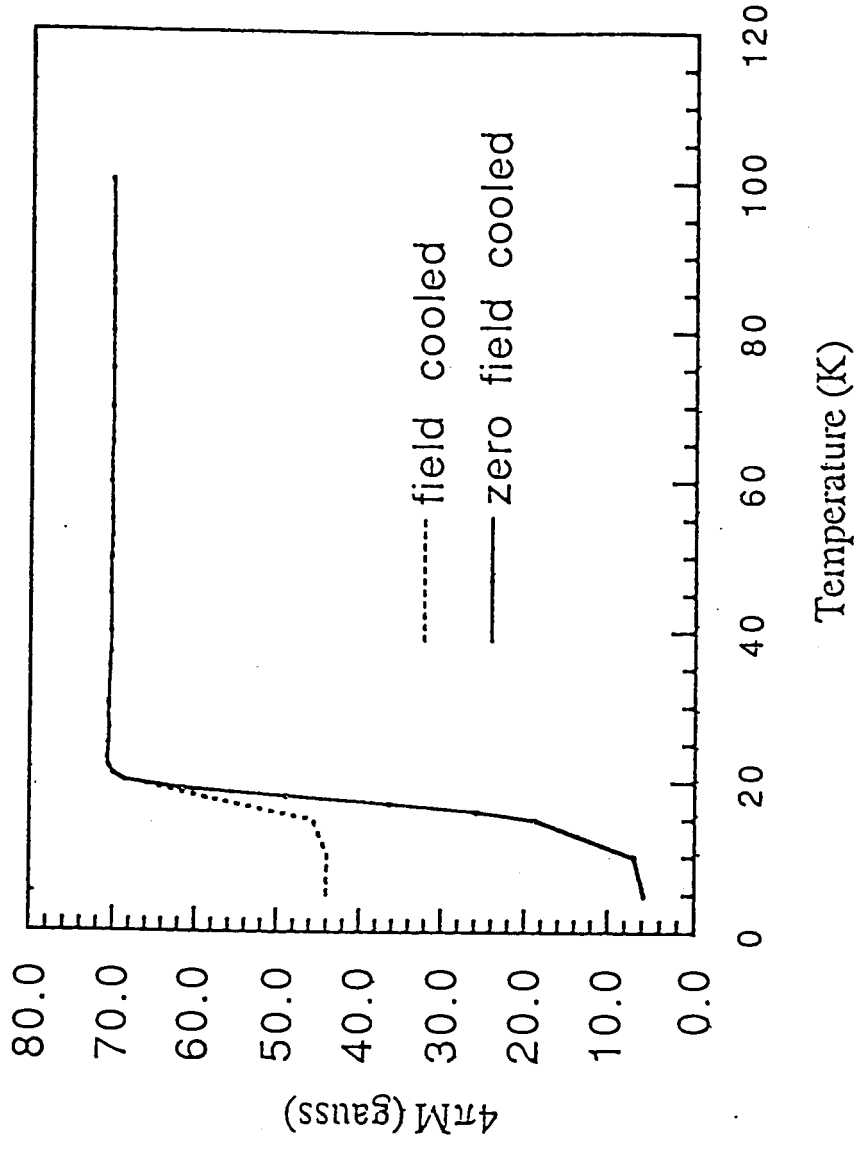

Figure 5.1.b: The dc magnetic susceptibility of $Nd_{1.85}Th_{0.15}CuO_{4-y}$ (Ref. [42]).

18.5 ± 1 K and 3 K. Zero resistance is reached at about 17.5 K and 15 K, respectively. We take the midpoint of the resistive transition as T_c. Normal-state resistivity just above the transition (Ce) is 27 $m\Omega$ cm and at room temperature 9 $m\Omega$ cm; for the Th sample the corresponding values are 7.6 and 2 $m\Omega$ cm.

The 2-1-4 Nd_2CuO_4 compounds with Nd-site cations smaller than lanthanum adopt a tetragonal structure similar to, but topologically distinct from, K_2NiF_4 (Ref.[122]). The crystal structure is commonly referred as to the tetragonal form with symmetry of $I_{4/mmm} = D_{4h}^{17}$. The unit cell has square-plane coordinated copper in Cu-O1 planes, with large cations (Nd, Ce, Sr) above and below. The O2 planes are in the between of two Nd layers, as shown in Fig. 5.2.

5.3 Infrared Reflectance of $Nd_{1.85}Ce(Th)_{0.15}CuO_{4-y}$

Infrared reflectance spectra were measured at a near-normal angle of incidence for the samples on a Bruker IFS 113V Fourier transform interferometer in conjunction with a He-cooled bolometer for the far-infrared range and a pyroelectric detector for higher frequencies. The resolution of the reflectance was 2 cm^{-1}. The temperature of the samples was varied above and below the T_c for measurements in the frequency range of $\approx$ 20 to 1000 cm^{-1}; room-temperature reflectance spectra were also taken from 100 to 10000 cm^{-1} for the two samples. Reference spectra were taken on a polished stainless-steel mirror (for details, see Chapter 2). The measurements were done with the participation of B. P. Clayman and S. H. Wang and the author [119].

Figs. 5.3.a and 5.3.b present the spectra of $Nd_{1.85}Ce_{0.15}CuO_{4-y}$ and $Nd_{1.85}Th_{0.15}CuO_{4-y}$ in normal and superconducting states fron 20 to 1000 cm^{-1}. The inset of Figs. 5.3.a and 5.3.b gives the room-temperature reflectance of the two

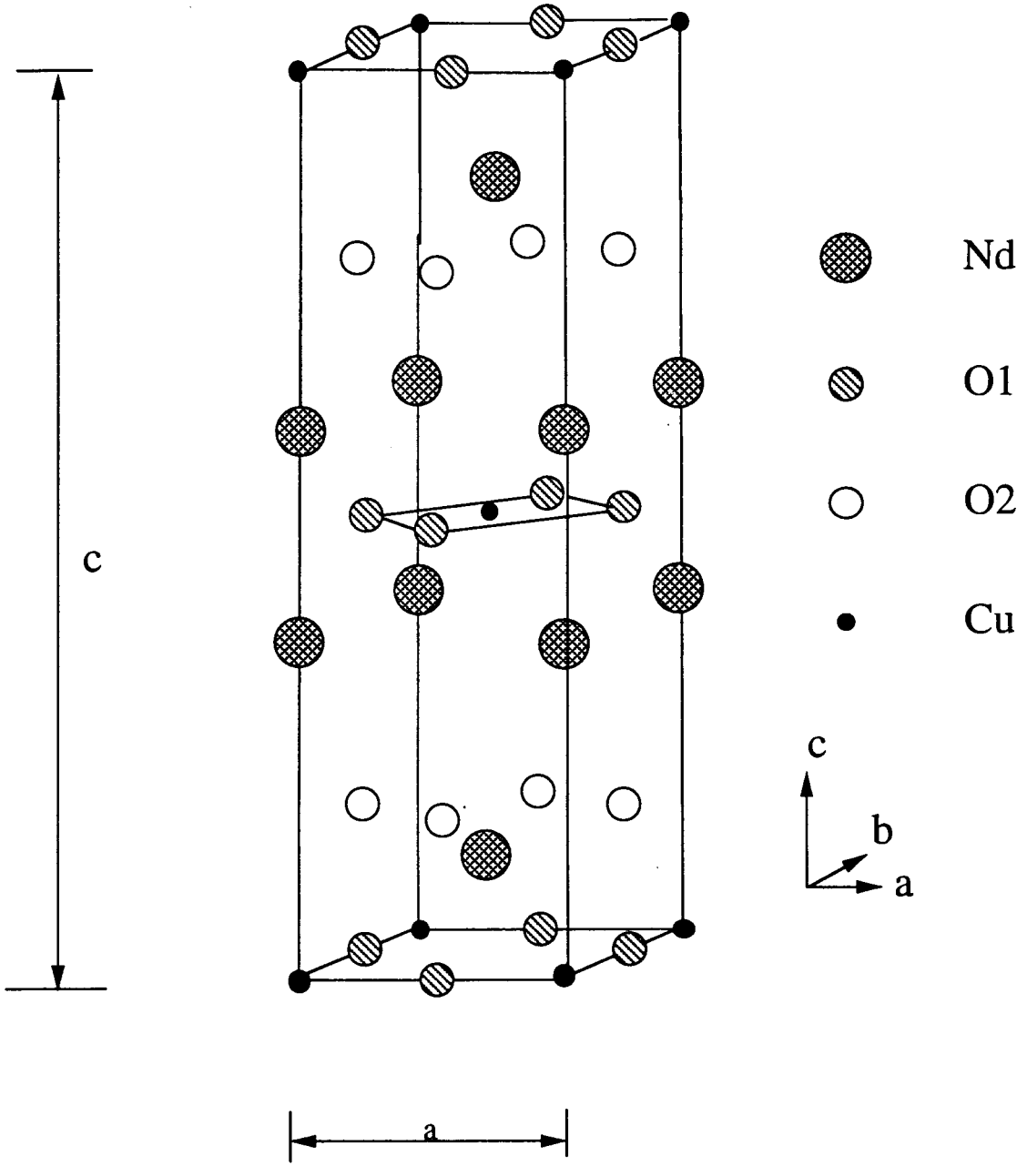

Figure 5.2: Nd_2CuO_4 unit cell

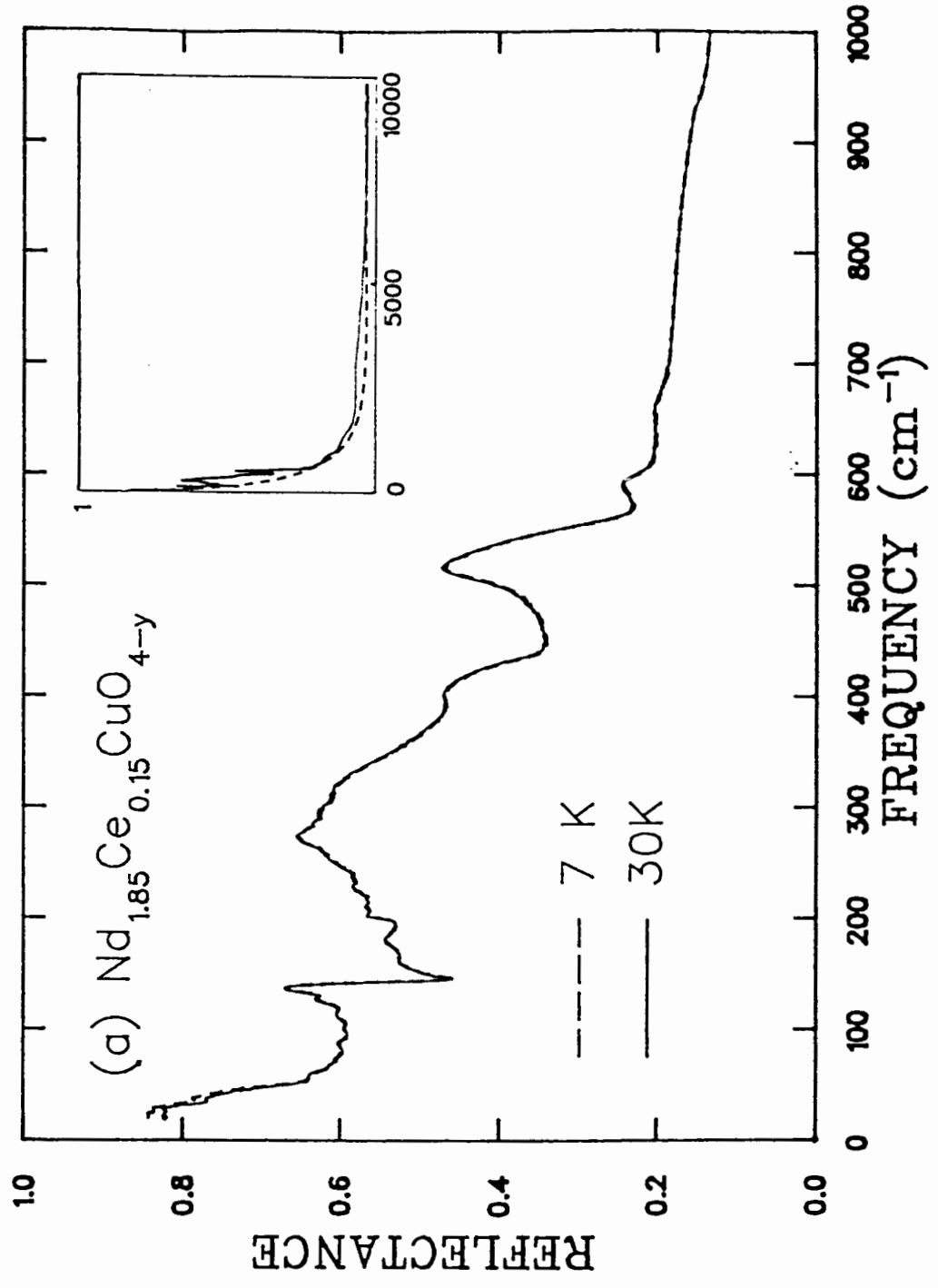

Figure 5.3.a: Reflectance spectra of $Nd_{1.85}Ce_{0.15}CuO_{4-y}$

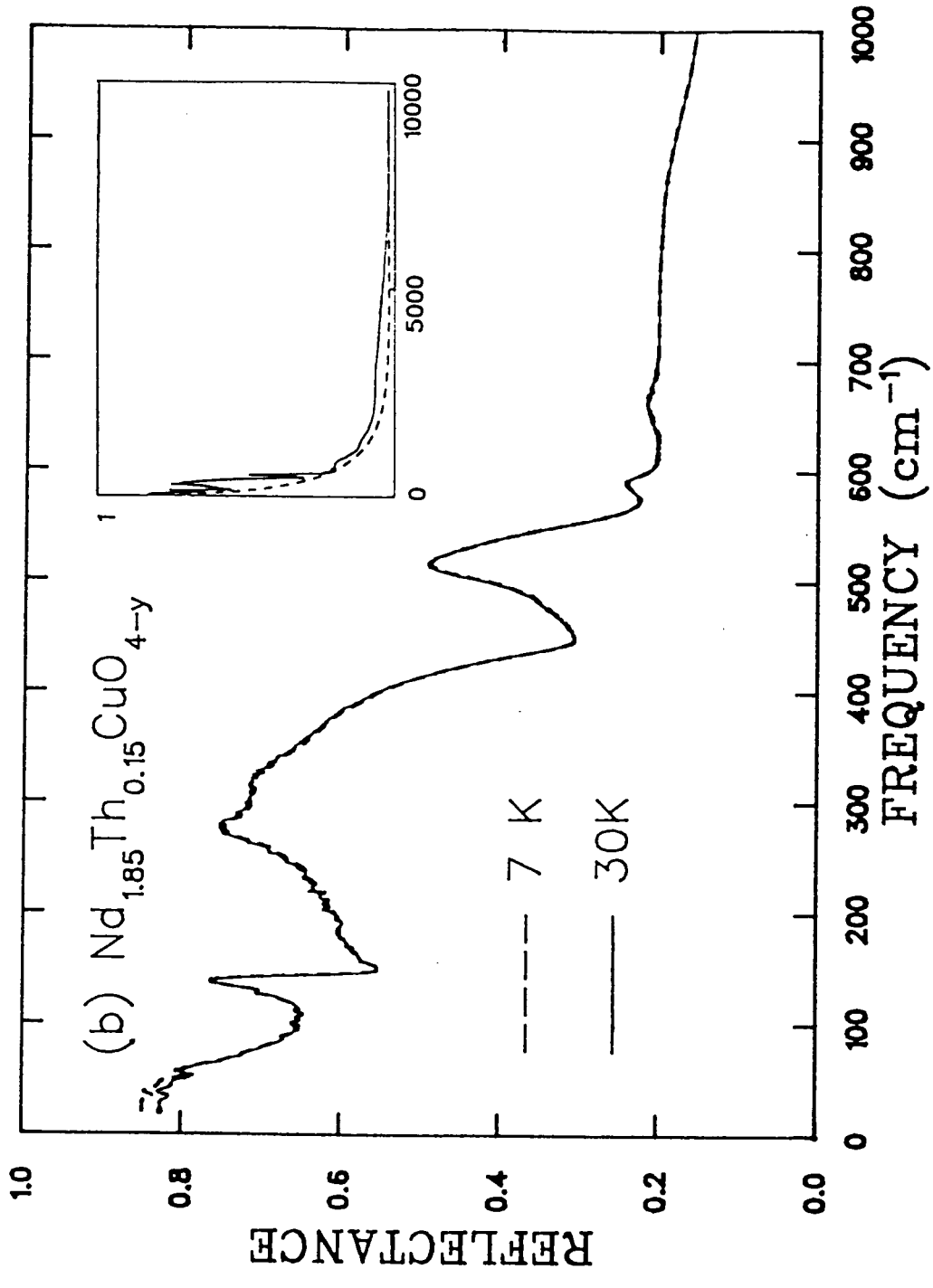

Figure 5.3.b: Reflectance spectra of $Nd_{1.85}Th_{0.15}CuO_{4-y}$

compounds from 100 to 10000 cm^{-1}. The spctra of the two compounds are very similar, except that reflectance of $Nd_{1.85}Ce_{0.15}CuO_{4-y}$ shows a significant increase in the strength of the feature at $\approx$ 410 cm^{-1} and a $\approx$ 10% reduction of the overall reflectance by comparing with the Th-compound.

Figs. 5.4.a and 5.4.b give the reflectance ratios in the frequency range of 20 to 70 cm^{-1}, including one additional intermediate temperature. Above about 100 cm^{-1}, there are no significant differences between reflectivities in the normal and superconducting states. A distinct enhancement of reflectance occurs in the superconducting state with a plateau begin at about 50 cm^{-1}. Above 10 K, the plateau height decreases and the region of decreased reflectance above 60 cm^{-1} gradually disappears; the plateau loses its distinct edge, preventing precise determination of the temperature dependence of the edge (shown below likely to be associated with the gap energy), but we note that the frequency at which the curves cross 1.00 decreases with increased temperature.

Figs. 5.5.a and 5.5.b present the real part of frequency-dependent conductivity calculated by a Kramers-Kronig transformation of the data in Figs. 5.3.a and 5.3.b. Because reflectance data are not available below 20 cm^{-1} and above 10,000 cm^{-1} due to instrumental restrictions, extrapolations of the reflectance are necessary. Calculated conductivities are somewhat dependent on the nature of the extrapolation, although the locations and relative strengths of the features are not.

One of the major problems in interpreting the optical experimental results for polycrystalline high-T_c materials is from the random orientations of the crystal grains in the sample. By analogy with the early work on La-214, our analyses on the experimental results must take into account the well-known anisotropy of these materials.

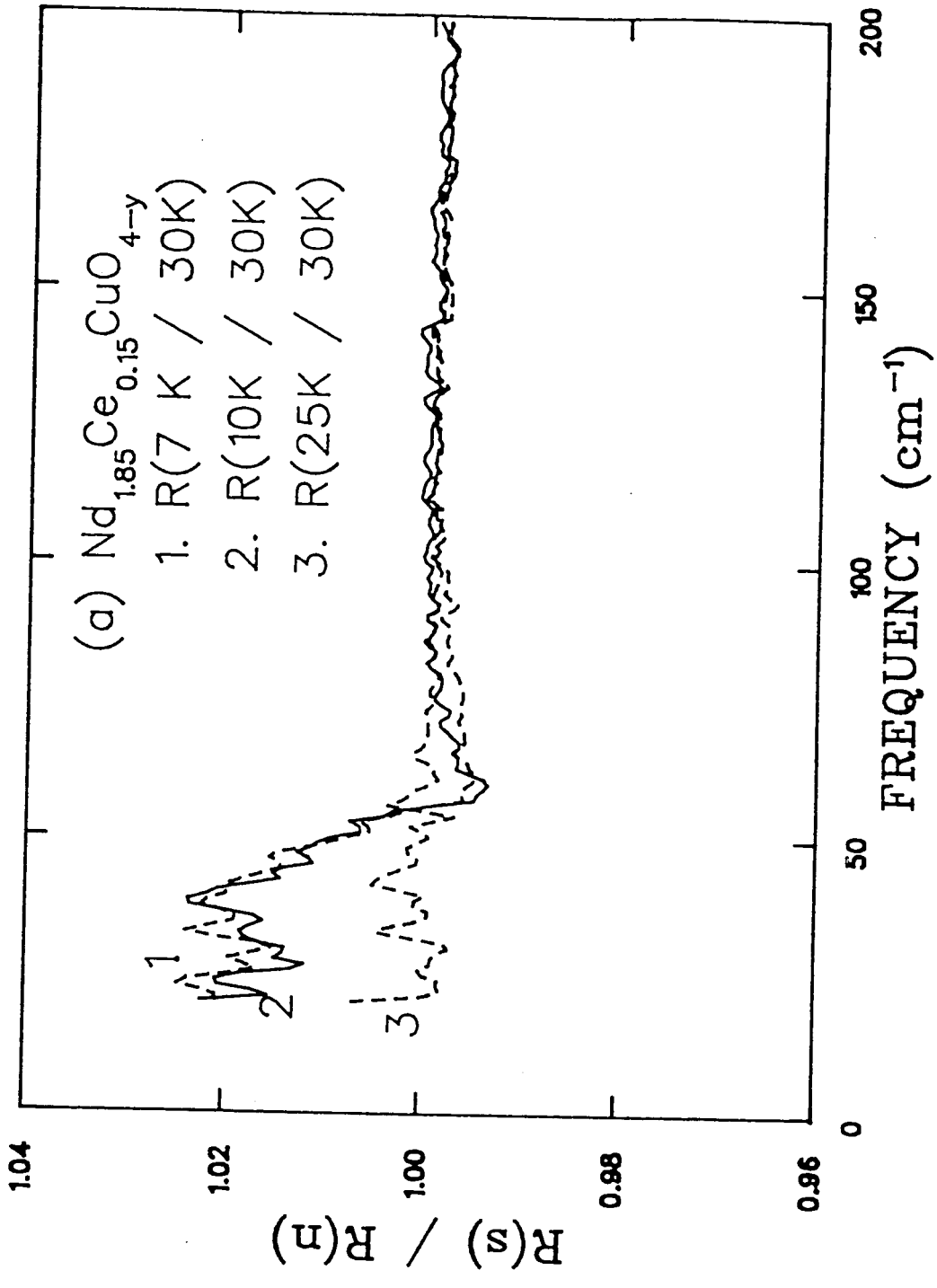

Figure 5.4.a: Reflectance Ratios of $Nd_{1.85}Ce_{0.15}CuO_{4-y}$

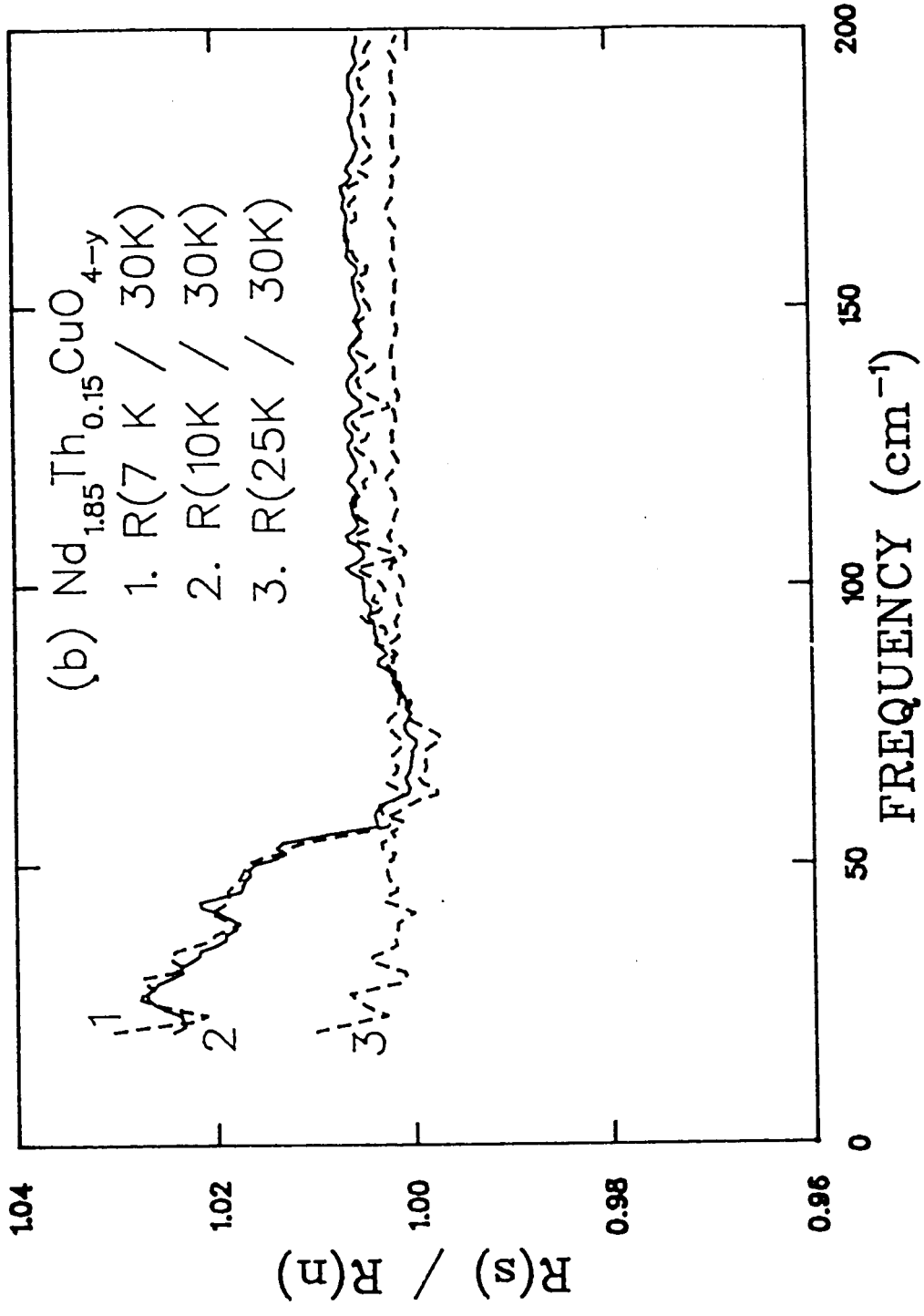

Figure 5.4.b: Reflectance Ratios of $Nd_{1.85}Th_{0.15}CuO_{4-y}$

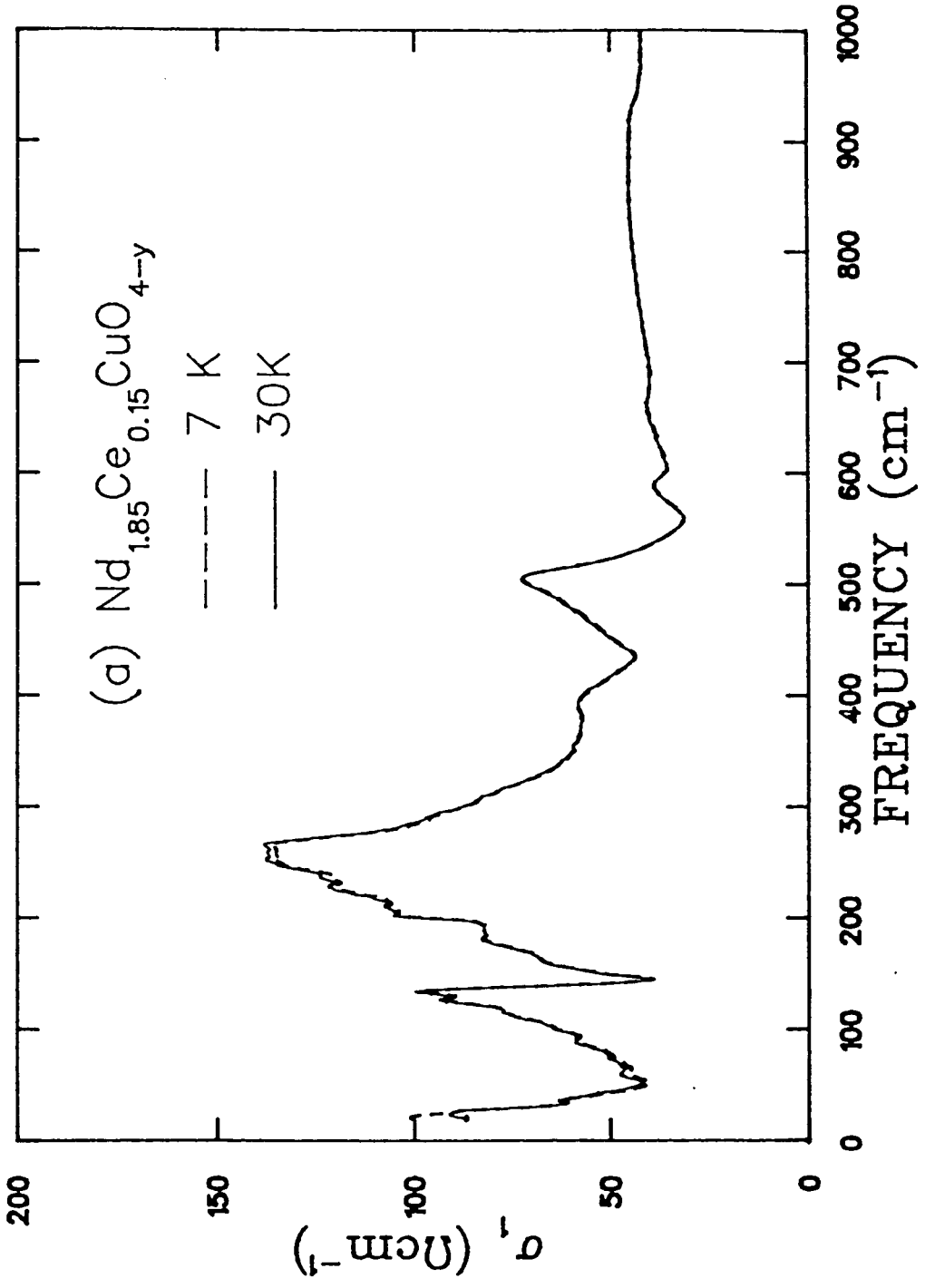

Figure 5.5.a: Conductivity of $Nd_{1.85}Ce_{0.15}CuO_{4-y}$

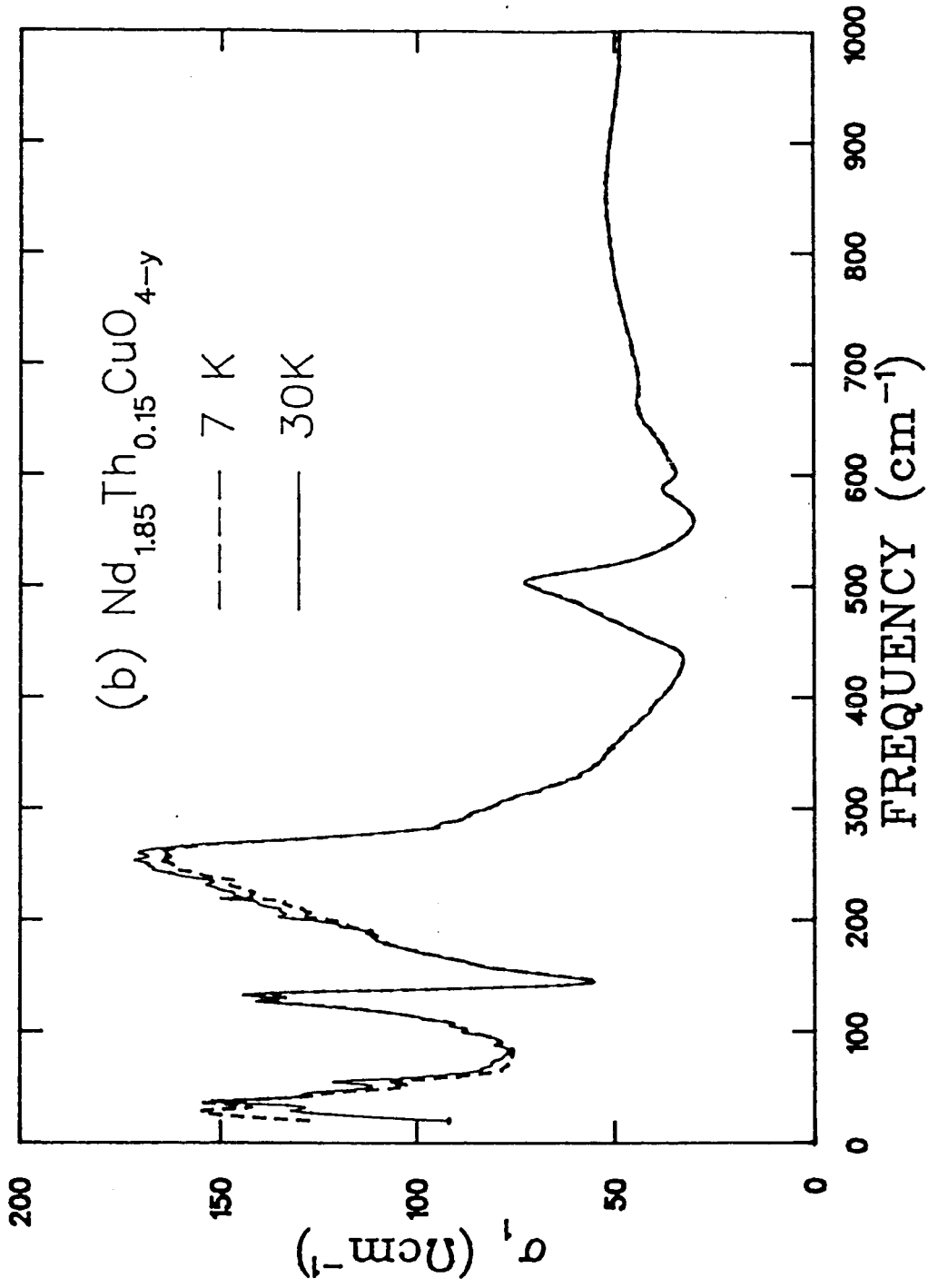

Figure 5.5.b: Conductivity of $Nd_{1.85}Th_{0.15}CuO_{4-y}$

Similar to works in [139, 140] on $La_{2-x}Sr_xCuO_4$, we consider our reflectance as a composite of the contributions from a metallic ab-plane and a nearly insulating c axis. Excitations in the ab-plane will be highly screened but those along the c axis will not be. The actual superposition of the contributions from the two directions will depend on the size, shape, the orientation of the crystallites and the wavelength of the incident radiation, and the incident wavelength λ is usually much smaller than the characteristic dimensions (about 10 μm) of the crystallites. A simple superposition of the reflectivities [139],

$$R = (1-f)R_{ab} + fR_c\,, \tag{5.1}$$

may suffice if the wavelength is much smaller than the characteristic dimensions of the crystallities. In Eq. (5.1) $R_{a-b(c)}$ is the reflectance for E directed along ab-plane or c-axis and f is the volume fraction of the R_c component.

The hole-doped high T_c compound, $La_{1.85}Sr_{0.15}CuO_{4-y}$, has a crystal structure and chemical composition similar to the electron-doped system. Comparing our reflectance spectra in Fig. 5.3.a and Fig. 5.3.b with those of $La_{1.85}Sr_{0.15}CuO_{4-y}$ [17], we find that the La-214 system shows qualitative similarity with ours. Its reflectance approaches about 80% at low frequency range and 20% at higher than 700 cm^{-1}. This seems to be the common optical behavior of both types of the "214" materials. Based on these similarities of stoichiometry, crystal structure, chemical composition and infrared properties, we believe that the anisotropic model should also work for the n-type $Nd_{1.85}Ce(Th)_{0.15}CuO_{4-y}$ compounds. These previous anisotropic studies on the polycrystalline $La_{1.85}Sr_{0.15}CuO_{4-y}$ could put us in a better position to understand our experimental results on $Nd_{1.85}Ce(Th)_{0.15}CuO_{4-y}$. We can therefore expect that our R_{ab} and R_c of superconducting $Nd_{1.85}Ce(Th)_{0.15}CuO_{4-y}$ present similar doping

effects on the spectra on $La_{1.85}Sr_{0.15}CuO_{4-y}$ by Collins et al. [18], that is, Sr on La site of insulator La_2CuO_4 or $Ce(Th)$ on Nd site of Nd_2CuO_4 affects the electric properties only on Cu_2O planes. Thus, by comparing our experimental spectra of the superconducting $Nd-214$ with relevant works from other groups, we can provide some useful information for understanding the high T_c copper oxide superconductors.

5.4 Superconducting excitations in n-type $Nd_{1.85}Ce(Th)_{0.15}CuO_{4-y}$

As indicated in Fig. 5.4.a and Fig. 5.4.b, the most striking features of these data are low-frequency enhancements of the reflectance in the superconducting state. Above $\sim 100\ cm^{-1}$, there are no significant differences between normal and superconducting reflectances. From BCS theory [32] one expects a region of high reflectance below the gap energy with an abrupt decrease in reflectance at the gap energy. For the copper oxide superconductors, the situation is less clear. It was proposed that the infrared gap measurements on unoriented polycrystalline samples should be dominated by contributions with the electric field perpendicular to the Cu-O plane, and quite insensitive to the a-b plane gap [18] [67]. For the present measurement on polycrystalline $Nd_{1.85}R_{0.15}CuO_{4-y}$, we assume that the low-frequency effects are dominated by c-axis excitations, since our reflectance is much lower than unity in the low frequency range. Therefore we may expect to observe a gap energy excitation along c-axis from our infrared measurements on the ceramic bulk samples, due to the strong anisotropy of the high T_c copper oxides. Thus, the enhanced low-frequency reflectance seen in our data should be considered as it relates to a c-axis gap-like excitation. We found these edges of the plateau at $50 \pm 2\ cm^{-1}$ $(6.25 \pm 0.25\ MeV)$ for both compounds

corresponding to the BCS features with the gap ratio $2\Delta/k_bT_c$ of 3.1 ± 0.2 (Ce) and 3.9 ± 0.2 (Th) respectively. These values are within the range found for conventional metallic superconductors.

$2\Delta/k_bT_c$ is an important parameter of a superconductor. The values of $2\Delta/k_bT_c$ from our measurements on $Nd_{1.85}Ce(Th)_{0.15}CuO_{4-y}$ are in good agreement with tunneling results on a NCCO crystal by Huang et al. [143], in which $2\Delta/k_bT_c = 3.9$ and the coupling parameter $\lambda \sim 1.0$. Our infrared results are also confirmed by a tunneling measurement with $2\Delta = 57.6cm^{-1}$ $(7.2\ MeV)$ obtained by a research group at the Argonne National Laboratory (ANL) [152]. The samples of the ANL group and ours come from the same ceramic bulk prepared by J. L. Peng et al [119]. Our results are also consistent with the BCS calculation with gap ratio $2\Delta/k_bT_c \simeq 4.1$ obtained from a temperature dependences of penetration depth $\lambda_{||}(T)$ and surface resistance $R_s(T)$ [133].

A theoretical work on $Nd_{2-x}Ce_xCuO_{4-y}$ based on the conventional strong coupling theory was reported by H. Chen et al [153]. The Eliashberg equations were solved by using a realistic model of phonon density of states. Specifically, they find $2\Delta/k_bT_c = 4.458$ and the coupling parameter, λ, to be 1.135. These calculated properties of $Nd_{2-x}Ce_xCuO_{4-y}$ appear to be in reasonable agreement with available experimental results. For example, our infrared reflectance measurement on the Nd-214 shows a value of $2\Delta/k_bT_c$ around $3 \sim 4$. The tunnelling experiment by Huang et al. [143] also show the similar value of $2\Delta/k_bT_c$, which is 3.9, and the coupling parameter $\lambda \sim 1.0$. This study suggests that the mechanism of superconductivity in the n-type $Nd_{2-x}Ce(Th)_xCuO_{4-y}$ system may be similar to that in a conventional strong coupling superconductor. Our results provide the evidence to support this conclusion.

We point out that some significantly different results have been presented by Degiogi et al. [136] for $Nd_{1.85}Ce_{0.15}CuO_{4-y}$ where 100% reflectance is reported below 56 cm^{-1} at 6 K. This surprising result is unique among studies on polycrystalline materials and is difficult to understand, in view of the characteristics of such materials as described above. Superconducting reflectance rises above normal reflectance at about 130 cm^{-1}, rather than 60 cm^{-1} as in the present work. Based on analysis of these results, the authors in [136] have concluded that they could not determine the superconducting gap. It is possible that their sample surface contains crystallites preferentially aligned with the c axis perpendicular to the surface, yielding a much higher conductivity and reflectance. Clearly, additional work is required to confirm the reason for these differences.

5.5 Normal State Properties and Phonon Assignments

The remainder of the spectrum is almost temperature independent in the range studied. It has three quite distinct aspects: several sharp features superimposed on the spectral background between $100 - 700$ cm^{-1}, and a broad, sharply decreased overall reflectance in the range of 1000 and 2000 cm^{-1}, weak peak centered around 3000 cm^{-1}. We discuss each separately.

One of the common properties of high T_c copper oxides, including the n-type Nd-214 system, is the anisotropy. For our polycrystalline samples, reflectance spectra are considered as a composite of the contributions from a metallic $a-b$ plane and a nearly insulating c axis because of the random orientation of the crystallites. We therefore do not attempt to give a detailed fit of the spectra by the usual superposition of a

Drude term and Lorentz oscillator(s). It is interesting to fit the overall shape of the reflectance spectrum using a Drude function: $\epsilon(\omega) = \epsilon_\infty - \omega_p^2/(\omega^2 + i\omega/\tau)$, where ω, ω_p, τ, and ϵ_∞ are the incident-photon frequency, the plasma frequency, the relaxation time of the free carriers, and the background dielectric constant, respectively. The fit parameter will not have physical significance in themselves because they result from the complicated superposition of contributions in different crystalline directions. However, results can be compared with previous results on ceramic samples and with our results for the dc conductivity.

Drude fits are shown in the insets to Fig. 5.3.a and Fig. 5.3.b. Parameters of the fits are in terms of $\sigma_0 = \omega_p^2 \tau \epsilon = 40\ (\Omega cm)^{-1}$, $\tau = 1 \times 10^{-15}\ sec$, and $\epsilon_\infty = 2.2\ (Ce)$ and $1.9\ (Th)$. Our values of τ are in the same range as found for Y-Ba-Cu-O ceramics [129], [18]. With values of the Fermi velocity in the range $2 \times 10^8\ cm/sec$, we find mean free paths of about 20 Å. The values of σ_0 are in rough agreement both with the values $1/\rho_{dc} = 37\ (\Omega cm)^{-1}\ (Ce)$ and $131(\Omega cm)^{-1}\ (Th)$ (see Chapter 2) and with the low-frequency values of σ_1 (about $10^2\ \Omega cm^{-1}$) obtained by a Kramers-Kronig analysis.

The conductivity of our $Nd_{1.85}Ce(Th)_{0.15}CuO_{4-y}$ samples in the low-frequency range rapidly decreases, as shown in Fig. 5.5.a and Fig. 5.5.b. It shows a poor metal behaviour and the conductivity is considerably lower than values observed in the Y-Ba-Cu-O system. The carrier density calculated from the Drude-fit parameters is $n = \sigma_0 m/\tau e^2 = 1.4 \times 10^{20}\ cm^{-3}$, assuming free-electron mass and charge; this should be compared with values of about $10^{21}\ cm^{-3}$, found for $Y-Ba-Cu-O$ polycrystalline samples [129], [18]. This leads to a plasma frequency of about 3500 cm^{-1}, which is also much lower than that of about 5900 cm^{-1} in ceramic Y-Ba-Cu-O samples [129], [18]. The plasma frequency, $\omega_p = 3350\ cm^{-1}$, found by M. S. Sherwin et al.[142] for the hole-type ceramic superconductor $La_{1.85}Sr_{0.15}CuO_4$ is similar to ours. Their fit,

however, included a Lorentz oscillator and gave a high value of ϵ_∞, so the results are not strictly comparable.

Our results should also be compared with the near-infrared reflectance of $Nd_{1.84}Ce_{0.16}CuO_4$ thin films measured by Hirochi *et al.* [144]. Their films were highly oriented with the c axis normal to the $SrTiO_3$ substrate. They got much higher reflectivities (e.g., about 0.35 at 4000 cm^{-1}). Their fit with the Drude model yielded longer relaxation times by a factor of about 4 and much higher carrier concentrations, in the range of 10^{22} cm^{-3}. The differences of our results and those from Hirochi *et al.* are clearly due to the differing orientations of the films.

The sharp features between 100 and 700 cm^{-1} are clearly due to lattice vibrations. Because their contributions to the optical constants are additive to those of the charge carriers, it is difficult to perform precise determinations of the mode energies. As noted above, fitting the data with a superposition of a Drude model and Lorentz oscillation was not attempted. Instead, we used the energies of the peaks in σ_1, obtained through a Kramers-Kronig analysis (Fig. 5.5.a and Fig. 5.5.b), with constant extrapolation of reflectance above 10000 cm^{-1} and below 20 cm^{-1}. Although the magnitudes of the calculated optical constants will not be meaningful due both to the extrapolations and to the polycrystallinity of the samples, the locations of the peaks will nevertheless yield the mode energies. Mode energies, obtained in this manner, are given in Table 5.5 [148].

Assignment of the peaks has been made by the use of works on Nd_2CuO_4 [145] [136] [138], Pr_2CuO_4 [146], and La_2CuO_4 [160] systems. It is known that Nd_2CuO_4 with a tetragonal crystal structure, like $La_{2-x}Sr_xCuO_4$ [147] by Bates and J. Eldridge, has $I_{4/mmm} = D_{4h}^{17}$ symmetry with seven atoms per unit cell [150]. Seven infrared-

Table 5.1: Phonon Assignment of $Nd_{1.85}Ce(Th)_{0.15}CuO_{4-y}$

Frequency (cm^{-1})		Orientation	Symmetry	Type
(Ce)	(Th)			
139	137	a-b	E_u	Nd-O bend
275	275	c	A_{2u}	Nd-O stretch
320	320	a-b	E_u	O bend
409	$\cdots$	c(?)	A_{2u}(?)	Nd(?)
518	517	c	A_{2u}	Cu-O stretch
594	593	a-b(?)	E_u(?)	(?)
670	670	a-b	E_u	Cu-O stretch

Assignments marked "?" are considered tentatively or missing in the observation due to either the strong plasmon screening effect in ab-planes or the overlap with other infrared-active modes.

active modes are expected, four of them being E_u modes raising from $a-b$ planes and three of them A_{2u} modes parallel along the c axis. The positions of phonons are determined with respect to the peaks from the conductivity spectrum by Kramers-Kronig analysis of the Nd-214 samples. Strength is measured with respect to the background reflectance attributed to free carrier effects. Phonon assignment for the experimental spectra are shown in Table 5.5. Assignments marked "?" are considered tentative or missing in the observation due to either the strong plasmon screening effect in $a-b$ planes or the overlap with other infrared-active modes. For example, an E_u mode around 500 cm^{-1} cannot be distinguished from an A_{2u} mode at 518 cm^{-1}.

We note that three of the modes shift to (very) slightly lower frequency upon replacement of Ce by the heavier Th, suggesting that these modes involve some motion of the Ce (or Th) ion. A simple isotopic-substitution model (i.e., no change in interionic force constants) would predict a 29% shift in the frequency of a mode which involves only that ion. However, there is no explicit evidence of this in our results, implying that most of the observed infrared-active modes do not significantly involve Ce or Th. The only possible exception is the mode at 409 cm^{-1} in the Ce compound which has no counterpart in the spectrum of the Th sample. It is possible that this mode does involve Ce significantly and its counterpart in the Th sample (if present) is obscured by another feature. The fact that the feature strengthens with increased temperature indicates that it may, in fact, merely be defect-induced and not an intrinsic mode of the system. We observed none of the Raman-active modes reported previously [151], although one might expect disorder caused by O vacancies which destroy translational symmetry to permit Raman-active modes to be observed.

5.6 Conclusions

We have performed measurements and analyses of the infrared reflectance spectra of $(Nd_{1-x}R_x)_2CuO_{4+\delta}$ (NCCO) system, where $R = Ce$ and Th. Our experimental results display a gap-like feature at $\sim 50cm^{-1}$ for both $Ce-doped$ and $Th-doped$ samples corresponds to $2\Delta/k_bT_c$ of 3.1 ± 0.2 (Ce) and 3.9 ± 0.2 (Th) respectively. These values have shown a clear quantitative agreement with the s-wave BCS theory, and are in consistent with the results from other electrodynamics measurements, i.g., tunneling, penetration depth, et al.. All together these results indicates, in contrast to other high-temperature superconductors and theoretical suggestions for high-temperature superconductivity, NCCO shows evidences of a single-valued and finite gap ratio, and its optical properties can be explained within the conventional theory. Thus the nature of the superconducting state of the n-type high-temperature superconductor is possibly very similar to that of conventional superconductors, supporting some earlier speculation for such similarity between NCCO and conventional superconductors.

We believe that NCCO may be the simplest and most easily understood example of cuprate superconductor because of its low T_c and relatively isolated CuO2 planes. With the observation of s-wave BCS-like behavior in NCCO, some questions naturally arise: why do optical and electrodynamics measurements on the other cuprates display non-BCS behavior? Is this due to extrinsic phenomena, or a consequence of different pairing state symmetries in the other cuprates and in NCCO? These questions call for further systematic and detailed studies of the electrodynamics of all the high-T_c cuprates.

Chapter 6

Infrared Studies of Effects of Ni Impurities in $YBa_2(Cu_{1-x}Ni_x)_3O_{6.95}$

6.1 Introduction

One of the central questions in the study of high-T_c superconductors concerns the possibility that the superconducting state is something other than the conventional s-wave BCS pairing state. Briefly, BCS theory shows how electron-phonon interactions can lead to a net attraction and pairing of electrons near Fermi surface. At very low temperatures, the attracting force between electrons is strong enough to overcome the Coulomb repulsion and encourage formation of correlated electrons pairs with total spin zero which allows Boson-like condensation into a single energy state, and results in a gap in energy between paired and unpaired electrons around the Fermi surface. This is so-called s-wave superconductor model. In a simple s-wave BCS model, gap has a width of $2\Delta_0$ at $T = 0$ around the Fermi surface with $2\Delta_0/k_BT_c \cong 3.5$ for weak coupling or higher for stronger coupling. This model predicts a rise to 100% reflectance and zero absorptance at T=0 for photons below the energy $2\Delta_0$ [29] [30]

[32].

Far-infrared techniques can be a sensitive probe and hence can be used to investigate the electrodynamics of the pairing state. However, reflectance studies on $YBa_2Cu_3O_{7-\delta}$ thin films and crystals [17] have shown that nearly all of the spectral weight associated with the Drude conductivity collapses into the zero-frequency δ function, so that no transitions across a gap will be observed. This result is consistent with the short coherence length observed in these materials, and places them in the clean-limit [90]. As discussed by Kamaras et al. [90], pure $YBa_2Cu_3O_{7-\delta}$ is in the clean-limit, which presents the normal skin effect regime of superconductivity with $\Gamma \ll 3.5k_BT_c$; $\xi_0 \ll l \ll \lambda_L$, where Γ is the scattering rate represented in wavenumber cm^{-1}, as denoted in chapter 2; ξ_0, l, and λ are the coherence length, mean free path, and penetration depth, respectively.

For a near-perfect normal metal, Γ is very small, ≈ 0, the reflectivity approaches unity below the plasma frequency. Above the plasma frequency, the metal is transparent and the reflectivity decreases rapidly with increasing frequency. The spectral weight of the frequency-dependent conductivity $\sigma_1(\omega)$, then, is distributed mostly in the low-frequency range, as discussed in Chapter 2. The normal state frequency-dependent reflectance and conductivity $\sigma_1(\omega)$ of a clean superconductor have similar behavior to a near-perfect metal. In the superconducting state, most of the spectral weight is transferred to the delta function at zero frequency as the Drude component condenses below T_c and the gap feature in the superconducting state can be too weak to be detected by the infrared technique, as schematically shown in Fig. 6.5. Therefore, in "clean" superconductors, the gap might not show up in the infrared spectrum because the normal state scattering rate Γ of the charge carriers may be too small relative to the superconducting energy gap ($\Gamma \ll 2\Delta_0$), and infrared spec-

troscopy cannot distinguish the change between a near-perfect conductor and a true superconductor [90].

Another possible reason for the gap not showing up in the far-infrared conductivity spectrum is that the gap may have nodes on the Fermi surface, and therefore the superconducting pairing energy would be distributed from zero energy to the "gap" Δ_0, which measures the maximum gap amplitude about the Fermi surface (see Fig. 6.6 for detail). Conductivity in the superconducting state then would be a continuum starting from zero frequency, instead of starting from $2\Delta_0$ at $T = 0$ as predicted by conventional s-wave BCS theory. All these possibilities give rise to substantial complications for measuring an energy gap by infrared techniques.

Deliberately introducing impurities into a pure high-T_c crystal could provide an opportunity to investigate the gap controversy in high-T_c materials, since impurity induced defects can enhance the scattering rate Γ and make it comparable to $2\Delta_0$, thus moving the superconductor into the dirty-limit where the scattering rate, Γ, is comparable to the gap size, $\Gamma \simeq 2\Delta_0$ [90]. Once a superconductor is in the dirty-limit, the normal state spectral weight is re-distributed to higher frequency range. That means, not all the normal Drude component collapses into the δ-function at 0-frequency, leads to a strong enough gap feature at $2\Delta_0$ in this case. Therefore, it is possible to see a gap in the conductivity spectrum $\sigma_1(\omega)$, as illustrated in Fig. 6.5. We can therefore produce optimum circumstances for the observation of the spectroscopic gap by substituting impurities in high-T_c systems.

In this chapter, a systematic study of the far-infrared reflectance of Ni-doped $YBa_2Cu_3O_{6.95}$ single crystals is presented. This is a continuing study of substitution effects on the $YBa_2Cu_3O_{7-\delta}$ system after our earlier investigation of Zn-doped YBCO;

see Chapter 3 for detail.

The comparison between Zn and Ni-doped YBCO is interesting. Ni and Zn impurities have been both found to preferentially substitute for $Cu(2)$ sites in the CuO_2 planes in the $YBa_2Cu_3O_{7-\delta}$ crystal structure [34] [35]. Thus, they provide means of specifically disturbing the CuO_2 planes in which the superconductivity is thought to originate, and that are the key element common to all of the high T_c superconductors. Other dopants such as Al, Co, and Fe prefer the CuO chain sites. Both Ni and Zn are in +2 charge states and Zn^{2+} is spin 0 ($3d^{10}$) while Ni^{2+} is spin 1 ($3d^8$), which indicates that Ni may be a magnetic impurity in a lattice. Both may induce local magnetic moments in the lattice when they substitute for a spin-1/2 Cu atom in the CuO_2 planes.

It has been reported [94] that Ni impurities increase the dc resistivity above T_c as much, or more than, Zn. That is, Ni provides at least as much scattering of the holes as Zn does. However Ni has a much less drastic effect on T_c than Zn. Susceptibility measurements of T_c by D. Bonn et al. [99] show that the suppression of T_c with impurity content is $\partial T_c/\partial x \sim 390K/x$ and $T_c = 91K$, and $89K$ for Ni-doped single crystals $YBa_2(Cu_{1-x}Ni_x)_3O_{6.95}$ with $x = 0.0075$, and 0.014, respectively. Zn-doped YBCO single crystal, on the other hand, gave $\partial T_c/\partial x \sim 1260K/x$. Thus Ni suppresses T_c at a rate about one-third of that Zn does and therefore has a much less drastic effect on pair-breaking than Zn [99].

An NMR study has shown, at a microscopic level, that Zn doping induces a finite density of states at the Fermi level, causing gapless superconductivity [106]. This NMR study has also indicated that small amounts of Ni impurities do not make $YBa_2Cu_3O_{7-\delta}$ gapless, as does the presence of Zn impurities which appear to have

a strong pair-breaking effect. Microwave studies [100] [107] show that Ni impurities increase the normal-state scattering rate but do not affect the linear behaviour of the penetration depth at low temperature. These results are the opposite of what is expected in an s-wave superconductor, in which a small amount 3d-transition-metal magnetic impurities drives $T_c \rightarrow 0$ [97].

To summarize, a small amount of Ni-doping does not change the nature of superconductivity since it hardly affects T_c and the density of states at the Fermi surface [106]. On the other hand, Ni-doping increases the scattering rate and may move a superconductor from clean-limit into dirty. Therefore, substituting Ni into $YBa_2Cu_3O_{7-\delta}$ is particularly interesting to far-infrared measurements for investigating the nature of a superconducting pairing state.

The motivation behind this study is two fold. First, the difficulties in observing features associated with a gap in clean-limit systems motivate us to study the effect of impurities on the optical conductivity. Secondly, doping impurities in the CuO_2 planes may move the superconductor away from the clean-limit and allow a distinction between unconventional (extended s-wave or d-wave) and anisotropic conventional (s-wave) models. By examining the low frequency optical response of Ni-doping on the ab-plane of untwinned single crystals $YBa_2Cu_3O_{6.95}$, we hope to gain more insight into the nature of the high-T_c superconductivity.

6.2 Experiment Details

The reflectance is measured at a near-normal angle of incidence for the samples on a Bruker IFS 113V Fourier transform interferometer from $\approx$ 50 to 3000 cm^{-1}. In the far infrared range, a 4.2 K silicon bolometer was used with beam splitters: 25 μm mylar

for $30-80\ cm^{-1}$; 12 μm mylar for $50-200\ cm^{-1}$; and 3.5 μm mylar for $150-700\ cm^{-1}$. In the mid infrared range, a LN_2 MCT detector was used with beam splitters: 1.5 μm mylar beam splitter for $500-1000\ cm^{-1}$; and KBr for $800-5000\ cm^{-1}$. All the optical components used in the experiments are listed in Table 6.1 for convenience.

The whole sample set up for the reflectance measurement was designed by C. C. Homes, for detail, see Ref.[69]. The sample is glued to the apex of a pyramidal cone, oriented so that light is incident on a face of the crystals that contains the a-b plane, and then mounted in a R. G. Hansen High-Tran continuous-flow cryostat. The High-Tran unit is isolated from the Bruker system by a sliding multiple-window holder which can accommodate two 25mm-diameter windows: one is a 2-mil polypropylene for the FIR range and the other one is a KBr window for measurements above $\approx$ $400\ cm^{-1}$. To ensure good thermal contact, the brass cone holding the samples is in contact with a copper braid connected to the cold finger of the flow dewar. The reflectance R_s of the samples is compared to the reflectance R_m of a stainless-steel reference mirror. To correct for the sample size and any scattering effects caused by the surface microstructure and irregularities, and to eliminate the effects of the reference mirror, the sample is coated with gold by an *in situ* evaporation technique. This produces a layer of gold of $\geq 3\delta$ (where δ is the classical skin depth) at 100 cm^{-1}, which ensures that multiple reflections do not occur. The measurements are then repeated on the gold-coated sample to yield R_{gs}. The effects of the reference mirror may be removed by dividing these two ratios

$$\left(\frac{R_s}{R_m}\right)\left(\frac{R_{gs}}{R_m}\right)^{-1} = \frac{R_s}{R_{gs}}, \tag{6.1}$$

which yields the reflectance of the sample with respect to gold. The reflectance for gold is well known [98], and the reflectance can subsequently be corrected by multiplying

Table 6.1: Optical Components for the Bruker IFS 113V Used in the Experiments

Frequency Range (cm^{-1})	Source	Beam Splitter (for High-Tran)	Window	Detector
20-120	Mercury lamp*	25μm Mylar	Polypropylene	4.2 K Bolometer
50-220	//	12μm Mylar	//	//
150-700	//	3.5μm Mylar	//	//
500-1000	Globar	//	Poly/KBr	LN_2MCT
500-5000	Globar	KBr/Ge	KBr	//

* With a thin black polyethylene optical filter to block out UV radiation.

the ratio by the reflectance of gold to yield the absolute reflectance of the samples. The uncertainty of the reflectance of gold is $\pm 0.5\%$. This introduces an uncertainty in the absolute value of the reflectance of sample of $\pm 0.5\%$. The noise level in the reflectance is typically less than $0.1 - 0.2\%$.

High-quality single crystals of pure and Ni-doped $YBa_2Cu_3O_{6.95}$ with mirror smooth ab-plane surfaces were grown using the flux method by R. X. Liang *et al.* of the Physics department at the University of British Columbia [101]. High purity Y_2O_3 (99.999%), CuO (99.999%), $BaCO_3$ (99.997%), and NiO (99.999%) were mixed in a power mortar with agate components. The mixed powder was pressed into a pellet and placed into a yttria stabilized zirconia (YSZ) crucible. The pellet was first heated up to 850^oC for 4 hours to evaporate carbonates, then to 1010^oC for 4 hours and cooled down to 990^oC. After 8-18 hours at 990^oC, the sample was slowly cooled at a rate of $0.3-0.8^oC/h$ to $970-950^oC$. The material was then poured onto a porous ceramic. Finally, the sample was cooled to room temperature at a rate of $150^oC/h$. The purity of the samples was evaluated by ion conductive plasma (ICP) mass spectroscopy and it was found that the total concentration of the principal contaminants, Al, Fe, Zn, was less than 0.002 atoms/unit cell. The as-grown crystals were subsequently annealed for 7 days in oxygen and oxygen content was set at 6.95 ($\delta = 0.05$) [95]. For the pure $YBa_2Cu_3O_{6.95}$ single crystal used in our experiments, the oxygen content yields a T_c near 93.5 K and outstanding bulk homogeneity is demonstrated by a specific heat jump at T_c that is very narrow, only 0.25 K wide. The crystal is almost defect free since the scattering rate at $T = 4K$ is as small as 1 cm^{-1} [100]. For our two Ni-doped samples, $T_c = 91K$ with the transition width 1.1 K, and $89K$ with width 1.3 K for $x = 0.0075$, and 0.014, respectively [100].

The typical dimensions of the single crystal we used in our experiments is about

$1.5mm \times 1.5mm$ in the a-b plane with thickness of $\approx 50\mu m$ along the c-axis.

6.3 Reflectance and Conductivity of $YBa_2(Cu_{1-x}Ni_x)_3O_{6.95}$

The ab-plane reflectance of an $YBa_2(Cu_{1-x}Ni_x)_3O_{6.95}$ twinned single crystals is shown in Fig. 6.1.a, Fig. 6.1.b, and Fig. 6.1.c for $x = 0$, 0.0075, and 0.014 respectively. The spectra presented here are from 50 cm^{-1} to 1000 cm^{-1} for several temperatures above and below T_c.

As Fig. 6.1 shows, in the low-frequency range, the reflectance of the three samples rises as temperature decreases. At 10 K, in the low-frequency range the reflectance R in the undoped crystal is quite high, and is greater than 99% below $\approx 200cm^{-1}$. Above this frequency R falls off slowly, with a pronounced shoulder at about 440 cm^{-1}, then drops steeply down. When $x = 0.0075$ Ni was added into the system to replace the Cu sites in the ab-plane, the reflectance is slightly decreased but still greater than 99% until $\approx 175cm^{-1}$. At 10 K in the $x = 0.014$ Ni-doped crystal, the reflectance at the lowest measured frequency starts lower than unity (greater than 99% below $\approx 100cm^{-1}$), but is extrapolated to unity as $\omega \to 0$. The reflectance of the two Ni-doped single crystals follow the similar R vs. ω behavior of the pure sample, except that the average reflectance of the heavier doped one is significantly lower below ≈ 500 cm^{-1} than in the pure material, as shown in Fig. 6.1.a.

In the normal state, as Ni is introduced to the system the reflectance shows a less dramatic change than it does in the superconducting state. In both the normal and superconducting states, additional vibrational structures are superimposed on the ab-plane reflectance. These features are resolved well above the noise level and become

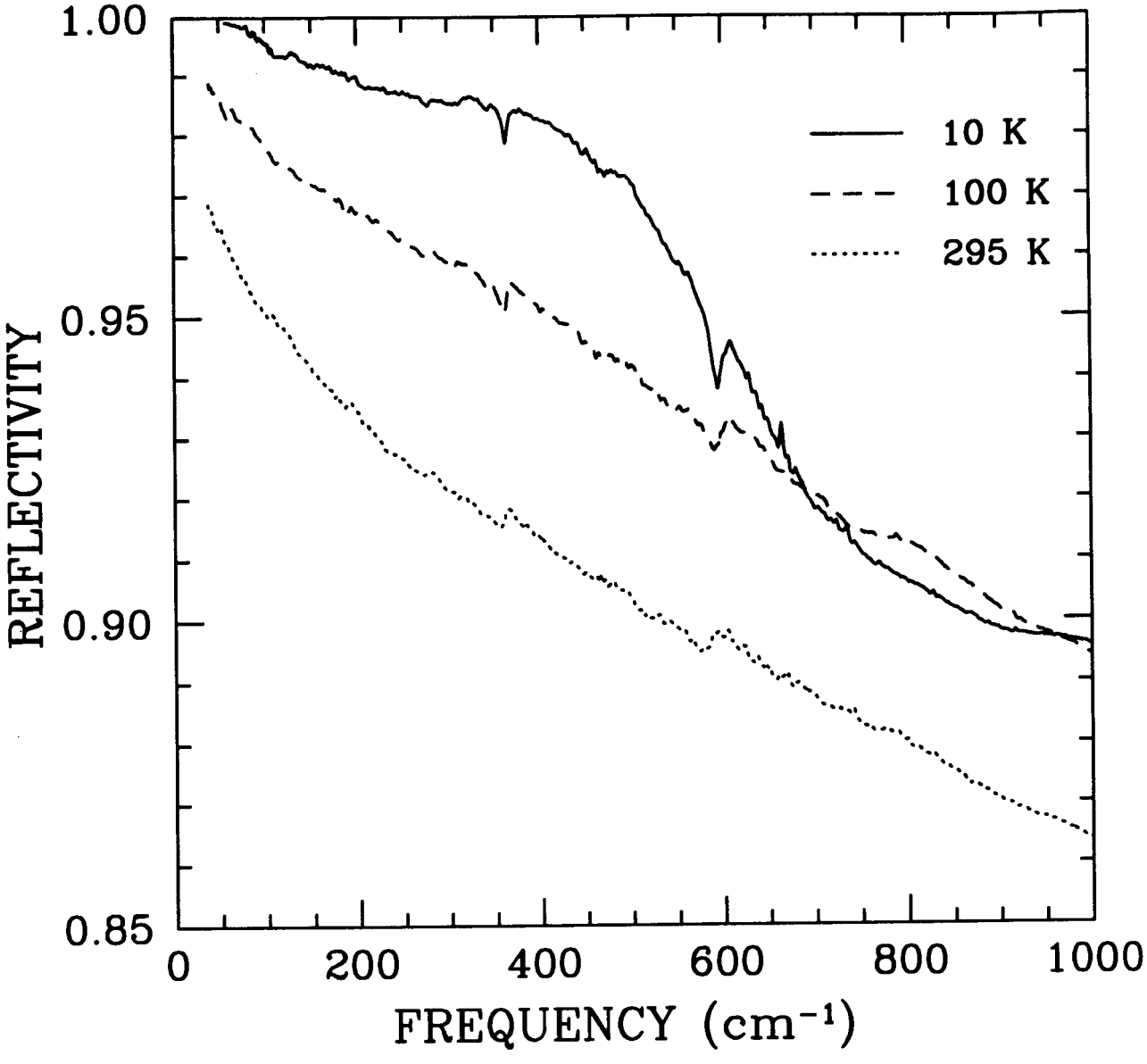

Figure 6.1.a: Reflectivity of the twinned pure $YBa_2Cu_3O_{6.95}$ single crystal from $\approx 50 - 1000cm^{-1}$ at 295 K, 100 K, and 10 K. $T_c = 93.5K$.

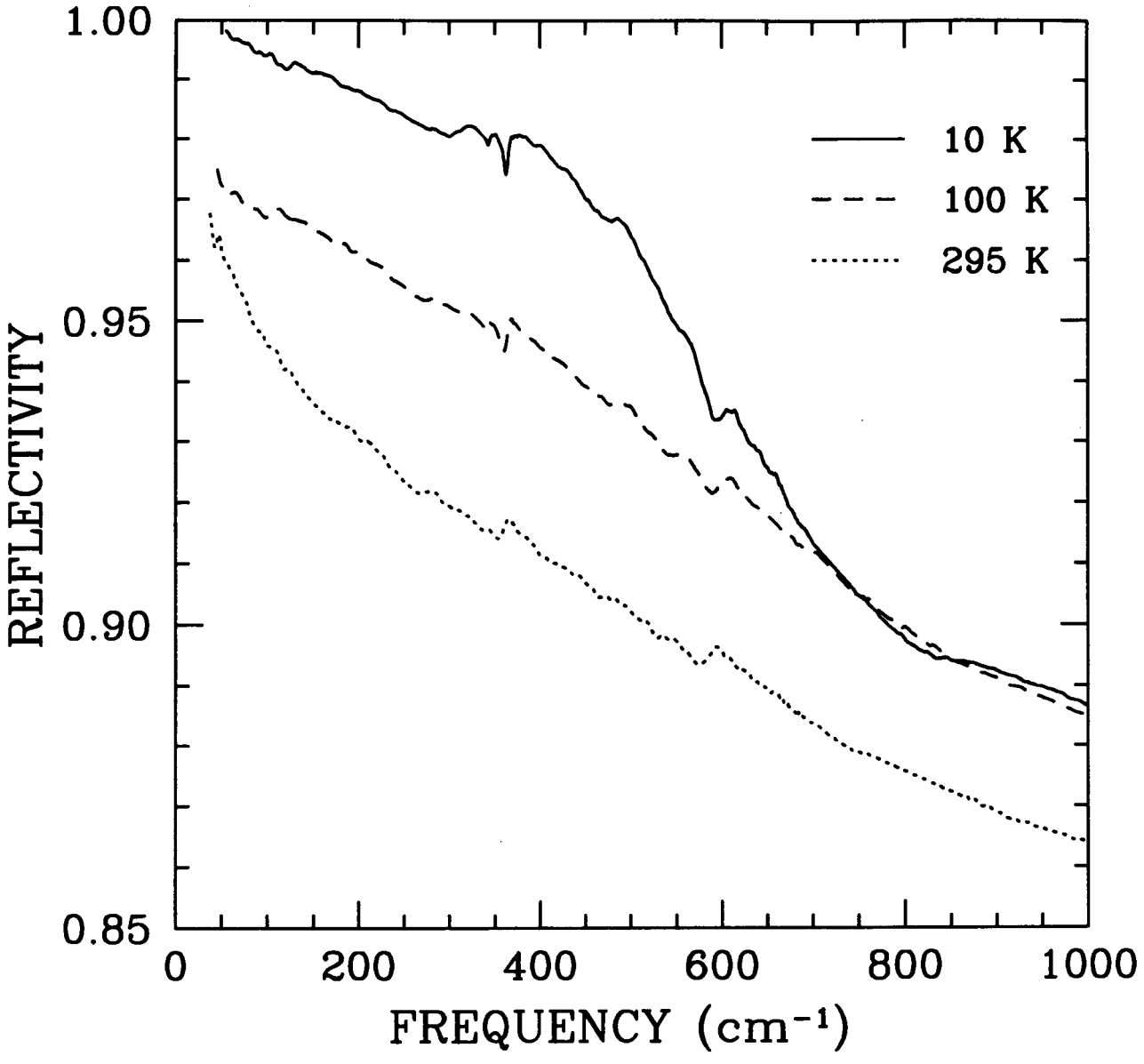

Figure 6.1.b: Reflectivity of twinned $YBa_2(Cu_{1-x}Ni_x)_3O_{6.95}$, $x = .75\%$, from $\approx 50 - 1000cm^{-1}$ at 295 K, 100 K, and 10 K. $T_c = 91K$.

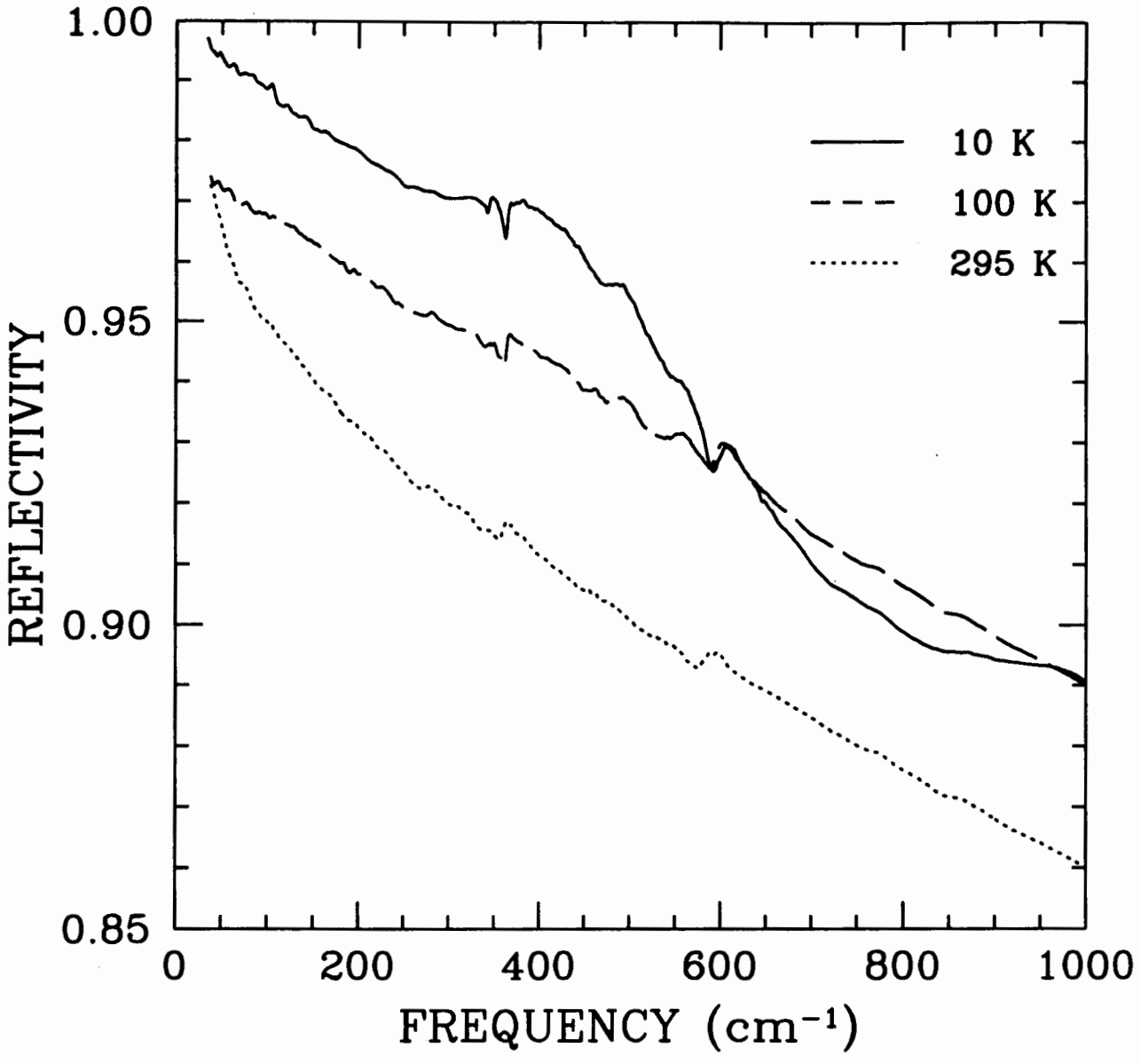

Figure 6.1.c: Reflectivity of twinned $YBa_2(Cu_{1-x}Ni_x)_3O_{6.95}$, $x = 0.014$, from $\approx 50 - 1000cm^{-1}$ at 295 K, 100 K, and 10 K. $T_c = 89K$.

more apparent in the optical conductivity spectra, calculated by using a Kramers-Kronig transformation, as shown in Fig. 6.2. Above 1000 cm^{-1} the reflectance of the two Ni-doped samples is almost identical to that of the pure one.

Above 3000 cm^{-1} the reflectance of all the samples is nearly temperature independent (spectra with frequency higher than 1000 cm^{-1} not shown in the thesis), so we used the data in Ref. [102] by Romberg et al. to extrapolate the reflectance up to 3.5×10^5 cm^{-1} $(45eV)$ above which we assume a free-electron behavior: $(1-R) \propto \omega^{-4}$. At low frequencies the particular extrapolation chosen does not have much influence on the conductivity in the region where actual measurements exist. In the normal state the reflectance was extended by a Hagen-Reubens frequency dependence: $(1-R) \propto \omega^{-1/2}$. In the superconducting state the "Gorter-Casimir" two-fluid model was used for the extrapolation below ≈ 40 cm^{-1}. On the two-fluid model of a superconductor, briefly, at temperatures $0 < T < T_c$ the current density may be written as the sum of the contributions of normal and superconducting electrons: $j = j_N + j_S$, where $j_N = \sigma_0 E$ and j_S is given by the London equation $j_S = -c/4\pi\lambda_L^2 A$. At the frequency ω is much lower than the scattering rate Γ, $\omega \ll \Gamma$, the supercurrent j_S short-circuits the normal electrons and the reflectance for $\omega \to 0$ goes as: $(1-R) \propto \omega^{-2}$[29]. With such extrapolations of the reflectance, the optical conductivity and other constants were then calculated by using a Kramers-Kronig transformation from the complex reflectivity $\tilde{r} \sim R(\omega)e^{i\theta(\omega)}$, where $R(\omega)$ is the measured reflectance, $\theta(\omega)$ is the phase (for detail, see Ref.[31] or Chapter 2),

$$\theta(\omega) = \frac{\omega}{\pi}\int_0^\infty \frac{\ln R(\omega') - \ln R(\omega)}{\omega^2 - \omega'^2} d\omega' . \tag{6.2}$$

and the optical conductivity corresponding to the reflectance spectra are shown in Fig. 6.2.a, Fig. 6.2.b, and Fig. 6.2.c for $x = 0$, 0.0075, and 0.014 respectively.

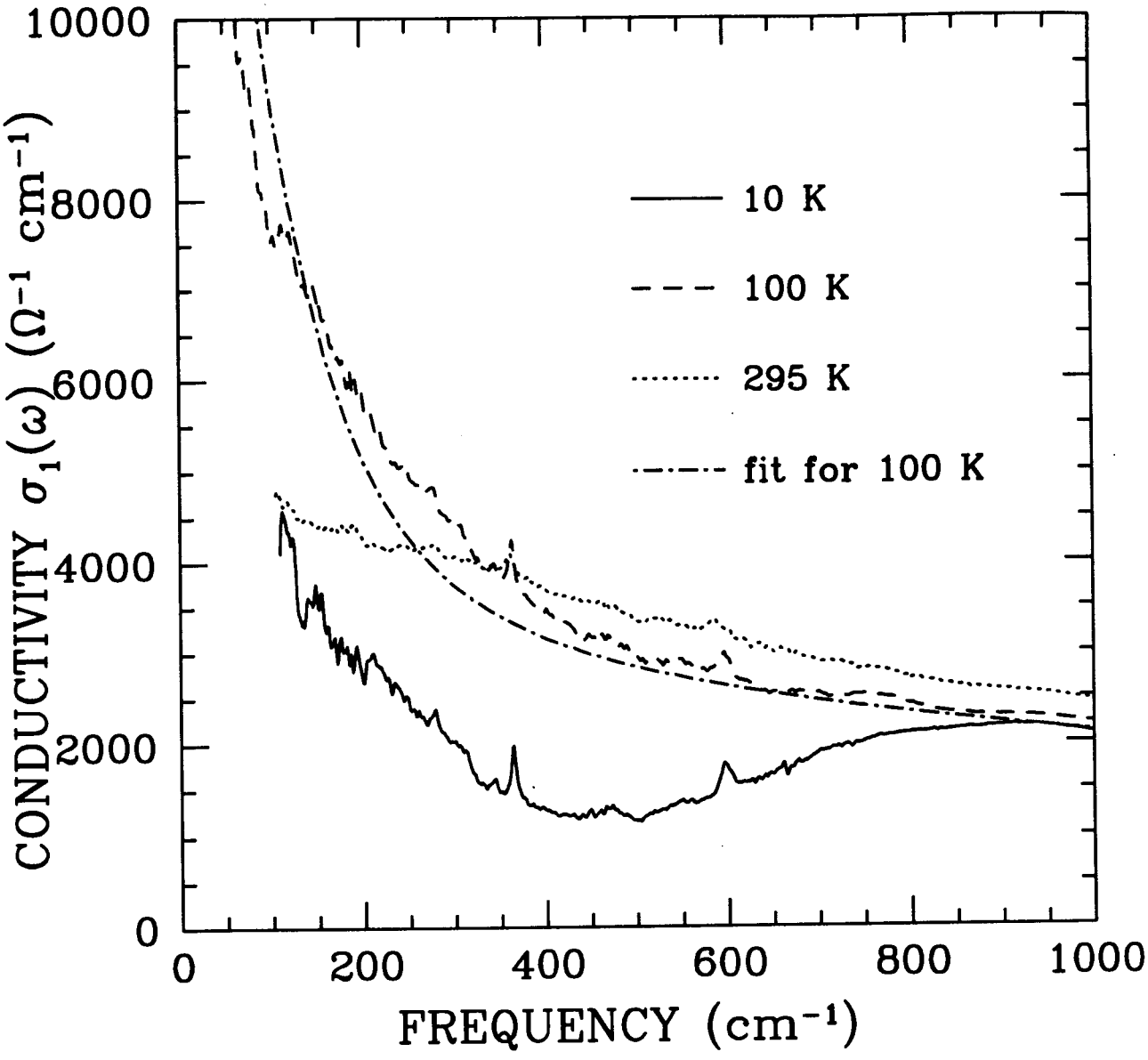

Figure 6.2.a: Conductivity of the pure $YBa_2Cu_3O_{6.95}$ twinned single crystal, from $\approx 50 - 1000cm^{-1}$ at 295 K, 100 K, and 10 K.

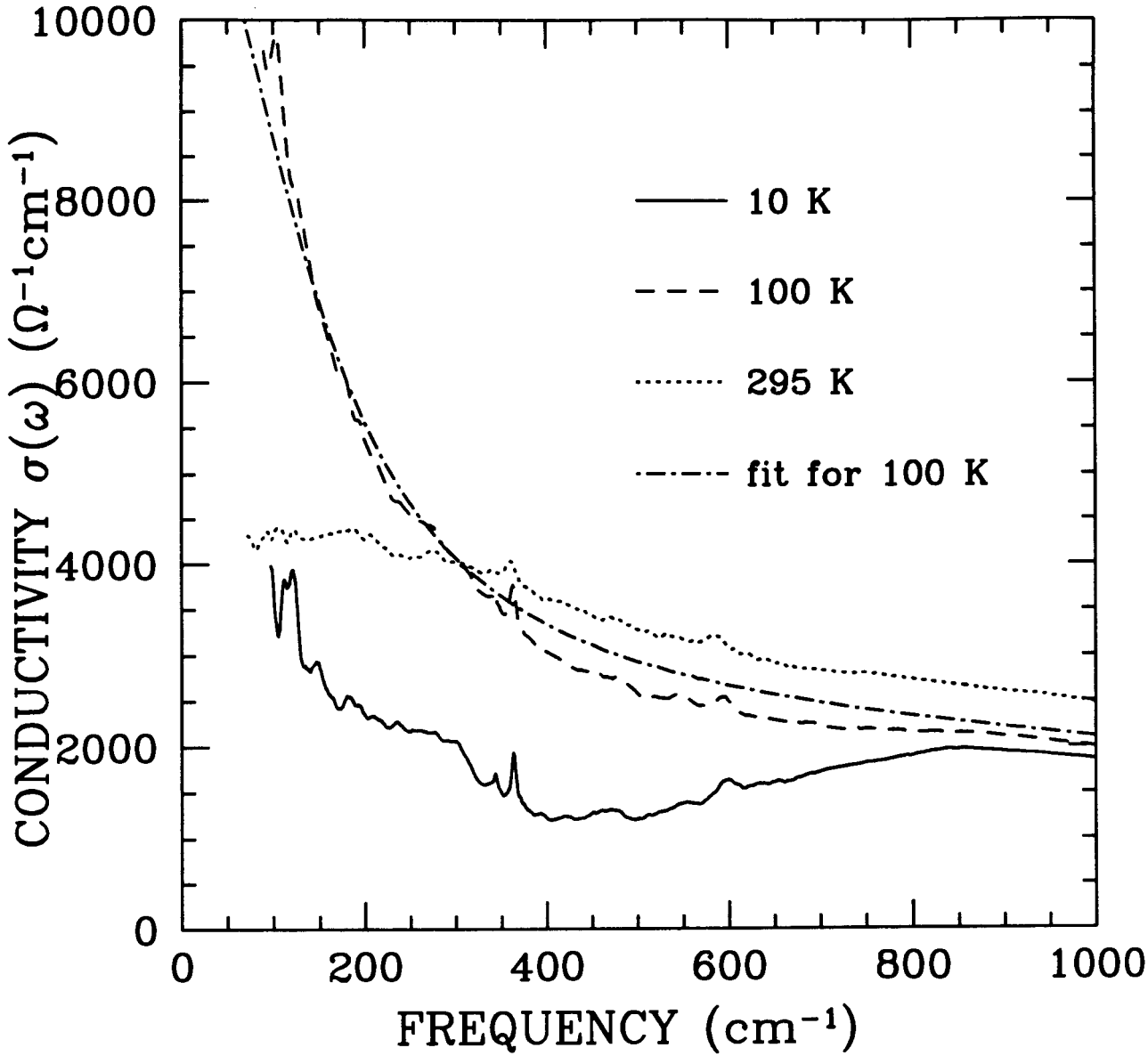

Figure 6.2.b: Conductivity of $YBa_2(Cu_{1-x}Ni_x)_3O_{6.95}$ twinned single crystal, x = .75%, from $\approx 50 - 1000cm^{-1}$ at 295 K, 100 K, and 10 K.

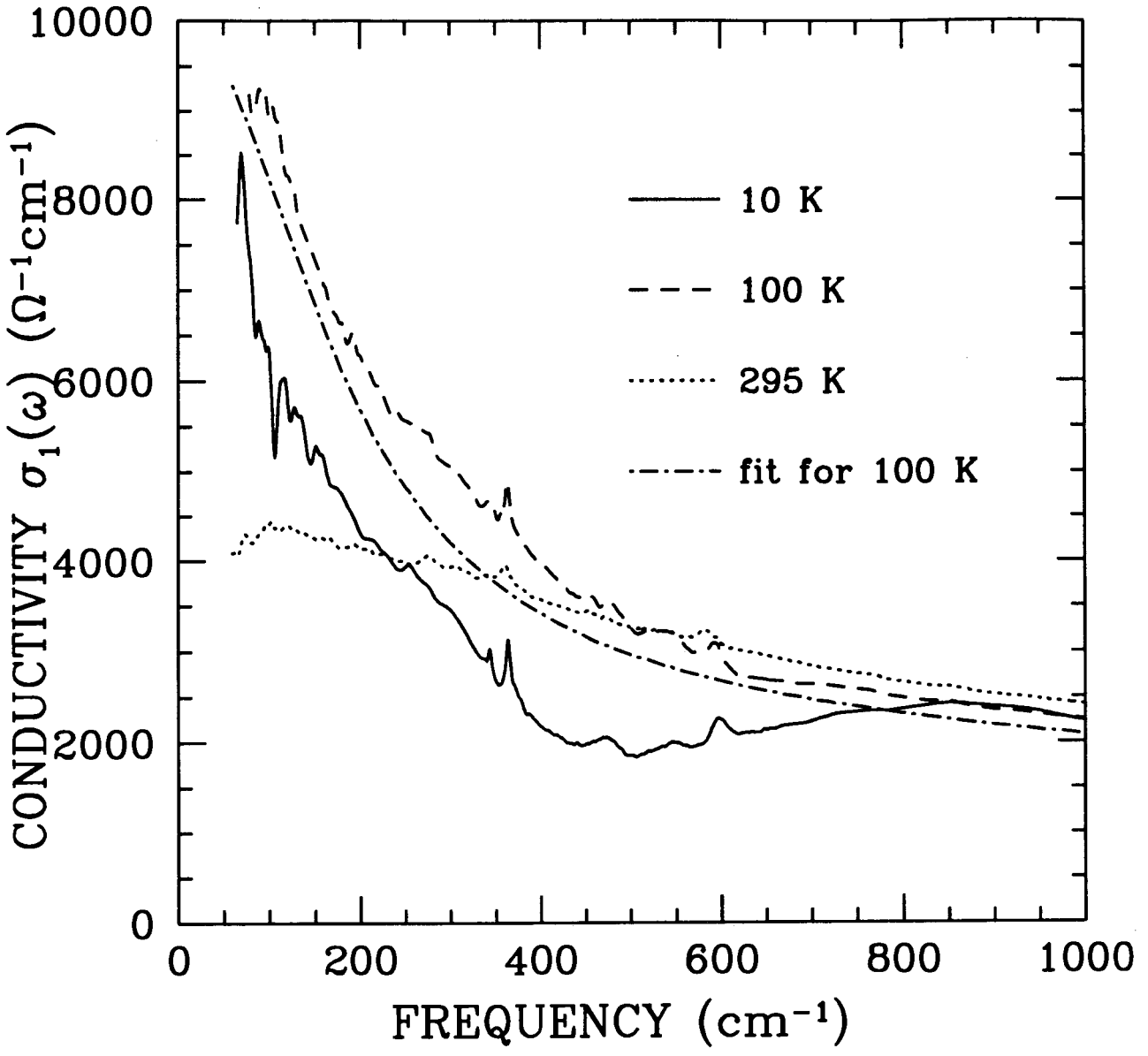

Figure 6.2.c: Conductivity of $YBa_2(Cu_{1-x}Ni_x)_3O_{6.95}$ twinned single crystal, $x = 0.014$, from $\approx 50 - 1000cm^{-1}$ at 295 K, 100 K, and 10 K.

Our overall ab-plane conductivity of the pure crystal is in good agreement with the recent results by D. N. Basov *et al.* [104] [110].

As indicated in Fig. 6.2, cooling down the samples from room temperature to $100K$ leads to a strong increase of the conductivity in the low-frequency range. Ni impurities do not strongly affect the normal state conductivity $\sigma_N(\omega)$. In the superconducting state, some of the low-frequency conductivity appears to condense to the delta function at zero frequency and the remaining conductivity can be attributed to: (i) a mid-infrared component which shows little temperature dependence (this component is above 1500 cm^{-1} and is not shown here); and (ii) a considerable large amount of low frequency conductivity (below 500 cm^{-1}, see Fig. 6.2), which is called the residual conductivity. The high quality of the crystal suggests that the residual conductivity below T_c is intrinsic to $YBa_2Cu_3O_{6.95}$ and is not due to sample imperfections. Instead, the existence of residual conductivity in the undoped material is consistent with a d-wave or extanded s-wave superconductor, as discussed by Carbotte *et al.* [108]. Thermal excitations of quasiparticles may be the cause of the residual conductivity at low frequency [105].

The combination of these two components results in a broad dip feature which occurs at $\approx$ 500 cm^{-1}, as shown in Fig. 6.2. With decreasing temperature the 500 cm^{-1} minimum grows deeper and the residual conductivity becomes weaker below T_c. A recent infrared study on radiation-damaged single crystals of $YBa_2Cu_3O_{6.95}$ by Basov *et al.* [110] shows similar behavior of conductivities in this frequency range. Their results show that the onset of the broad feature centred at $\approx$ 500 cm^{-1} is quite evident in the normal state, above T_c, and thus it is very unlikely to be associated with the superconducting gap. We therefore can conclude that, down to the low-frequency limit of our measurements, no obvious BCS energy gap feature is observed

in the conductivity spectra.

The conductivities of the two Ni-doped samples are almost identical to that of the pure crystal in the low-frequency region except that two changes take place, as shown in Fig. 6.2: (i) in the superconducting state, the dip near 500 cm^{-1} is less pronounced in the Ni-doped crystals and the low-frequency residual conductivity at $\leq$ 500 cm^{-1} is enhanced as Ni doping levels increase; (ii) in the normal state at 100 K the scattering rate is increasing with Ni-doping. These results are found to be inconsistent with isotropic s-wave but display most of the expected qualitative features for d-wave or extended s-wave. This will be discussed in detail in the next section by comparing with recent theoretical calculations of the far infrared conductivity, as well as studies of radiation damaged samples of $YBa_2Cu_3O_{6.95}$ [110]. The effects of disorder on superconductivity in these systems will be also discussed. To investigate these changes, we fit the conductivity of the three crystals using a Drude-Lorentz model for the complex dielectric function.

6.4 Optical Properties

In the normal state, a two-component model has been reported [17] as a successful phenomenological approach for the ab-plane conductivity data fitting. In the two-component picture, high-T_c superconductors can be viewed as containing two types of carriers: free carriers which are responsible for the dc conductivity and condense to form the superfluid in the superconducting state; and bound carriers which involve bound electrons of uncertain origin and have a semiconductor-like gap for excitations from their bound states. The conductivity therefore is ascribed to contain two channels: a Drude component with a temperature-dependent damping, and several

Lorentzian oscillators which represent incoherent bound excitations, such as spin fluctuations, etc., which are essentially temperature independent. Based on this picture, the complex dielectric function can be described in terms of a Drude-Lorentz function:

$$\tilde{\epsilon}(\omega) = \epsilon_\infty - \frac{\omega_{pD}^2}{\omega^2 + i\omega\Gamma_D} + \sum_{MIR} \frac{\omega_{pj}^2}{(\omega_j^2 - \omega^2) - i\omega\Gamma_j}\ , \tag{6.3}$$

where ω_{pD}, Γ_D, and ϵ_∞ are the plasma frequency, the scattering rate of the free carriers, and the background dielectric constant for the Drude contribution; and ω_j with strength ω_{pj} and line width Γ_j is the jth Lorentzian oscillator at the mid-infrared band, respectively.

By using Eq. 6.3, we obtain fit curves for conductivity spectra at 100 K in the normal state with $\omega_{pD} = 10070 \pm 100\ cm^{-1}$ and $\Gamma_D = 110 \pm 5\ cm^{-1}$ for the undoped crystal; $\omega_{pD} = 10100 \pm 100\ cm^{-1}$ and $\Gamma_D = 145 \pm 5\ cm^{-1}$, and $\omega_{pD} = 10200 \pm 100\ cm^{-1}$ and $\Gamma_D = 170 \pm 5\ cm^{-1}$ for the Ni-doped crystals with $x = 0.0075$ and 0.014, respectively. Fit curves calculated from Eq. 6.3 are shown in Fig. 6.2 for conductivity spectra at 100 K, where the frequency-dependent conductivity $\sigma_1(\omega)$ is derived from Eq. 6.3:

$$\sigma_1(\omega) = \frac{\omega\epsilon_2(\omega)}{4\pi} \tag{6.4}$$

$$= \frac{1}{4\pi}\frac{\omega_{pD}^2\Gamma_D}{\omega^2 + \Gamma_D^2} + \sum_{MIR} \frac{\omega^2\omega_{pj}^2\Gamma_j}{(\omega_j^2 - \omega^2)^2 + \omega^2\Gamma_j^2}\ , \tag{6.5}$$

and the Lorentzian parameters ω_{pj}, ω_j, and Γ_j used in the fits are (in cm^{-1}): 15000, 500, 1800 (1900, 2000) for $j = 1$; and 14000, 3300, 7500 for $j = 2$, in the pure (x=0.0075, 1.5%) systems. The increase of of Γ_D with Ni doping here represents a considerable increase in the normal state scattering rate. Since the plasma frequencies, which have $\omega_{pD}^2 = 4\pi ne^2/m^*$ (n is the carrier concentration, and m^* is the effective mass), are nearly identical in both pure and doped materials, then as-

suming that m^* is not changing, Ni-doping at this level does not change the carrier concentration. As $\omega \rightarrow 0$ in Eq. 6.5, the value for the dc conductivity is $\sigma_{dc} = \omega_{pD}^2/4\pi\Gamma_D$. Using the Drude parameters from the fits at 100 K, the predicted values are $\sigma_{dc} = 15360\Omega^{-1}cm^{-1}$ in the pure crystal, and $\sigma_{dc} = 11730\Omega^{-1}cm^{-1}$, $\sigma_{dc} = 10160\Omega^{-1}cm^{-1}$ in the Ni-doped crystals with $x = 0.0075$, and $x = 1.5\%$, respectively. These results are in rough agreement with preliminary transport measurements on these systems [116].

In the superconducting state, the oscillator strength of the low-frequency conductivity condenses to a delta function at the origin (the electromagnetic response of the superconducting condensate) and the remaining conductivity can be interpreted in terms: (i) the appearance of a Drude-like contribution, or, the residual conductivity (as defined in the previous section); and (ii) a mid-infrared component which does not participate in the formation of the superconducting condensate and shows little temperature dependence.

Below T_c, the phenomenological two-component model can not generate a satisfactory fit for the ab-plane conductivity in the superconducting state [17]. The low-frequency residual conductivity is found to be $\sigma_1(\omega) \propto \omega^{-1}$ instead of ω^{-2} as would be expected from a Drude form [17] [90].

The low-frequency optical properties will be dominated by the zero-frequency δ function [17]

$$\epsilon_1(\omega) = \epsilon'_\infty - \frac{\omega_{ps}^2}{\omega^2}, \tag{6.6}$$

where ϵ'_∞ is the high-frequency contribution to ϵ_1, which contains the bound-electron contribution including the zero-frequency sum of all the bound excitations in Eq. 6.3, and ω_{ps} is the plasma frequency of the superconducting charge carriers and is related

to the concentration n_s of the superconducting carriers and their effective mass m^* by $\omega_{ps}^2 = 4\pi n_s e^2/m^*$. Fig. 6.3 shows the real part of the dielectric function as a function of $1/\omega^2$ from our experimental data of three samples at 10K plotted.

From ω_{ps}^2, which is the slope of $\epsilon_1(\omega)$ vs $1/\omega^2$, in Fig. 6.3, we obtain $\omega_{ps} = 9920 \pm 100\ cm^{-1}$ for the pure system. By comparing the normal state Drude plasma frequency $\omega_{pD} = 10070 \pm 100\ cm^{-1}$, the value of ω_{ps} indicates that nearly all of the Drude component has collapsed into the δ function, in agreement with the premise that this is a clean-limit system. On the other hand, in the Ni-doped system, $\omega_{ps} = 8070 \pm 100\ cm^{-1}$, which is much lower than the Drude component $\omega_{pD} = 10120 \pm 100\ cm^{-1}$ in the normal state. Since the strength of the $\delta \propto \omega_{ps}^2$, the Ni-doped ω_{ps} indicates that only about two thirds of the Drude component has collapsed into the δ function.

The slope of $\epsilon_1(\omega)$ vs $1/\omega^2$ is also a direct determination of the penetration depth λ in the superconducting state by $\lambda = 1/2\pi\omega_{ps}$ (ω_{ps} is in cm^{-1}) [17], yielding values of $\lambda = 1604 \pm 100$ Å, 1709 ± 100 Å, 1971 ± 100 Å for x=0, 0.0075, and 0.014 of Ni in $YBa_2(Cu_{1-x}Ni_x)_3O_{6.95}$. The increase in the penetration depth with Ni-doping is accompanied by an increase in the low-frequency residual conductivity, and a decrease in the strength of the condensate. Since Ni doping provides additional scattering, the system becomes dirtier and more of the pairs are scattered into electron-hole pairs, then the superconducting condensate becomes weaker. Therefore the penetration depth λ increases with doping. The frequency-dependent penetration depth $\lambda(\omega) = c/[4\pi\omega\sigma(\omega)]^{1/2}$ [17], directly calculated from our experimental data with a Kramers-Kronig analysis, are plotted in Fig. 6.4.

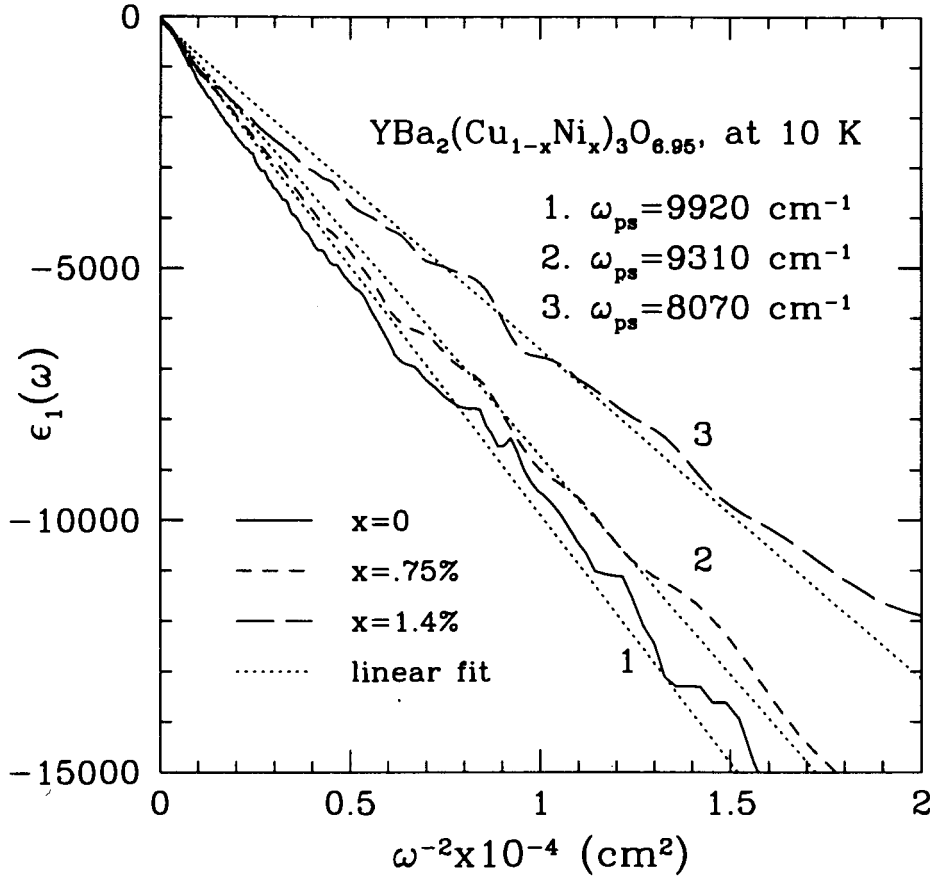

Figure 6.3: The real part of the dielectric function $\epsilon_1(\omega)$ as a function of $1/\omega^2$ for $YBa_2(Cu_{1-x}Ni_x)_3O_{6.95}$ for $x = 0$ (solid line), $x = 0.0075$ (dashed line), and $x = 0.014$ (long dashed line). The dotted line is the fit to a straight line whose slope gives value of ω_{ps}^2. The range of the data used for the fit is $\approx 70 - 500cm^{-1}$ at 10 K.

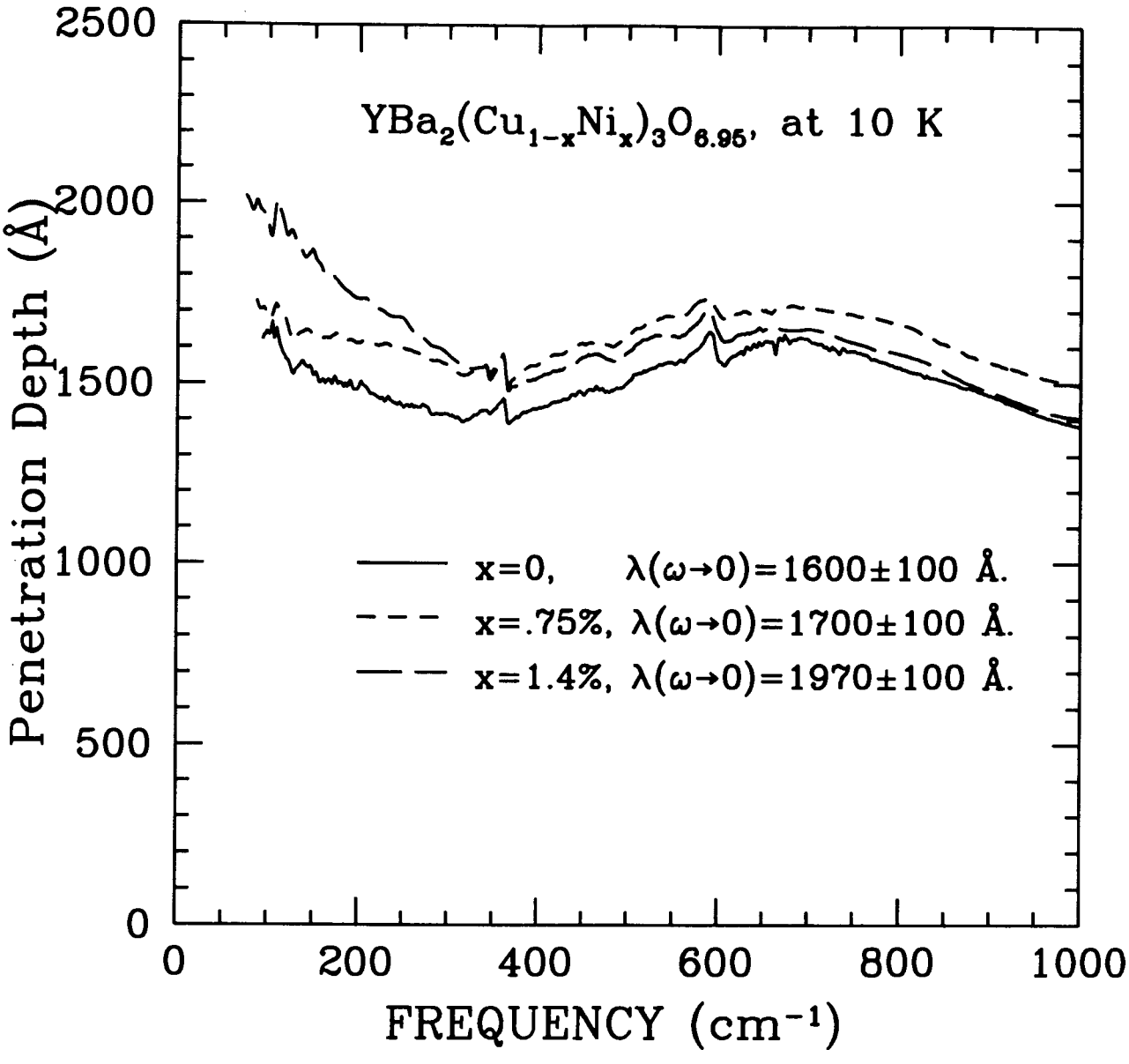

Figure 6.4: Frequency dependent penetration depth $\lambda(\omega) = c/[4\pi\omega\sigma(\omega)]^{1/2}$, below 1000 cm^{-1}.

6.5 Superconducting Energy Gap

The most interesting issue in the infrared properties of high-T_c superconductors is the origin and nature of the superconducting state. There is a growing body of evidence that the density of states in high-T_c superconductors is not zero for energies much lower than $k_B T_c$, in contrast to the situation in conventional superconductors [108] [117]. In conventional superconductors, a simple s-wave BCS model has a isotropic gap of width $2\Delta_0$ around the Fermi surface with $2\Delta_0/k_B T_c \approx 3.5$ at T=0 K for weak coupling or higher for stronger coupling. This energy gap is evident in the far-infrared and microwave range for low-T_c BCS superconductors [82].

For the high-T_c superconducting materials, infrared studies [67] [89] [90] reveal a feature at $\sim (8-12)k_B T_c$ in the reflectance, originally thought to be a BCS-like gap. However, there is increasing evidence to the contrary [134]. In high-T_c superconductors, the gap might not show up in the infrared spectrum for several reasons. First, the scattering rate of the charge carriers may be small relative to the superconducting energy gap $\Gamma \ll 2\Delta_0$ (Γ is in cm^{-1}); in other words, pure high-T_c materials can be in the clean-limit which presents the normal skin effect regime of superconductivity with $\Gamma \ll 2\Delta_0$; $\xi_0 \ll l \ll \lambda_L$ as discussed by Kamaras *et al.* [90]. Fig. 6.5 demonstrates the changes expected in the conductivity when a material becomes superconducting. Fig. 6.5.a is the clean-limit case and Fig. 6.5.b is the dirty-limit case. We assume that both the clean and dirty-limit superconductors have a superconducting gap with same value $2\Delta_0$. For a clean superconductor, its scattering rate $\Gamma \ll 2\Delta_0$, and the gap feature at $2\Delta_0$ is very weak below T_c since most of its spectral weight is transferred to the delta function at zero frequency as the Drude component condenses. Therefore, it is difficult to detect the superconducting

transitions across a gap by infrared spectroscopy [90]. On the other hand, for a dirty-limit superconductor, the scattering rate Γ is comparable to $2\Delta_0$ and a strong gap feature appears at $2\Delta_0$. In this case, one may expect to observe gap structure in the FIR conductivity. Secondly, high-T_c superconductivity might involve a d-wave or extended s-wave model in which the gap can be zero at some points (nodes) on the Fermi surface and conductivity $\sigma_1(w)$ in the superconducting state will start at $\omega = 0$ as in the normal state. With the existence of nodes, a finite can not appear in the infrared conductivity spectrum.

According to Anderson's theorem [97], magnetic impurities are expected to have a strong influence on superconductivity in the case of s-wave pairing, whereas a superconductor with an unconventional pairing state (p or d wave) is negligibly affected by magnetic impurities. Thus, our study on the magnetic impurity Ni can be an experimental test of the possible model of the superconductivity in high-T_c materials by: (i) enhancing the impurity scattering rate to move the pure $YBa_2Cu_3O_{6.95}$ into the dirty-limit for a possible observation of a spectroscopic BCS-like gap; (ii) substituting Ni impurities in the CuO_2 planes to distinguish between unconventional extended s-wave or d-wave and anisotropic conventional s-wave models [108], [110].

However, in spite of the enhanced scattering rate from substituting Ni impurities in $YBa_2Cu_3O_{6.95}$, the conductivity of our three crystals in the superconducting state shows no evidence of a conventional superconducting gap. Instead, the frequency dependence of the conductivity shows the development of a low-frequency residual conductivity, indicating that the $YBa_2Cu_3O_{6.95}$ superconductor is gapless [108]. From our earlier discussion, in the Ni-doped system, the plasma frequency in the superconducting state $\omega_{ps} = 8070 \pm 100\ cm^{-1}$, which is much lower than the Drude component $\omega_{pD} = 10120 \pm 100\ cm^{-1}$ in the normal state. Thus, the Ni-doping

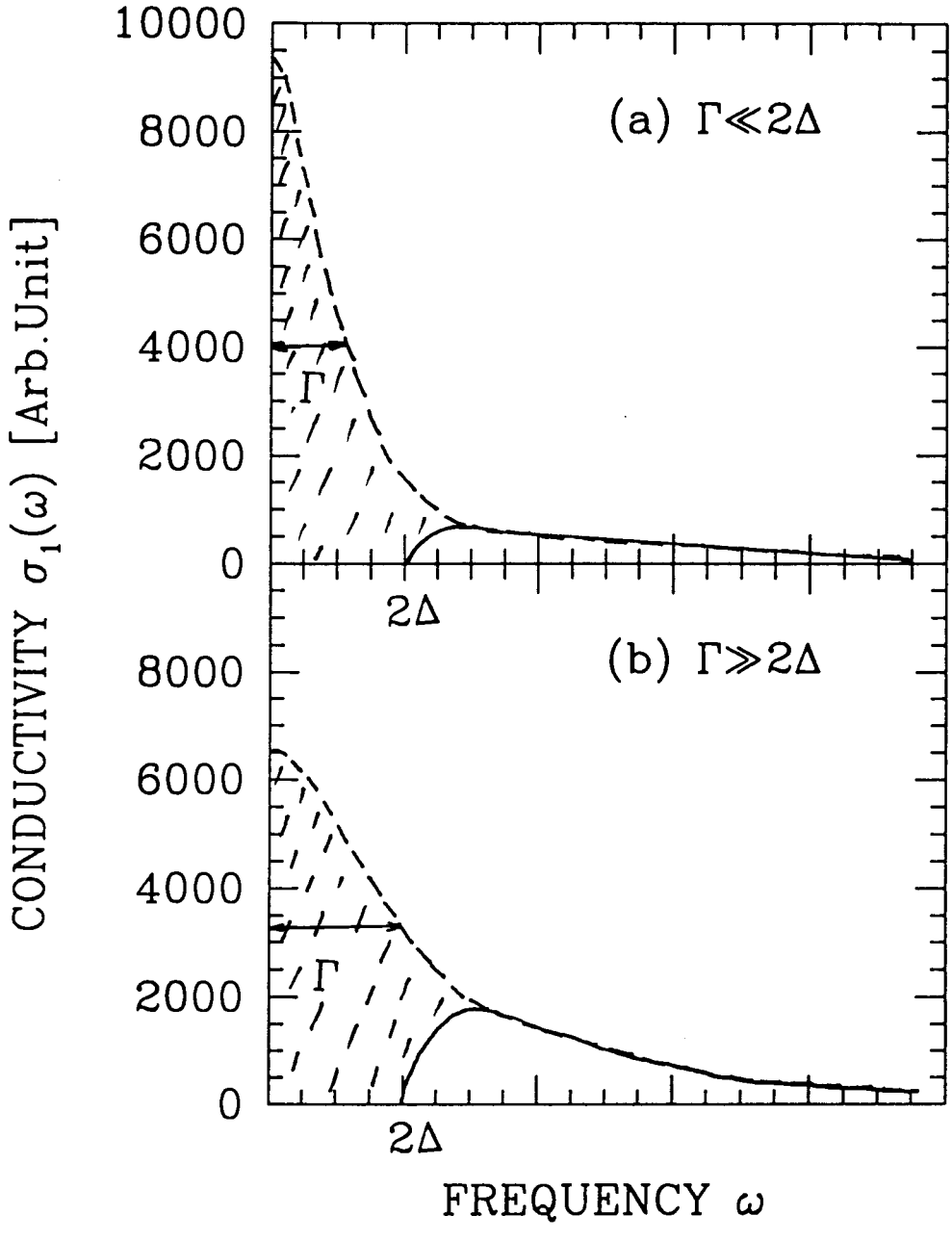

Figure 6.5: The conductivity (for $\omega > 0$) of a classical BCS superconductor in the (a) clean and (b) dirty limits. The dashed line represents conductivity in the normal state and the solid line represents conductivity in the superconducting state. The shaded area is the weight that collapses into the condensate

level of 1.5% should be enough to expose a gap feature if one exists. If we associate the increase of the scattering rate with impurities, we obtain $\Gamma_D = 110 \pm 5\ cm^{-1}$ in the undoped crystal, while in the heavily Ni-doped crystal $\Gamma_D = 170 \pm 5\ cm^{-1}$, which represents a considerable increase in the normal state scattering rate. The increase of Γ_D with Ni doping indicates that we are indeed moving away from the "clean-limit". Therefore it appears that the failure to observe a spectroscopic gap is not because of the lack of momentum conserving processes due to the clean limit [90], but due to the unconventional nature of the response of $YBa_2Cu_3O_{6.95}$.

There are a number of theories of superconductivity that include gaplessness in the density of states with or without disorder, including d-wave theories [107] [108], which have the attractive feature that disorder is naturally accommodated. Hence we concentrate our analysis on a comparison with conventional BCS s-wave models and d-wave theories. Briefly, in a classic s-wave case, the order parameter $\Delta(k)$ is constant with value Δ_0, $\Delta(k) = \Delta_0$. This gives rise to a square-root singularity in N(E) at energy $E = \Delta_0$. The order parameter of d-wave, approximately, is $\Delta(k) = \Delta_0(cosk_x a - cosk_y a)$, while the order parameter of extended s-wave is $\Delta(k) = \Delta_0(cosk_x a + cosk_y a)$, where Δ_0 measures the maximum gap amplitude about the Fermi surface. The common features of these two models are that they have lines of nodes in the gap function and peaks in $N(E)$ at energy $E = \Delta_0$ [115], as illustrated by Fig. 6.6.

Ni impurities are believed to be elastic scatterers in the YBCO system since Ni-doping does not affect the linear temperature dependence of penetration depth [100]. On the other hand, addition of as little as 0.15% Zn impurities, which are believed to be resonant scatterers [110], alters the linear behaviour of the penetration depth at low temperature, as indicated by D.A. Bonn et al. [99]. The effect of elastic scattering is

dramatically different for s-wave and d-wave superconductors. In a clean anisotropic s-wave superconductor, elastic scattering always reduces order-parameter anisotropy. This leads to a smearing of the energy gap anisotropy and eventually to an isotropic gap, and a decrease in the density of states (DOS) $N(E)$ at low frequency, so that the density of states $N(E)$ becomes more BCS-like with a clearly defined gap [97]. By contrast, in a d-wave or extended s-wave superconductor, the density of states $N(E)$ is gapless and increases linearly from $N(\epsilon_F) = 0$ at Fermi surface (where $E = \epsilon_F$). Once impurities are introduced in a d-wave superconductor, some of the quasiparticle pairs will be scattered out of the superconducting condensate into electron-hole pairs. Then the superconducting density of states will be considerably smeared by the impurity-induced disorder; and the conductivity spectra should show a Drude-like absorption extending all the way to zero frequency generated by impurities. In the d-wave case, on the other hand, impurities have different effects on the conductivity spectra that the defects wll induce a gap structure at $2\Delta_0$, as shown by J. P. Carbotte *et al.* [108].

The absence of any BCS-like gap features in the superconducting conductivity $\sigma_1(\omega)$ at low frequencies in our crystals is in agreement with what is known theoretically about the conductivity of d-wave superconductors. In addition, our experimental results show that the low-frequency residual conductivity is increasing with Ni-doping. As we discussed above, if impurities introduce a finite gap in an anisotropic s-wave superconductor, then the residual conductivity should be expected to decrease, which is exactly opposite to our experimental results. This implies that our experiments are consistent with models of superconductors [108] whose gap have line nodes on the Fermi surface, either a d-wave or extended s-wave superconductor, rather than an s-wave superconductor with an anisotropic gap which has non zero minimum.

At the present time we cannot distinguish between a d-wave and an extended

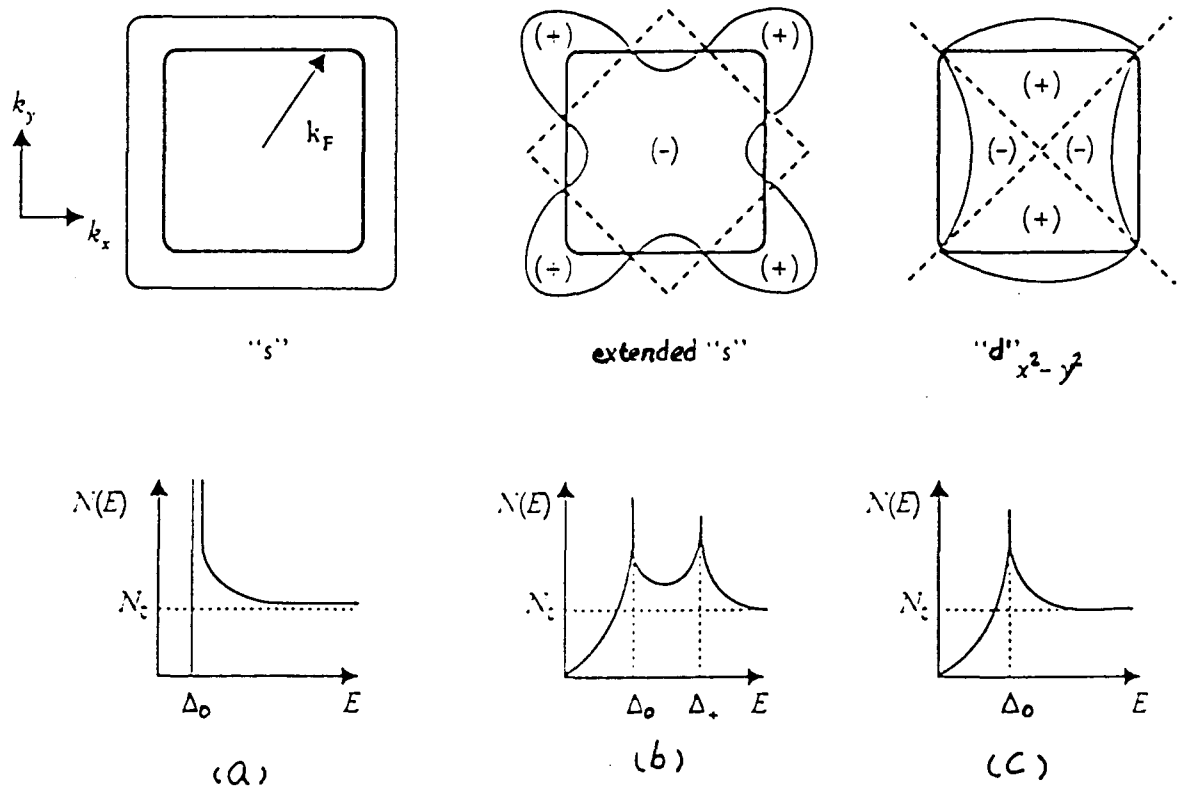

Figure 6.6: Fermi surface gap function and densities of states of a superconductor with tetragonal symmetry for various pairing symmetries. The gap functions in the $k_z = 0$ plane (top) are represented by the thin solid lines; distance from the Fermi surface (thick lines) gives the amplitude of the gap, a positive value being outside the Fermi surface, a negative value inside. The corresponding density of states for one-quasiparticle excitations N(E) is shown below each gap function, with N_0 the normal-state value. Gap node surfaces are represented by the dashed lines. (a) The classic s-wave case, where the gap function is constant, with value Δ_0. (b) The extended -s-wave case; (c) A d-wave case. The extended s-wave and d-wave functions shown here each have a linear density of states up to order Δ_0, which measures the maximum gap amplitude about Fermi surface.

s-wave gap by using the infrared technique. However, the existence of residual conductivity in the undoped material is consistent with a d-wave superconductor [110].

The absence of a fully-developed gap in our experimental results is in accordance with the results of photoemission spectroscopy which show an anisotropic gap with maximum along the Cu-O bond direction and vanishing magnitude of gap 45 ° away [112]. The recent precise measurements by Hardy *et al.* [100] provide evidence that shows a spectrum of excitations down to very low energies in the superconducting state and a linear behavior of penetration depth $\Delta\lambda(T) = \lambda(T) - \lambda(1.3T)$ at low temperature in the pure and Ni-doped $YBa_2Cu_3O_{6.95}$ system. This linear behaviour is quite unlike the exponentially activated behaviour caused by the nodeless energy gap of a conventionl s-wave BCS superconductor. This result is consistent with an anisotropic energy gap that has nodes at the Fermi surface, as discussed by Annett and Goldenfeld *et al.* [110] [111]. The anisotropy of the NMR relaxation rate [113] and the nonvanishing low-frequency Raman scattering [114] point in a similar direction.

Different tunneling experiments have come to opposite conclusions about the symmetry of the superconducting order parameter in the high-Tc cuprates. For example, D. A. Wollman *et al.* measured the properties of Josephson weak link junctions (YBCO-Pb) and found evidence for $d_{x^2-y^2}$ symmetry [163]. On the other hand, A. G. Sun *et al* studied Josephson tunneling and found their results inconsistent with this symmetry [164].

Our data is another piece of a growing amount of evidence that the low-temperature density of states in the high-T_c materials is profoundly different from conventional superconductors.

6.6 Conclusion

In summary, the infrared conductivities of pure and Ni-doped $YBa_2(Cu_{1-x}Ni_x)_3O_{6.95}$ single crystals indicates that no conventional s-wave superconducting gap is observed. Instead, our study shows evidence of either an extended s-wave or a d-wave superconductor. This result is consistent with a recent reflectance study on ion irradiated single crystals of $YBa_2Cu_3O_{6.95}$ [110]. In the normal state, Ni acts as scatterer, decreasing the value of σ_{dc} and broadening the Drude-like conductivity. However, at the highest Ni concentration, T_c is still $89K$, and the penetration depth is still linear at low temperatures [116]. These results indicat that, within our doping level, Ni impurity is not a pair-breaking scatterer which destroys the superconductivity in the $YBa_2Cu_3O_{6.95}$ system. Below T_c, our experimental results show a low-frequency residual conductivity and this component increases with Ni doping. These observations are not consistent with a simple s-wave superconductor, but support either an extended s-wave or a d-wave model that has nodes in the gap function. At the present time we cannot distinguish between a d-wave and an extended s-wave gap by infrared technique. This conclusion of gaplessness is supported by NMR and microwave measurements.

Chapter 7

Summary and Outlook

In conclusion, for our pure and Ni-doped $YBa_2Cu_3O_{6.95}$ twinned single crystals, we have focused on the search and determination for the nature of the superconducting gap by studying the effect of impurities on the optical conductivity. Our results indicate that the gap is not a simple anisotropic s-wave, but is instead either an extended s-wave or a d-wave gap. In the normal state, Ni acts as scatterer, decreasing the value of σ_{dc} and broadening the Drude-like conductivity. However, within our doping level, the penetration depth is still linear at low temperatures, indicating that Ni impurity is not a pair-breaking scatterer in the $YBa_2Cu_3O_{6.95}$ system. Below T_c, our experimental results show a low-frequency residual conductivity and this component increases with Ni doping. This result is consistent with a recent reflectance study on ion irradiated single crystals of $YBa_2Cu_3O_{6.95}$ [110]. These observations support either an extended s-wave or a d-wave model that has nodes in the gap function. At the present time we cannot distinguish between a d-wave and an extended s-wave gap by infrared technique.

For our polycrystalline samples, we have focused on the lattice vibrations and phonon assignment for the normal state properties and the temperature-dependent

spectrum of excitations for superconducting states. From our infrared reflectance studies on the superconducting polycrystalline materials Zn-doped $YBa_2Cu_3O_{7-\delta}$, Pb-doped $Bi_2Sr_2CuO_{6+y}$, and n-type Ce(Th)-doped $Nd_{1.85}Ce(Th)_{0.15}CuO_{4-y}$, we have revealed many details about the electronic properties of the high T_c copper oxides. Most of the phonon features appeared in the spectra have been tentatively assigned by comparing the experimental work on similar compounds from other groups. Our results are in reasonable agreement with theoretical calculations.

We have also applied a direct calculation of the wave vector and frequency dependent lattice vibrational tensor of $Bi_2Sr_2CuO_{6+y}$ based on the shell model. We have performed the fitting process on the shell model parameters in order to investigate the doping effects on phonon frequencies and lattice vibration. We find that not only the mass of ions in a lattice but also its total ionic charge as well as the core-shell spring constant can cause a great deal of variation of the phonon frequencies.

For the Zn-doped system, there is no obvious evidence showing a superconducting energy gap from our experimental results in the $YBa_2(Cu_{1-x}Zn_x)_3O_{7-\delta}$ system. The effects of inserting Zn^{2+} ions in the $YBa_2Cu_3O_{7-\delta}$ lattice lead to a strong depression of reflectivity in low frequency range and an increase of DC conductivity in the normal state. This suggests either that a free carrier model is totally inappropriate to describe these materials or that very strongly frequency-dependent damping processes are present.

By taking the ratio, $R_s(T)/R_n(T)$, of the reflectance in the superconducting state to that in the normal state, we have found that the low-frequency enhancement at $\sim 50cm^{-1}$ in the ratio for both Ce-doped and Th-doped $Nd_{1.85}Ce(Th)_{0.15}CuO_{4-y}$ samples should be assigned as the superconducting energy gap corresponding to

$2\Delta_0/k_bT_c$ of 3.1 ± 0.2 (Ce) and 3.9 ± 0.2 (Th) respectively. These values are within the range found for conventional strong coupling superconductors. We find that the optical properties of the n-type superconductors, including evidence of a gap, are very similar to those of the hole-type La-Sr-Cu-O system, and thus the mechanism for superconductivity is likely the same as well.

In spite of our studies as well as others, including various physical properties investigated by several experimental techniques, a number of uncertainties regarding the nature of the superconductivity in high-T_c cuprate still remain. So far neither the experimental investigations nor the many theoretical attempts have clearly revealed the microscopic pairing mechanism that could lead to the high transition temperatures. Specifically, the pairing mechanisms, the magnitudes and anisotropies of the superconducting energy gaps are still far from clear.

As better facilities and samples with better homogeneity become available, more informative and reliable data can be expected to further clarify these issues. Polarized optical measurements on high quality untwinned single crystal YBCO is one of the improvements which might provide more precise information about the strong anisotropy of the materials. It should be interesting to carry out polarized infrared experiments on single crystal n-type materials, as we mentioned earlier, to distinguish the positions of superconducting gaps in the ab-plane and c-axis. Finally, for more information about temperature-dependent superconducting excitation spectra in all the high-T_c superconductors, it is useful to compare the behavior of anisotropic optical response in these lower $T_c(20 \sim 40K)$ materials with those of higher T_c (over $77K$) superconductors. For theoretical models on lattice-dynamical calculations, in particularly the shell model, more extensive neutron-scattering experiments, in addition with optical spectra, are needed to measure the phonon dispersion curves in

the existing high temperature superconducting materials to provide sufficient data to determine the interatomic forces in solids.

Hopefully, the further research will lead to a better understanding of the mechanism of superconductivity in the high temperature superconducting materials.

Appendix

Physical Picture Underlying the Shell Model

In this appendix, we will briefly review the theory of lattice dynamics as described by the shell model. The theory of lattice dynamics actually precedes the development of the quantum mechanics [154]. However, early development of lattice dynamics was centered on the so-called ionic point charge model, where each atom inside the solid is treated as a point charge. The electronic degree of freedom has been completely neglected. This has led to severe unphysical consequences in the predicted phonon-dispersion relations and related optical properties. For example, in alkali halide crystals where the point charge model was supposed to apply, the calculated splitting between the longitudinal and transverse optical modes at the zone center is more that twice as large as the actual experimental data [155]. The high-frequency dielectric function ϵ_∞ will always be 1 in the point charge model because the electronic screening effects are neglected, while in reality, ϵ_∞ can be much larger. For the NiO crystal, $\epsilon_\infty = 12.99$.

The shell model offers a simple yet very effective way to incorporate the electronic degree of freedom into the lattice dynamics theory—hence improving the point charge model qualitatively. The essence of the shell model is depicted in Fig. A.1, where an electron shell of charge Y is attracted to the ion core whose charge is X through a spring k. The atomic polarization due to the electronic excitations is naturally built in by a simple displacement between the center of the shell and the ion core. The

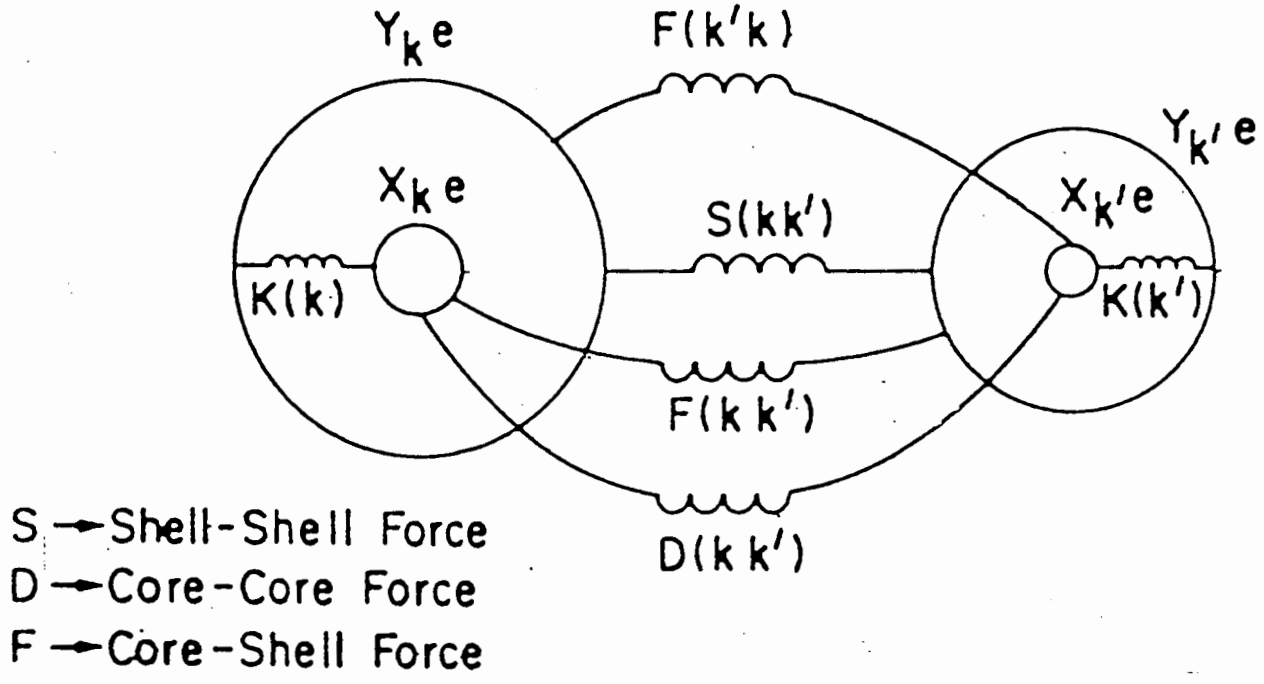

Figure A.1: Generalized shell model. $X_k e$ and $X_{k'} e$ denote the core charges while $Y_k e$ and $Y_{k'} e$ denote the shell charges. The springs represent the various short-range forces. The forces $F(kk')$ and $F(k'k)$ are frequently taken to be equal, as in this work.

atomic polarizability α can be related to the spring constant the the shell charge by,

$$\alpha = Y^2/k. \tag{A.1}$$

Using the shell model, nearly perfect agreement with experiments can be obtained for the phonon dispersion relations of alkali halides [155]. For NiO, the shell model gives a value of $\epsilon_\infty = 12.22$, in good agreement with the experimental result [156]. Throughout the past three decades, the shell model has remained the major method for studying the lattice dynamics of various systems [156] - [160] because (1) it is simple to use and the physical picture is very clear, and (2) it is capable of producing high quality results in practical applications. Since the discovery of high-T_c superconductors, the shell model has been applied to nearly every copper-oxide discovered so far [73] - [161]. The optical measurements such as the Raman spectra and the infrared spectra carried out here have played an essential role in determining the parameters used in the shell model calculations for the high-T_c compounds. In general, the shell model has demonstrated to be able to produce rather accurate phonon dispersion relations for these copper oxides. Perhaps the most impressive demonstration is the work on the Nd_2CuO_4 crystal as reported by Pintschovius et al.[161], where the shell model not only gave good optical results but also accurate phonon dispersion throughout the Brillouin zone.

The derivation of the shell model equations is straightforward. Only the most salient step will be outlined below. More detailed description can be found in Ref. [157]. One starts with the harmonic expansion of the crystal total energy E against the ionic vibration u^c and the shell vibration u^s,

$$E = \Phi + \frac{1}{2}\sum_{l,\alpha} k_\alpha [u^c_\alpha(l) - u^s_\alpha(l)]^2, \tag{A.2}$$

where α denotes the x,y,z Cartesian components, l denotes the atomic location in the crystal. The last term of the above equation is the standard core-shell energy due the the attached spring k_α.

$$\Phi = \frac{1}{2}\sum_{l,\alpha}\sum_{l',\alpha'}\Phi^{cc}_{\alpha,\alpha'}u^c_\alpha(l)u^c_{\alpha'}(l)$$

$$+\frac{1}{2}\sum_{l,\alpha}\sum_{l',\alpha'}\Phi^{cs}_{\alpha,\alpha'}u^c_\alpha(l)u^s_{\alpha'}(l)$$

$$+\frac{1}{2}\sum_{l,\alpha}\sum_{l',\alpha'}\Phi^{ss}_{\alpha,\alpha'}u^s_\alpha(l)u^s_{\alpha'}(l). \qquad \text{(A.3)}$$

This is the second order expansion of the core-core Φ^{cc}, core-shell Φ^{cs} and shell-shell Φ^{ss} interactions. Most of these interactions are Coulomb interactions except for the shell-shell term where additional short range interactions are included to account for the overlap repulsion due to the electronic exchange effect. This overlap interaction is often simulated by the Born-Mayer potential, ae^{-br} with a and b as adjustable parameters and r the interatomic distance. Therefore, the required parameters in a shell model are, the core-shell spring constant k, the core and shell charges X and Y, and the Born-Mayer constants a and b. For systems with more than one kind of atom per unit cell, the number of parameters can be large. Typically, about 15 to 20 parameters are used for the high-T_c compounds.

The equation of motion in terms of u^c and u^s can be obtained by Newton's second law. And the two basic shell-model matrix equations which determine the phonon dispersion relation directly follow the equation of motion,

$$\omega^2(\mathbf{q})\mathbf{m}\mathbf{U}^c = [\mathbf{R} + e^2\mathbf{ZCZ}]\mathbf{U}^c + [\mathbf{R} + e^2\mathbf{ZCY}]\mathbf{W} - e\mathbf{ZE}_{ext}, \qquad \text{(A.4)}$$

$$0 = [\mathbf{R}^\dagger + e^2\mathbf{YCZ}]\mathbf{U}^c + [\zeta + e^2\mathbf{YCY}]\mathbf{W} - e\mathbf{YE}_{ext} \qquad \text{(A.5)}$$

Here, we have used a set of notations closely following those used in Ref. [157]. **M**, **Z**, and **Y** are the diagonal matrices of core masses, core charges, and shell charges. **R** represents the short range shell-shell repulsion. **C** is the Coulomb interaction matrix. ζ is a matrix function of **R**, **C**, and the core-shell spring constant, which is defined in Ref. [157]. $\mathbf{U}^c$ and **W** are the core displacement and the shell to core relative displacement vectors. The left hand size of Eq. (A.5) is zero because the shell is treated as massless as the electronic mass is much smaller than the ionic mass. It is also possible to directly calculate the dielectric response functions from the shell model. The equation for the dielectric functions has been recently derived in Ref. [155] by Chen and Callaway. An application of their theory for the optical properties of Nd_2CuO_4 is reported in Ref. [162].

Bibliography

[1] H. Kamerlingh Onnes, Leiden Comm. **120b** (1911)

[2] H. Kamerlingh Onnes, Leiden Comm. **122b** (1911)

[3] H. Kamerlingh Onnes, Leiden Comm. **124c** (1911)

[4] H. Kamerlingh Onnes, Leiden Comm. Suppl. **34** (1913)

[5] F. London and H.London, Proc. Roy. Soc. **A149** 71 (1935)

[6] F. London and H.London, Physica **2** 341 (1935)

[7] J.Bardeen, L. N. Cooper, and J. R. Schrieffer, Phys. Rev. **108**, 1175(1957)

[8] V. Daniel Hunt, *Superconductivity Sourcebook*, (John Wiley and Sons, 1989).

[9] J. G. Bednorz and K. A. Müller, Z. Phys. **B64**, 189 (1986).

[10] C. E. Gough, M. S. Coklough, E. M. Forgan, R. G. Joudan, M. Keene, C. M. Murihead, A. I. M. Rae, N. Thomas, J. S. Abell and S. Sutton, Nature **326**, 855 (1987).

[11] J. Niemeyer, M. R. Dietrich, C. Polotis, Z. Phys. **B67**, 155 (1987).

[12] M. K. Wu, J. R. Ashburn, C. J. Torng, P. H. Hor, R. L. Meng, L. Gao, Z. J. Hwang, Y. Q. Wang, C. W. Chu, Phys. Rev. B **58**, 908 (1987).

[13] H. Maeda, Y. Tanaka, M. Fukutomi, and T. Asano, Jpn. J. Appl. Phys. **27**, L209 (1988); C. W. Chu, J. Bechtold, L. Gao, P. H. Hor, Z. J. Huang, R. L. Meng, Y. Y. Sun, Y. Q. Wang, and Y. Y. Xue, Phys. Rev. B **60**, 941 (1988).

[14] Z. Z. Sheng, A. M. Hermann, A. El Ali, C. Almasan, J. Estrada, T. Datta, and R. J. Matson, Phys. Rev. B **60**, 937 (1988).

[15] Y. Tokura, H. Takagi, and S. Uchida, Nature **337**, 345 (1989).

[16] S. Martin, A. T. Fiory, R. M. Fleming, L. F. Schneemeyer, and J. V. Waszczak, Phys. Rev. B **60**, 2194 (1988).

[17] D. B. Tanner and T. Timusk, *Physical Properties of High Temperature Superconductors III*, (World Scientific, 1992), p363.

[18] R. T. Collins, Z. Schlesinger, F. Holtzberg, and C. Field, Phys. Rev. B **63**, 422 (1989).

[19] G. Briceno, and A. Zettle, Solid State Commun, **70**, 1055 (1989).

[20] Z. X. Shen et al., Phys. Rev. Lett. **70**, 1553 (1993).

[21] G. M. Eliashberg, Zh. Eksp. Teor. Fiz. **38**, 966 (1966) [Sov. Phys. -JETP **11**, 696 (1960)]; P. B. Allen and B. Mitrovic, in "Solid State Physics", H. Ehrenreich, F. Seitz, and D. Turnbull, eds., (Academic Press, New York, 1982), p. 2-92.

[22] P. W. Anderson, Science **235**, 1196 (1987).

[23] S. Chakravarty, A. Sudbo, P. W. Anderson, and S. Strong, Science **261**, 337 (1993).

[24] C. Jiang, and R. C. Dynes, Phys. Rev. B **47**, 5325 (1993).

[25] P. Monthoux, A. V. Balatsky, and D. Pines, Phys. Rev. Lett. **67**, 3448(1991).

[26] C. M. Varma et al., Phys. Rev. Lett. **63**, 1995 (1989); *ibid.* **64**, 497 (1990).

[27] J. R. Schrieffer et al., Phys. Rev. Lett. **60**, 944 (1988).

[28] W. M. Que and G. Kirczenow, Phys. Rev. B **38**, 4601 (1988).

[29] Charles Kittel, *Introduction to Solid State Physics*, Fifth Ed. (Wiley, New York, 1976).

[30] Gerald Burns, *Solid State Physics*, (Academic Press, 1985)

[31] F. Wooten, *Optical Properties of Solid*, (Academic Press, New York and London, 1972)

[32] D. C. Mattis, and J.Bardeen, *Phys. Rev.*, **111**, 412 (1958)

[33] G. Xiao, F. H. Streitz, A. Gavrin, Y-W. Du, and C. L. Chien, Phys. Rev. B **36**, 8782 (1987);

[34] Frank Bridges, Guoguang Li, James B. Boyce, T. Claeson, Phys. Rev. B **48**, 1266 (1993).

[35] S. A. Hoffman, M. A. Castro, G. C. Follis, and S. M. Durbin Phys. Rev. B **49**, 12170 (1994).

[36] M. Affronte, D. Pavuna, O. Martin, F. Licci, T. Besagni, and S.Cattani, Solid State Commun., **70**, 951 (1989).

[37] D.G. Hinks, L. Soderholm, D. W. Capone, II, B. Dabrowski, A. W. Mitchell, and D. Shi, Appl. Phys. Lett. **53** (1988) 423-425.

[38] D.B. Wiles and R.A. Young, J. Appl. Cryst. **14**, 149 (1981).

[39] Y. Ikeda, H. Ito, S. Shimomura, Y. Oue, K.Inaba, Z. Hiroi, and M. Takano, Physica C**159**, 93 (1989).

[40] Yasuhiko Takemura, Masashi Hongo, and Shumpei Yamazaki, Jpn. J. Appl. Phys. **28** (1989) L916.

[41] Justin K. Akujieze, Ph.D. Thesis, Illinois Institute of Technology, unpublished (1991).

[42] J. L. Peng, R. N. Shelton, and H. B. Radousky, Solid State Commun. **71**, 479 (1989).

[43] Suso Gygax, private communication; George Soerensen, Ph.D. Thesis, Simon Fraser University, unpublished (1993).

[44] J. P. Franck, A. Hnatiw, M. K. Yu, S. Gygax, G. Soerensen, E. Altendorf and J. C. Irwin, Proc. on *Lattice Effect in High T_C Superconductors*, Santa Fe (1991).

[45] Qian Song, B.P. Clayman, and Suso Gygax, Physica **C165** (1990) 328-334.

[46] L. Pintschovvius, W. Reichardt, in *Physical Properties of High Temperature Superconductors IV*, edited by D. M. Ginsberg (World Scientific, 1993) pp. 375-451.

[47] C. Thomsen and M. Cardona, in *Physical Properties of High Temperature Superconductors IV*, edited by D. M. Ginsberg (World Scientific, 1989) pp. 257-258.

[48] L F Mattheiss, Phys. Rev. Lett. **58**, 1024 (1987); B. V. Chakraverty, D. D. Sarma and C. N. R. Rao, Physica C **156** (1988) 413; J. M. Wheatley, T. C. Hsu and P. W. Anderson, Phys. Rev. B **37** (1988) 5897.

[49] D. B. Tanner and T. Timusk, *Physical Properties of High Temperature Superconductors III*, edited by D. M. Ginsberg (World Scientific, 1989), p 339.

[50] D. M. Ginsberg, in *Physical Properties of High Temperature Superconductors I*, edited by D. M. Ginsberg (World Scientific, 1989) p.4.

[51] A. P. Litvinchuk, C. Thomsen and M. Cardona, in *Physical Properties of High Temperature Superconductors IV*, edited by D. M. Ginsberg (World Scientific, 1993) pp. 375-451.

[52] N. Pyka, W. Reichardt, L. Pintschovvius, S. L. Chaplot, P. Schweiss, A. Erb, and G. Muller-Vogt, Phys. Rev. **B48**, 7746 (1993).

[53] Tsuyoshi Kajitani, Kejji Kusaba, Masae Kikuchi, Yasuhiko Syono, and Makoto Hirabayashi, Jpn. J. Appl. Phys. **27** (1988) L354.

[54] R. Dupree, A. Gencten, and D. McK. Paul, Physica C **193** 81 (1992).

[55] Y. C. Jean et al., Phys. Rev. Lett. **64**, 1593 (1990).

[56] H. Alloul, P. Mendels, H. Casalta, J. F. marucco, and J. Arabski, Phys. Rev. Lett. **67**, 3140 (1991).

[57] H. Alloul, et al.,Physica C **171** (1990) 419; P. Mendels, et al., *ibid.* **171**, (1990) 429.

[58] G. A. Thomas, H. K. Ng, A. J. Millis, R. N. Bhatt, R. J. Cava, E, A. Rietman, D. W. Johnson, Jr., G. P. Espinnosa, and J. M. Vandenberg, Phys. Rev. B **36**, 846 (1987); Genzel, A. Wittlin, J. Kuhl, Hj. Mattausch, W. Bauhofer, and A. Simon, Solid State Commun. **63**, 843 (1987).

[59] D. A. Bonn, A. H. O'Reilly, J. E. Greedan, C. V. Stager, T. Timusk, K. Kamarás, and D.B. Tanner, Phys. Rev. B**37**, 1574 (1988).

[60] R. T. Collins, Z. Schlesinger, R. H. Koch, R. B. Laibowitz, T. S. Plaskett, P. Freitas, W. J. Gallagher, R. L. Sandstrom, and T. R. Dinder, Phys. Rev. Lett. **59**, 704 (1987).

[61] L. Genzel, A. Wittlin, M. Bauer, M. Cardona, E. Schonherr, and A. Simon, Phys. Rev. B **40**, 2170 (1989).

[62] W. Ose, P. E. Obermayer, H. H. Otto, T. Zetter, H. Lengfellner, J. Keller, and K. F. Renk, Z. Phys. B **70**, 307 (1989).

[63] V. Zelezny, D.B. Tanner, K. Kamarás, L. P. Kozeeva, and A. A Pavlyuk, Z. Phys. B **96**, 313-318 (1995).

[64] C. C. Homes and T. Timusk, Phys. Rev. Lett. **71**, 1645 (1993).

[65] Z. Schlesinger, R. T. Collins, L. D. Kaiser, and F. Holtzberg, Phys. Rev. Lett. **59**, 1958 (1987).

[66] Z. Schlesinger, R. T. Collins, L. D. Kaiser, F. Holtzberg, G. V. Chandrashekar, M. W. Shafer, and T. M. Plaskett, Physica C **153** 1734 (1988).

[67] Z. Schlesinger, R. T. Collins, F. Holtzberg, C. Feild, G. Koren,and A. Gupta, Phys. Rev. B **41**, 11237 (1990).

[68] M. K. Crawford, W. E. Farneth, R. K. Bordia, and E. M. McCarron III, Phys. Rev. B**38**, 11 382 (1988). E. L. Benitez, J. J. Lin, and S. J. Poon, W. E. Farneth, M. K. Crawford, and E. M. McCarron, Phys. Rev. B**38**, 5025 (1988).

[69] C. C. Homes, M. Reedyk, D. A. Crandles, and T. Timusk, Appl. Opt. **32** 2976(1993).

[70] N. Pyka, W. Reichardt, L. Pintschovvius, S. L. Chaplot, P. Schweiss, A. Erb, and G. Muller-Vogt, Phys. Rev. B**48**, 7746 (1993).

[71] J. Humlicek, A. P. Litvinchuk, W. Kress, B. Lederle, C. Thomsen, M. Cardona, H. U. Habermeier, I. E. Trofimov, and W. Konig, Physica C **206**, 345 (1993)

[72] M. Cardona, L. Genzel, R. Liu, A. Wittlin, Hj. Mattausch, F. García-Alvarado, and J. M. García-Gonzalez, Solid State Commun. **64**, 727 (1987).

[73] J. Prade, A. D. Kulkarni, F. W. de Wette, W. Kress, M. Cardona, R. Reiger, and U. Schröder, Solid State Commun. **64**, 1267 (1987).

[74] R. Liu, C. Thomsen, W. Kress, M. Cardona, B. Gegenheimer, F. W. de Wette, J. Prade, A. D. Kulkarni, and U. Schröder, Phys. Rev. **B37**, 7971 (1988); W. Kress, U. Schröder, J. Prade, A. D. Kulkarni, and F. W. de Wette, Phys. Rev. B**38**, 2906 (1988).

[75] Frances E. Bates, Phys. Rev. B**39**, 322 (1989).

[76] H. J. Ye, R. P. McCall, W. E. Farneth, E. M. McCarron III and A. J. Epstein, Phys. Rev. B**43**, 10 574 (1991).

[77] M. Stravola, D. M. Krol, W. Weber, S. A. Sunshine, A. Jayaraman, G. A. Kourouklis, R. J. Cava, and E. A. Rietman, Phys. Rev. B**36**, 850 (1987).

[78] P. B. Kirby, M. R. Harrison, W. G. Freeman, I. Samuel, and M. J. Haines, Phys. Rev. B**36**, 8315 (1987).

[79] P. Chaudhari, R. T. Collins, P. Freitas, R. J. Gambino, J. R. Kirtley, R. H. Koch, R. B. Laibowitz, F. K. LeGoues, T. R. McGuire, T. Penney, Z. Schlesinger, A. P. Segm¨ller, S. Foner and E. J. McNiff,Jr., Phys. Rev. B**36**, 8903 (1987).

[80] A. Wittlin, L. Genzel, M. Cardona, M. Bauer, W. König, E. Garcia, M. Barahona and M. V. Cabañas. Phys. Rev. B**37**, 652 (1988).

[81] Z. Schlesinger *et al.*, Phys. Rev. Lett. **59**, 1958 (1987); G. A. Thomas *et al.*, Phys. Rev. Lett. **61**, 1313 (1988); T. Timusk *et al.*, Physica (Amsterdam) **153-155C**, 1744 (1988).

[82] R. E. Glover III and M. Tinkham, Phys. Rev. **108**, 243 (1957).

[83] P. L. Richards and M. Tinkham, Phys. Rev. **119**, 575 (1960).

[84] D. M. Ginsberg and M. Tinkham, Phys. Rev. **118**, 990 (1960).

[85] R. R. Joyce, and P. L. Richards, Phys. Rev. Lett. **24**, 1007 (1970).

[86] G. Brandli and A. J. Sievers, Phys. Rev. B**5**, 3550 (1972).

[87] See, for example, J. Schutzmann *et al.*, Phys. Rev. B**46**, 512 (1992). Z. Schlesinger *et al.*, Phys. Rev. Lett. **65**, 801 (1990).

[88] M. Reedyk, and T. Timusk, Phys. Rev. Lett. **69**, 2705 (1992).

[89] L. Forro et al., Phys. Rev. Lett. 65 (1990) 1941.

[90] K. Kamarás et al., Phys. Rev. Lett. 64 (1990) 84.

[91] D. Romero et al., Phys. Rev. B44 (1991) 2818.

[92] R.A. Hughes et al., Phys. Rev. B40 (1990) 5162.

[93] A good review of optical data is given by G.A. Thomas, in High Temperature Superconductivity, ed. by D.P. Tunstal, W. Barford, and P. Osborne (Adam Hilger, Bristol, 1991), p. 169; also D.B. Tanner et al., in High Temperature Superconductivity, ed. by J. Ashkenazi et al., (Plenum, New York, 1991), p.159.

[94] M.J. Sumner, J.-T. Kim, and T.R. Lemberger, Phys. Rev. B47 (1993) 12248.

[95] P. Schleger, W. N. Hardy, and B. X. Yang, Physica C**176**, (1991) 261.

[96] C. C. Homes, Q. Song, B. P. Clayman, D. A. Bonn, R. Liang, and W. N. Hardy, submitted to Phys. Rev. Lett.

[97] P. W. Anderson, J. Phys. Chem. Solids **11**, 26 (1959).

[98] D. W. Lynch and W. R. Hunter, "Comments on the optical constants o fmetals and an introduction to the data for several metals," in *Handbook of Optical Constants of Solids*, E. D. Palik, ed, (Academic, New York, 1985), pp. 286-295.

[99] D. A. Bonn, S. Kamal, Kuan Zhang, R. Liang, D. J. Barr, E. Klein, and W. N. Hardy, Phys. Rev. B**50**, 4051 (1994).

[100] D. A. Bonn, R. Liang, et al., Phys. Rev. B**47**, 11 314 (1993).

[101] Ruixing Liang, P. Dosanjh, D. A. Bonn, D. J. Baar, J. F. Carolan and W. N. Hardy, Physica C**195**, (1992) 51.

[102] H. Romberg, N. Ncker, J. Fink, Th. Wolf, X. Xi, G. Koch, H. P. Geserich, M. Durrler, W. Assmue, and B. Gegenheimer, Z. fur Phys. B 78, 367 (1990)

[103] D. N. Basov, A. V. Puchkov, R. A. Hughes, T. Strach, J. Preston, T. Timusk, D. A. Bonn, R. Liang, and W. N. Hardy, Phys. Rev. B**49**, 12 165 (1994).

[104] D. M. Miller, P. L. Richards, S. Estmad, A. Inam, T. Venkatesan, B. Dutta, X. D. Wu, C. B. Eom, T. H. Geballe, N. Newman, And B. B. Cole, Phys. Rev. B**47**, 8076 (1993).

[105] P. A. Lee, Phys. Rev. B**47**, 11 314 (1993).

[106] K. Ishida, Y. Kitaoka, N. Ogata, T. Kamino, K. Asayama, J. R. Cooper, and N. Athanassopoulou, Physica B**186-188**, (1993) 1015.

[107] R. E. Walstedt et al.,Phys. Rev. B**48**, 10 646 (1993).

[108] C. Jiang, and J. P. Carbotte, Phys. Rev. B**50**, 9449 (1994); J. P. Carbotte, C. Jiang, D. N. Basov, and T. Timusk, Phys. Rev. B**51**, 11798 (1995).

[109] P. J. Hirschfeld et al., Phys. Rev. B**40**, 6695 (1989).

[110] L. S. Borkowski and P. J. Hirschfield, Phys. Rev. B**49**, 15404 (1994), P. J. Hirschfeld et al., Phys. Rev. B**48**, 4219(1993).

[111] J. A. Annett, N. Goldenfeld and S. R. Renn, Phys. Rev. B**39**, 2778 (1991).

[112] Z. X. Shen et al., Phys. Rev. Lett. **70** (1993) 1553. D. S. Dessau et al., Phys. Rev. Lett. 66 (1991) 2160.

[113] N. Bulut and D.J. Scalapino, Phys. Rev. Lett. **68** (1992) 706.

[114] X. K. Chen, J. C. Irwin, to be published (1995) .

[115] Daniel. L. Cox, and M. Brian Maple, Phys. Today, **2**(1995) 32.

[116] D. A. Bonn, private communication.

[117] D. Mandrus, Michael C. Martin, C. Kendziora, D. Koller, L. Forro, and L. Mihaly, Phys. Rev. Lett. **70** (1993) 2629.

[118] J. D. Jorgensen, P. Lightfoot, and S. Pei, Supercond. Sci. Technol. **4**, S11 (1991).

[119] S.H. Wang, Q. Song, B.P. Clayman, J.L. Peng, L. Zhang and R.N. Shelton, Phys. Rev. Lett. **64** (1990) 1067-1070.

[120] L. H. Greene and B. G. Bagley, in *Physical Properties of High Temperature Superconductors II*, edited by D. M. Ginsberg (World Scientific, 1990) p.167.

[121] K. Remschnig, J. M. Tarascon. P. F. Miceli, G. W. Hull, and W. R. McKinnon, Phys. Rev. B **43**, 5481 (1991).

[122] Robert M Hazen, in *Physical Properties of High Temperature Superconductors II*, edited by D. M. Ginsberg (World Scientific, 1990) p.167.

[123] J. M. Tarascon. et al., Phys. Rev. B **39**, 11 587 (1989). J. M. Tarascon, Y. LePage, W. R. McKinnon, R. Ramesh, M. Eibschutz, E. Tselepis, E. Wang, and G. W. Hull, Physica C**167** (1990) 20-34.

[124] C.C. Torardi, M.A. Subramanian, J.C. Calabrese, J. Gopalakrishnan, E.M. McCarron, K.J. Morrissey, T.R. Askew, R.B. Flippen, U. Chowdhry, A.W. Sleight, Phys. Rev. B **38**, 225 (1988).

[125] G. Burns, G. V. Chandrashekhar, F. H. Dacol, M. W. Shafer, and P. Strobel, Solid State Commun. **67**, 603 (1988).

[126] A. D. Kulkarni, F. W. de Wette, J. Prade, U. Schroder, and W. Kress, Phys. Rev. B **41**, 6409 (1990).

[127] J. Prade, A. D. Kulkarni, F. W. de Wette, W. Kress, and U. Schroder, Phys. Rev. **B39**, 2771 (1989).

[128] F. W. de Wette, private communication.

[129] T. Timusk, S. L. Herr, K. Kamarás, C. D. Porter, D. B. Tanner, D. A. Bonn, J. D. Garrett, C. V. Stager, J. E. Greedan, and M. Reedyk, Phys. Rev. B**38**, 6683 (1988).

345 (1989).

[130] Wu Jiang, S. N. Mao, X. Xi, Xiuguang Jiang, J. L. Peng, T. Venkatesan, and C. J. Greene, Phys. Rev. Lett. **73**, 1291 (1994)

[131] Wu Jiang, J. L. Peng, Z. Y. Li, C. J. Greene, Phys. Rev. B**47**, 8151 (1993).

[132] Z. Z. Wang et al., Phys. Rev. B**43**, 3020 (1991).

[133] D. H. Wu et al., Phys. Rev. Lett. **70** 85 (1993).

[134] H. Tagaki, S. Uchida, and Y. Tokura, Phys. Rev. Lett. **62**, 1197 (1989).

[135] J. T. Markert and M. B. Maple, Solid State Commun. **70**, 145 (1989).

[136] L. Degiogi, S. Rusiecki, and P. Wachter, Physica **161C**, 239 (1989).

[137] N. P. Ong, in *Physical Properties of High Temperature Superconductors II*, edited by D. M. Ginsberg (World Scientific, 1990) p.480.

[138] S. Sugai, T. Kobayashi, and J. Akimitsu, Phys. Rev. B**40**, 2686 (1989).

[139] Z. Schlesinger, R. T. Collins, M. W. Schafer, and E. M. Engler, Phys. Rev. **B36**, 5275 (1987); G. L. Doll, J. T. Nicholls, M. S. Dresselhaus, A. M. Rao, J.

M. Zhang, G. W. Lehman, P. C. Eklund, G. Dresselhaus, and A. J. Strauss, Phys. Rev. B**38**, 8850 (1988).

[140] G. L. Doll, J. Steinbeck, G. Dresselhaus, M. S. Dresselhaus, A. J. Strauss, and H. J. Zeiger, Phys. Rev. B**36**, 8884 (1987).

[141] T. Ekino and J. Akimitsu, Phys. Rev. B**40**, 7364 (1989); I. Takeuchi, J. S. Tsai, T. Manako, and Y. Kubo, Phys. Rev. B**40**, 9286 (1989).

[142] M. S. Sherwin, P. L. Richards, and A. Zettl, Phys. Rev. B**37**, 1587 (1987).

[143] Q. Huang, J. F. Zasadzinski, N. Tralshawala, K. E. Grag, D. G. Hinks, J. L. Peng, and R. L. Greene, Nature **347**, 369 (1990).

[144] K. Hirochi, S. Hayashi, H. Adachi, T. Mitsutu, T. Hirao, K. Setsune, and K. Wasa, Physica **160C**, 273 (1989).

[145] M. K. Crawford, G. Burns, G. V. Chandrashekbar, F. H. Dacol, W. E. Farneth, E. M. McCarron III, and R. J. Smalley, Phys. Rev. B**41**, 8933 (1990).

[146] M. K. Crawford, G. Burns, G. V. Chandrashekbar, F. H. Dacol, W. E. Farneth, E. M. McCarron III, and R. J. Smalley, Solid State Commun. **73**, 507 (1990).

[147] F. E. Bates and J. Eldridge, Solid State Commun. **72**, 187 (1989).

[148] B.P. Clayman, S.H. Wang, and Q. Song, Physica **B165&166** (1990) 1233-1234.

[149] J. -M. Bassat, P. Odier, and F. Gervais, Phys. Rev. B**35**, 7126 (1987).

[150] Hk. Müller-Buschbaum and W. Wollschläger, Z. AnorgAllg. Chem. **414**, 76 (1975).

[151] V. G. Hadjiev, I. Z. Kostadinov, L. Bozukov, E. Dinolova, and D. M. Mateev, Solid State Commun. **71**, 1093 (1989).

[152] Private communication, the tunneling data of ceramic $Nd_{1.85}Ce(Th)_{0.15}CuO_{4-y}$ was provided by Dr. J. L. Peng.

[153] H. Chen and J. Callaway, Phys. Rev. B**46** 14321, (1992).

[154] For references to early works, see, M. Born and K. Huang, *Dynamical Theory of Crystal Lattices* (Oxford, London, 1954).

[155] H. Chen and J. Callaway, Phys. Rev. B**45** 2085, (1992).

[156] A. D. B. Woods, W. Cochran, and B. N. Brockhouse, Phys. Rev. **119**, 980 (1960).

[157] G. Venkataraman, L. A. Feldkamp, and V. L. Sahni, *Dynamics of Perfect Crystals* (MIT Pressm, Cambridge, Mass, 1975).

[158] W. Reichardt, V. Wagner, and W. Kress, J. Phys. C **8**, 3955 (1975).

[159] A. D. Kulkarni, F. W. de Wette, J. Prade, U. Schroder and W. Kress, Phys. Rev. B **43** 5451 (1991).

[160] M. Mostoller, J. Zhang, A. M. Rao, P. C. Eklund, Phys. Rev. B **41**, 6488 (1991).

[161] L. Pintschovius, N. Pyka, W. Reichardt, A. Yu. Ramiantsev N. L. Mitrofanov, A. S. Ivanov, G. Collin, and P. Bourges, Physica C **185-189**, 156 (1991).

[162] H. Chen and J. Callaway, Physica C **210**, 308 (1993). J. T. Markert and M. B. Maple, Solid State Commun. **70**, 145 (1989).

[163] D. A. Wollman et al., Phys. Rev. Lett. **71** (1993) 2134.

[164] A. G. Sun, D. A. Gajewski, M. B. Maple, and R. C. Dynes, **Phys. Rev. Lett.** **72** (1994) 2267.